NASA TECHNICAL MEMORANDUM NASA TM-88527

THEORETICAL AND EXPERIMENTAL INVESTIGATIONS OF IGNITION, COMBUSTION, AND EXPANSION PROCESSES OF HYPERGOLIC LIQUID FUEL COMBINATIONS AT GAS TEMPERATURES UP TO 3000°K

Harry Schulz

Translation of: "Theoretische und experimentelle Untersuchungen von Zündungs-, Verbrennungs-, und Expansionsvorgangen hypergoler flussiger Treibstoffkombinationen bei gastemperaturen bis 3000°K," dissertation submitted from the Faculty of Mechanical Engineering of the Rhein-Westfalia Technical College, 1967, pp. 1-123

NATIONAL AERONAUTICS AND SPACE ADMINISTRATION
WASHINGTON, D.C. 20546 MARCH 1987

STANDARD TITLE PAGE

1. Report No. NASA TM-88527	2. Government Accession No.	3. Recipient's Catalog No.
4. Title and Subtitle THEORETICAL AND EXPERIMENTAL INVESTIGATIONS OF IGNITION, COMBUSTION, AND EXPANSION PROCESSES OF HYPERGOLIC LIQUID FUEL COMBINATIONS AT GAS TEMPERATURES UP TO 3000°K		5. Report Date March 1987 6. Performing Organization Code
7. Author(s) Harry Schulz		8. Performing Organization Report No. 10. Work Unit No.
9. Performing Organization Name and Address SCITRAN Box 5456 Santa Barbara, CA 93108		11. Contract or Grant No. NASw- 4004 13. Type of Report and Period Covered Translation
12. Sponsoring Agency Name and Address National Aeronautics and Space Administration Washington, D.C. 20546		14. Sponsoring Agency Code

15. Supplementary Notes
Translation of: "Theoretische und experimentelle Untersuchungen von Zundungs-, Verbrennungs-, und Expansionsvorgangen hypergoler flussiger Treibstoffkombinationen bei gastemperaturen bis 3000°K," dissertation submitted from the Faculty of Mechanical Engineering of the Rhein-Westfalia Technical College, 1967, pp. 1-123

16. Abstract
The ignition, combustion, and expansion characteristics of hypergolic liquid propellant mixtures in small rocket engines are studied theoretically and experimentally. It is shown by using the Bray approximation procedure that the reaction H + OH + M = H_2O + M (where M is the molecular mass of the gas mixture) has a strong effect on the combustion efficiency. Increases in recombination energies ranging from 30 to 65% were obtained when the rate of this reaction was increased by a factor of 10 in gas mixtures containing 90% oxygen. The effect of aluminum additions and various injection techniques on the combustion process is investigated.

17. Key Words (Selected by Author(s))	18. Distribution Statement
	Unclassified and Unlimited

19. Security Classif. (of this report)	20. Security Classif. (of this page)	21. No. of Pages	22. Price
Unclassified	Unclassified	163	

L-TM 88527

THEORETICAL AND EXPERIMENTAL INVESTIGATIONS OF IGNITION, COMBUSTION AND EXPANSION PROCESSES OF HYPERGOLIC LIQUID FUEL COMBINATIONS AT GAS TEMPERATURES UP TO 3000°K

Dissertation submitted from the Faculty of Mechanical Engineering of the Rhein-Westfalia Technical College, Aachen toward the academic degree of Doctor of Engineering

Submitted by graduate engineer

Harry Schulz

of Gelsenkirchen

Adviser: Prof. Dr.-Ing. F. A. F. Schmidt
Co-adviser: Prof. Dr.-Ing. H. Kühl

Date of oral examination: 23 May 1967

FOREWORD

Design of high-power engines requires not only practical experience but the most accurate possible knowledge of the thermodynamic processes of ignition, combustion and expansion of chemical fuel combinations. With respect to the use of high-energy fuels with high combustion temperature, incorporation of the reaction-kinetic processes in expansion is of great interest.

In the Institute for Thermal Technology and Combustion Engines of the Technical College, Aachen, Dr.-Ing. F. A. F. Schmidt, Director, there has been special emphasis on research in ignition and combustion for many years [1, 2, 3, 4]. Recently the thermodynamics of high-temperature combustion has taken the foreground [5, 6].

It was Prof. Schmidt who provided the impetus for this work, and who made it possible, through valuable council and continuing scientific and technical support, for me to carry it out. At this point I wish to express my special thanks to him.

Prof. Dr.-Ing. H. Kühl also deserves my heartiest thanks for accepting the position of co-advisor and for his valuable suggestions and stimuli in the completion of the work.

The objective of this work is the application of thermodynamic calculations to determination of power characteristics with liquid fuel combinations, with inclusion of reaction kinetic laws in nozzle flow of hot combustion gases. The theoretical calculations are supplemented by experimental investigations.

For their willing help in the treatment of detail problems as well as in the structure and performance of the experiments, the author thanks Graduate Engineers H. P. Berg and W. P. Lee. The author thanks Dr.-Ing. H. Prehn for his help in the discussion of thermodynamic calculations.

I wish further to thank the Chief Engineer of the Institute, Dr.-Ing. May, for his continuing support.

Extensive computations were carried out in the computer center of the Technical College, Aachen and in the German Computer Center, Darmstadt; I wish to thank them here for their support.

Bayer AG very kindly assisted the performance of the experimental studies by providing unsymmetrical dimethylhydrazine at no cost.

I particularly thank the German Research Society for support of the work through providing support.

TABLE OF CONTENTS /1

A. INTRODUCTION /3

Theoretical calculations of power of high-temperature engines have so far been limited principally to treatment of hypothetical limiting cases of chemical and of frozen equilibrium during expansion. This treatment of nozzle flow, based on thermodynamic principles, generally provides sufficient accuracy for conventional fuels if one assumes frozen equilibrium, because certain reserves exist with respect to the actually attainable power under certain circumstances.

As the difference between the two types of expansion becomes greater with transition to higher temperatures, this can give rise to considerable uncertainties for proper design, because recombination effects cause a shift in the power level.

Therefore, the statement of the objective includes not only calculation of power for the theoretical limiting cases, but also treatment of the actual course of expansion.

For the selected fuel combination, we first work out an approximation method by means of which a more accurate view of the expansion course is possible. The treastment of the expansion flow considering the finite reaction velocities of all the reactions which proceed presupposes use of a very fast digital computer, as well as knowledge of the kinetic data. Using recent findings of the American space agency, NASA [7] and with the aid of the German Computer Center in Darmstadt, an extensive computer program will be used to supplement the approximate solution in order to determine the expansion flow with relaxation.

Out of the many technologically usable fuel combinations, some hypergolic fuel pairs were selected for the investigations in this work. The fuel mixture UDMH = $(CH_3)_2N_2H_2$ + HNO_3 will be used for the desired comparison between the theoretical calculations and the experimental results.

Nitric acid was chosen as the oxidizer because this oxygen carrier forms hypergolic combinations with many fuels, is chemically stable, and does not tend to explosions and spontaneous decomposition.

The reaction-kinetic calculations used with the selected /4
fuel combinations to determine expansion flow with relaxation, including the approximation solutions can in principle be transferred to other systems. The calculations make it possible to consider other high-energy fuel combinations.

Supplementing an existing program for equilibrium computation on the Siemens 2002 digital computer at the Aachen Technical College [3], the specific heats, the isentropic exponent and the velocity of sound at chemical equilibrium were derived, because these quantities are needed for calculation by the approximation procedure.

The agreement on comparison of the theoretical calculations and the experimental investigations is an important prerequisite for working out principles. As hardly any data have yet become available from use of liquid fuels in small engines, we first studied the effect of various design and operating quantities on the power behavior of the model

combustion chamber test stand which was developed. The goal of these experiments is determining important engine parameters.

Because of the use of highly concentrated nitric acid, special design features and increased safety precautions are required in design of the combustion chamber test stand.

To supplement the combustion chamber experiments, ignition delay times were to be measured under certain conditions using a special apparatus, because this value is important for starting conditions when using hypergolic fuels.

In solid fuel engines, there have been various determinations of reduction of instability phenomena by addition of light metals to the fuel [8]. In order to clear up the question of the extent to which these phenomena can also be observed with liquid fuels, experimental studies on this point were set up.

The final expansion temperature, because of the great difference between the theoretical limiting cases, is well suited for approximate experimental consideration of recombination effects [9].

By means of temperature measurements and comparison of them with the corresponding theoretical values, a further portion of the work provides a contribution to expansion of knowledge of the actual course of combustion and expansion in high-temperature engines. /5

B. THEORETICAL CONSIDERATION OF COMBUSTION AND EXPANSION PROCESSES WITH CONSIDERATION OF DISSOCIATION AND RECOMBINATION

1. Characteristic values in rocket engines

Conversion of the chemical energy bound into the fuels into the kinetic energy of the exhaust gas stream occurs in a continuous flow process. The individual processes such as evaporation of the injected fuel components, diffusion, heat transfer, combustion and expansion are complex, and some of them occur simultaneously. It is not possible to consider a single process as decisive for evaluating a fuel [10, 11, 12].

Along with theoretical considerations [13, 14, 15], experimental studies in particular [16, 17, 18] have contributed to expansion of knowledge about the process of combustion. It has appeared that determination and utilization of characteristic values is of great use for engine design.

a. Thrust coefficient, characteristic velocity and specific impulse

The thrust of a rocket is determined from the impulse relation [1, 10].

$$S = M_s W_2 + (p_2 - p_0) F_2 \quad *) \tag{1}$$

With

$$W_2 = \sqrt{\frac{2\varkappa}{\varkappa - 1} \frac{\mathfrak{R} \cdot T_1}{M_1} \left[1 - \left(\frac{p_2}{p_1}\right)^{\frac{\varkappa - 1}{\varkappa}}\right]} \tag{2}$$

and

$$M_s = p_1 F_{min} \sqrt{\varkappa \left(\frac{2}{\varkappa + 1}\right)^{\frac{\varkappa + 1}{\varkappa - 1}} \frac{M_1}{\mathfrak{R} \cdot T_1}} \tag{3}$$

(1) transforms into /7

$$S = P_1 F_{min} \varkappa \sqrt{\frac{2}{\varkappa-1}\left(\frac{2}{\varkappa+1}\right)^{\frac{\varkappa+1}{\varkappa-1}}\left[1-\left(\frac{P_2}{P_1}\right)^{\frac{\varkappa-1}{\varkappa}}\right]} + (P_2 - P_a)F_2 \qquad (4)$$

By definition of the thrust coefficient:

$$C_F = \varkappa \sqrt{\frac{2}{\varkappa-1}\left(\frac{2}{\varkappa+1}\right)^{\frac{\varkappa+1}{\varkappa-1}}\left[1-\left(\frac{P_2}{P_1}\right)^{\frac{\varkappa-1}{\varkappa}}\right]} + \frac{P_2 - P_a}{P_1}\cdot\frac{F_2}{F_{min}} \qquad (5)$$

one gets a simple relation for the thrust:

$$S = C_F F_{min} P_1 \qquad (6)$$

The characteristic velocity c is defined as:

$$c^* = \frac{P_1 F_{min}}{M_s} \qquad (7)$$

or with Equation (3)

$$c^* = \frac{\sqrt{\frac{\mathcal{R}\cdot T_1}{M_1}}}{\sqrt{\varkappa\left(\frac{2}{\varkappa+1}\right)^{\frac{\varkappa+1}{\varkappa-1}}}} \qquad (8)$$

If one relates the thrust according to Equation (6) to the unit of mass throughflow, one obtains the specific impulse, I_{sp}:

$$I_{sp} = \frac{S}{M_s} = \frac{C_F F_{min} P_1}{M_s} \quad 1) \qquad (9)$$

1. Using the mixed square system, the specific impulse gets the dimension kp.s/kg [1]. In practice, the usual dimension is s. (See also Equation (10).

Then, after introduction of the characteristic velocity, from (9) we obtain

$$I_{sp} = \frac{c_F \cdot c^*}{g} \qquad (10)$$

The specific impulse is the characteristic value for comparison of power values of different fuel systems [10]. It can also be obtained with the help of the effective exhaust velocity: $I_{sp} = w_{e\,eff}/g$. Relation (10) separates the processes within the combustion chamber and in the nozzle, which is important for investigation of the individual processes. According to Equation (10) the specific impulse depends, on one hand, on the thermodynamic properties of the fuel and the quality of combustion (characterized by c^*); while, on the other hand, the efficiency of the expansion (characterized by c_F) is considered in the nozzle. The combustion process is, then, separated from the expansion process, so that c^* in particular can be determined simply. This is of great interest for engine development. As for the theoretical calculation of these characteristic values according to (5) and (8), the problems are in the choice of the correct value for the isentropic exponent $\bar{\varkappa}$. As the expansion is linked with a steep temperature drop, different averages for $\bar{\varkappa}$ must be found to determine c^* and c_F. As the temperature drop is relatively slight up to the narrowest cross-section, c^* can be considered a function of combustion chamber conditions for the case of frozen flow. But if reactions occur in the convergent part of the nozzle, the conditions in the nozzle throat must be defined, because the characteristic velocity determines the value of the flow up to the narrowest cross section [19]. /8

Possibilities for calculation of the isentropic exponents are presented in section B. 2d.

b. Characteristic length and residence time of gases in the combustion chamber

Combustion in rocket combustion chambers occurs within a relatively small space. As the mass throughput, the combustion process, and the gas properties determine the combustion chamber volume and the narrowest cross section of the nozzle, the quotient of the chamber volume V_k and the throat cross section F_{min} was used very early as a useful parameter in engine development [10].

$$L^* = \frac{V_k}{F_{min}} \qquad (11)$$

The characteristic length L^* is a measure of the residence time of the combustion gas in the combustion chamber. As different fuel combinations need different residence times for preparation and complete burning, the required characteristic length can depend primarily on the fuel system used. /9

The characteristic length of the experimental combustion chambers is varied in the experimental investigations.

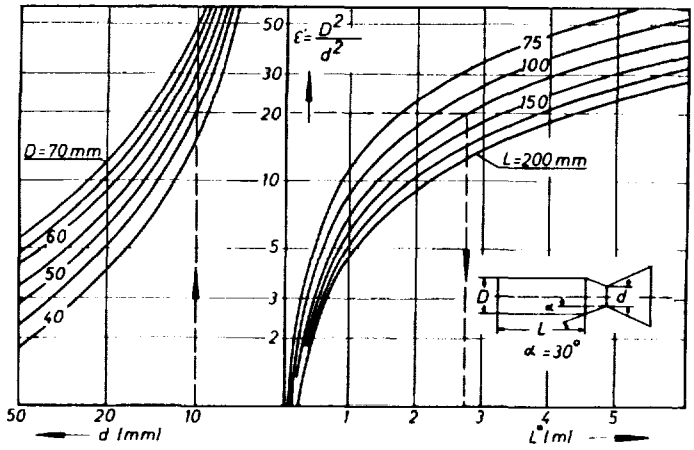

Figure 1. Nomogram for determining the characteristic length of the experimental test chamber.

Figure 1 shows various possible combinations of combustion chamber geometry to establish the characteristic length.

In the approximate determination of the gas residence time in the combustion chamber it is assumed that the combustion gas fills the entire chamber volume [18].

From the continuity relation and the gas equation, one obtains for the residence time of the gases:

$$t_v = \frac{V_k \cdot P_1}{M_s} \left(\frac{M}{R \cdot T}\right)_{\text{average}} \qquad (12)$$

With introduction of (8) and (11), (12) transforms into /10

$$t_v = L^* C \left(\frac{M}{R \cdot T}\right)_{\text{avg.}} \qquad (13)$$

On the other hand, according to (8)

$$c^* = \frac{\sqrt{\left(\frac{\mathcal{R}\cdot T}{M}\right)_b}}{\sqrt{\varkappa\left(\frac{2}{\varkappa+1}\right)^{\frac{\varkappa+1}{\varkappa-1}}}} \qquad (14)$$

index D = nozzle

With the assumption that $\left(\frac{\mathcal{R}\cdot T}{M}\right)_{avg} = k\left(\frac{\mathcal{R}\cdot T}{M}\right)_b$

with k = constant, (13) transforms [18] into

$$l_r = \frac{L^*}{c^* k\left[\varkappa\left(\frac{2}{\varkappa+1}\right)^{\frac{\varkappa+1}{\varkappa-1}}\right]} \qquad (15)$$

Barrere [10] gives an average for usual fuel combinations:

$$l_r = 2{,}38 \cdot \frac{L^*}{c^*} \qquad (16)$$

The residence time of the gas in the combustion chamber usually is between 2 and 7 msec.

c. Calculation of combustion chamber volume required to burn liquid fuel combinations

The combustion chamber volume is determined by the time needed for conversion of the injected fuel components into combustion gases. The two components introduced at the injection head end of the generally cylindrical combustion chamber are conducted into the thrust nozzle as combustion gases at high temperature. Along with the fuel properties, the nature of the injection and the preparation of the mixture are important. In general, it can be said that the efficiency of combustion, without considering heat transfer to the walls, is higher with larger reaction volume. Through heat losses on one hand and because of the added

weight on the other hand, however, the usable efficiency [11] is reduced in larger combustion chambers, so that an optimal combustion chamber volume exists for each design.

This volume is usually found experimentally, but there have been various reports on approximate numerical determination [10, 20, 21].

In the following, the combustion chamber volume is determined over the course of the reaction by means of simplified assumptions. The ratio of combustion chamber length to diameter lies within narrow limits, so that determination of the volume practically establishes the combustion chamber geometry.

For the combustion chamber volume per unit of mass throughput, the following relation can be established:

$$V_k^* = v(z) \cdot \overline{m_s'} \cdot l(z) \qquad (17)$$

in which

$V_k^* = \frac{V_k}{M_s}$ = specific combustion chamber volume

$z = \frac{x}{L}$ = relative combustion chamber length

with x = distance from the injection head and L = combustion chamber length.

v = specific volume of the combustion gases.

In order to determine the fuel conversion $\overline{m_s'}$ as a function of the distance from the injection head plane, the following simplifications are introduced for the reaction kinetic treatment, according to C. C. Miesse [22]: The fuels react only in the vapor phase; the fuel vapors react

as a simple chemical reaction; complete mixing exists; the system is isothermal. Under these assumptions, the conversion equation is:

$$d(m_s') = k_r (M_s')^e dt \qquad (18)$$

in which $d(m_s')$ = relative increase of converted fuel per unit time, dt.

k_r = reaction rate constant referred to the fuel mass converted per unit time

M_s' = relative proportion of unburned fuel

e = order of the reaction

For injection heads with good atomization within a short distance, the combustion gas can be considered a homogeneous mixture. Thus the portion of the yet unreacted fuel M_s' at any point x along the chamber is equal to the total mass less that portion already burned, m_s'.

$$M_s' = 1 - m_s' \qquad (19)$$

With this relation, (18) changes into:

$$d(m_s') = k_r (1 - m_s')^e dt \qquad (20)$$

The path-time law can be defined with the residence time t_v for the combustion chamber as: $l_v dx = L dt$

and by introducing $= dx/L$

$$dt = dz \cdot t_v \qquad (21)$$

With this, (20) becomes:

$$d(m_s') = k_r \cdot t_v \cdot (1 - m_s')^e dz \qquad (22)$$

For a first-order reaction and a reaction rate independent of z, the integration can be done easily.

$$z = \frac{1}{k_r l_v} \int \frac{d(m_s')}{(1 - m_s')} \qquad (23)$$

$$z = \frac{1}{k_r l_v} \ln\left(\frac{1}{1 - m_s'}\right) + C_o$$

With the boundary conditions: $z = 0$, $m_s' = 0$, $C_o = 0$, /13 one obtains:

$$e^{z \cdot k_r l_v} = \frac{1}{1 - m_s'}$$

or

$$m_s' = 1 - e^{-z k_r l_v} \qquad (24)$$

Equation (24) shows that the proportion of burned mass near the injection head increases rapidly with rising z.

For the development of the specific volume, the course $v = k_i l_v z$ is assumed as a first approximation (k_i = constant).

For instance, the specific volume can be calculated from the experimentally determined gas velocity (see p. 86) by means of the continuity equation.

Equation (17), on differentiation, yields:

$$dV_k^* = v \cdot m_s' \frac{dl}{dz} dz + m_s' \cdot l \frac{dv}{dz} dz + vl \frac{dm_s'}{dz} dz \qquad (25)$$

or, after introduction of the quantities calculated above:

$$= 2k_i \cdot l_v^2 z\,dz - 2k_i \cdot l_v^2 z \cdot e^{-k_i l_v z}\,dz + k_i k l_v^3 z^2 e^{-k_i l_v z}\,dz \qquad (26)$$

Integration of (26) gives the desired volume:

$$\int dV_k^* = k_i\, l_v^2 \left[2\int z\,dz - 2\int z\, e^{-k_i l_v z}\,dz + k l_v \int z^2 e^{-k_i l_v z}\,dz\right] \qquad (27)$$

The solution of (27) can be found through partial integration.

$$V_k^* = k_i \cdot l_v^2 z^2 \left[1 - e^{-k_i l_v z}\right] \qquad (28)$$

With introduction of $v = k_i\ t_v\ z$ and the gas equation, one /14 obtains:

$$V_k^* = l_v z \cdot R \cdot \left(\frac{T_i}{M_i}\right) \frac{1}{p_i} \left[1 - e^{-k_i l_v z}\right] \qquad (29)$$

According to (29), with use of Equation (16) simultaneously, the specific combustion chamber volume depends only on the thermodynamic gas properties, the reaction rate and the quantity z. For a homogeneous first-order reaction, Barrere [10] reports $k \sim \frac{1}{\tau_{ch}}$

Thus $k l_v = \frac{l_v}{\tau_{ch}} = D_i$ becomes the first Kammkohler number.

For the example calculation, D_i is selected as an average [22].

The variable z is assigned to be a measure of the quality of the combustion chamber. If, with completed engines, various development epochs are calculated for the quantity z with known combustion chamber volumes, one obtains a curve according to Figure 2.

$$z = \frac{V_K^* M_1 \cdot P_1}{4 \cdot R \cdot T_1 \left[1 - e^{-k \cdot t_v}\right]} \qquad (29a)$$

V^*_K = actual combustion chamber volume per unit of mass throughput

t_v = gas residence time in the combustion chamber

M_1, P_1, T_1 = state of the combustion gases at the end of combustion

z = combustion chamber characteristic value

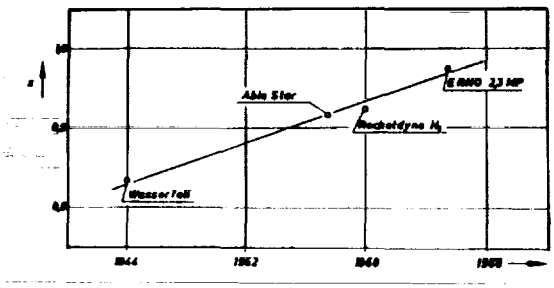

Figure 2. Development of the combustion chamber characteristic value z.

Figure 2 shows that current designs have already achieved very high maturity. /15

The data used for the calculation are shown in Table 1.

Table 1

Engine	Waterfall	Aerojet Gen. Able-Star	Rocketdyne H 1	ERNO 2.3 Mp
Pressure, P_t atm	20	14	45,6	9,2
Volume, V_k dm^3	51	18	150	14,5
Throughput, M_e, kg/s	44	12,85	333	7,83
Temperature T_t °K	2740	2610	3220	3010
Molecular weight M_t kg/mol	29,4	22,2	21,9	19,9

By use of Figure 2, the specific combustion chamber volume can be determined according to Equation (29) as a function of the fuel used and the desired chamber pressure. Figure 3 shows the result of such a design.

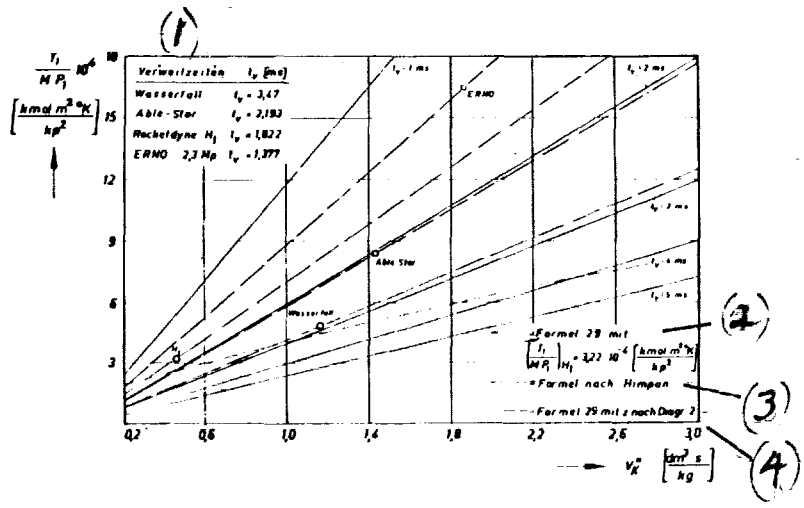

Figure 3. Specific combustion chamber volume of liquid fuel rockets.

1. Residence times
2. Formula (29) with
3. Formula according to Himpan
4. Formula (29) with z from Diagram 2.

The required volume can be determined relatively accurately in comparison with the relation given by Himpan [20]. In particular, one can easily determine the effect of operating conditions such as the chamber pressure and the mixing ratio on the required reaction volume. /16

2. Thermodynamic state quantities, characteristic numbers and engine powers with the equilibrium expansion.

a. Calculation of the gas state in the combustion chamber, the exhaust gas composition, and the theoretical power with chemical and frozen equilibrium

The power of a chemical fuel is determined essentially by its combustion temperature and the molar mass of the combustion gases. Using the fundamental program developed by O. Stumpt [3] for the Siemens 2002 digital computer, the

exhaust gas composition can be determined at chemical equilibrium for arbitrarily chosen pressures and temperatures, including their enthalpy and entropy. These data serve as the basis for establishing the enthalpy-entropy diagram as in Figure 5. Determination of the adiabatic combustion temperature at constant pressure is based on the condition of constant total enthalpy for the fuel mixture consisting of fuel and oxidizer, and the combustion products.

$$h_{fuel} = h_{exhaust\ gas} \quad [1] \qquad (30)$$

$$h_{fuel} = 1/M_{fuel} \sum(\nu_i \cdot H_i) \qquad (31)$$

ν_i indicates the number of moles of fuel component i per mole of fuel, while H_i represents the absolute molar enthalpy of fuel component i at the injection conditions. T_o = 298.16 °K.

The absolute enthalpy of oxidizer and fuel at the reference temperature T_o can be determined from existing tables of heats of formation, $\Delta H_{f(T_o)}$ [10]. The heat of formation corresponds to the absolute enthalpy change on formation of a material from its elements in the standard state. The absolute enthalpies of various elements are known from the literature [15].

From this we have: /17

$$H_{i(T_o)} = \Delta H_{f(T_o)} + \sum_k [\beta_k \cdot H_{k(T_o)}]_i \qquad (32)$$

In relation (32), k are the elements having the atomic or molar number ß forming the compound i of the fuel or oxidizer.

---

1. Enthalpy is generally designated as h in rocket technology.

For example, for the absolute enthalpy of furfuryl alcohol, $C_5H_6O_2$ at the reference temperature T_o:

$$H_{C_5H_6O_{2(T_o)}} = \Delta H_{f C_5H_6O_{2(T_o)}} + 5H_{C_{graphit(T_o)}} + 3H_{H_{2(T_o)}} + H_{O_{2(T)}} \quad (33)$$

The computer program is adapted on the following basis:

At absolute zero, the absolute enthalpies of the burned gaseous materials CO_2, H_2O, N_2 and O_2 are zero [23].

The still unknown absolute entropy of solid carbon in Equation (33), H_c graphite (T_o) is determined from the reaction equation

$$C_{graphite} + O_2 = CO_2$$

$$H_{CO_{2(T_o)}} = \Delta H_{f CO_{2(T_o)}} + H_{C_{graphit(T_o)}} + H_{O_{2(T_o)}} \quad (34)$$

$$H_{C_{graphit(T_o)}} = -\Delta H_{f CO_{2(T_o)}} + H_{CO_{2(T_o)}} - H_{O_{2(T_o)}} \quad (35)$$

With the absolute enthalpy of the fuel mixture before combustion, obtained in this manner, the combustion temperature can be determined from the h-s diagram.

Figure 6 shows the result of such a calculation. The highest combustion temperature occurs in the range /18
$\bar{\lambda}$ = 0.85 to 0.9 for the oxygen carrier ratio.

For theoretical calculation of the state quantities during expansion, the following conditions are assumed:

1) Complete combustion. The exhaust gas consists of a homogeneous mixture of thermally complete gases. Negligible velocity at the nozzle entrance.
2) The gas state during expansion is determined by the entropy of the system, which shall remain unchanged in the pressure drop.

3) Unidimensional calculation of the flow processes.

4) Effects of friction, divergence angle, and heat transfer are neglected.

5) The liquid and solid components have negligible volumes and are in equilibrium with the gaseous combustion products.

The first major law of thermodynamics leads to the exhaust gas velocity.

$$w = \sqrt{2(h_1 - h_2)} \qquad (36)$$

Index: 1 = combustion chamber state, 2 = final state

The accuracy of h-s diagrams is generally adequate for graphic determination of power with chemical equilibrium. But, because the final expansion temperatures are also required in the current investigations, establishment of h-s-T diagrams (Figure 4) appeared expedient to avoid temperature interpolations.

Calculation of the course of expansion with frozen equilibrium presents no problems because of the constant exhaust gas composition. From the entgropy relation

$$s = s_{(T,\ p=1atm)} - \mathcal{R} \cdot \ln\left(\frac{p}{atm}\right) \qquad (37)$$

one obtains for various temperatures, on the basis of constant entropy:

$$s^{\circ}_{T_2} - s^{\circ}_{T_1} = \mathcal{R} \cdot \ln\left(\frac{p_2}{p_1}\right) \qquad (38)$$

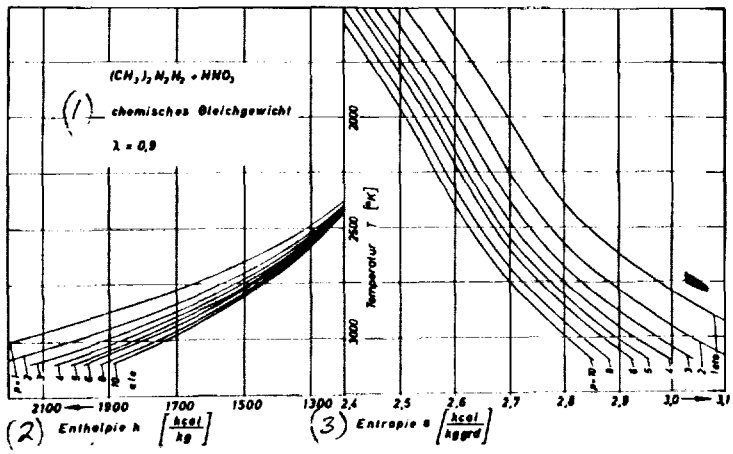

/19

Figure 4. h-s-T diagram for chemical equilibrium.

1. chemical equililbrium
2. Enthalpy
3. Entropy

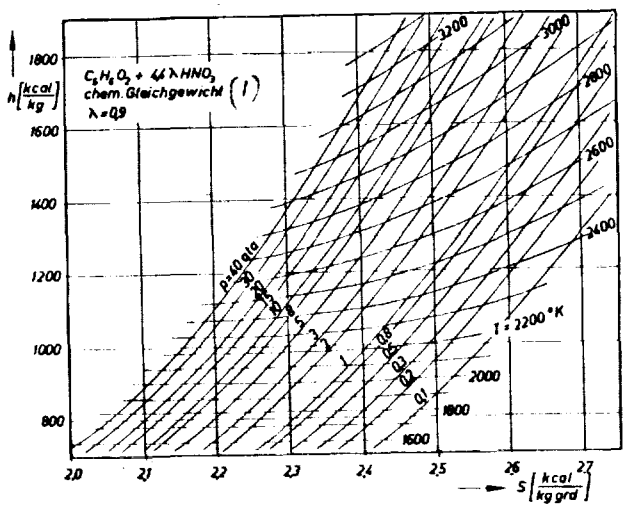

Figure 5. h-s diagram for chemical equilibrium

1. chemical equilibrium

For the final expansion pressure of a combustion gas, it follows from (38) that: /20

$$p_2 = p_1 \cdot e^{\frac{1}{R}\left[(\sum r_i \cdot s_i)^0_{T_2} - (\sum r_i \cdot s_i)^0_{T_1}\right]} \qquad (39)$$

The matching gas velocities are calculated from the enthalpy difference, while the specific volume is calculated by means of the gas equation using the gas composition and the total number of moles at the combustion chamber state.

Analysis of recombination effects in the expansion flow also requires accurate knowledge of all state quantities even for the limiting case of chemical equilibrium. Use of graphic interpolation methods; e. g., using the h-s diagram, is not satisfactory here.

As it was not possible to develop an extensive program for calculation of equilibrium expansion, the chemical equilibrium is determined by sampling for the fuels studied at many points during the expansion at constant entropy. The temperatures input to the computer at the desired pressure are changed until the condition $\Delta s = 0$ is met.

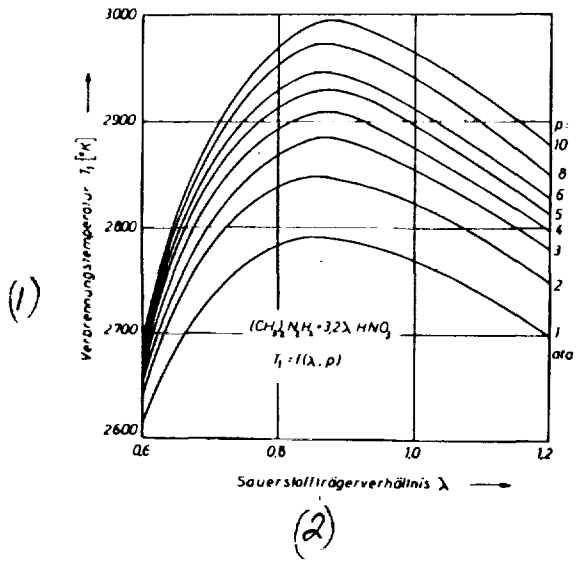

Figure 6. Theoretical combustion temperature.

1. Combustion temperature
2. Oxygen carrier ratio

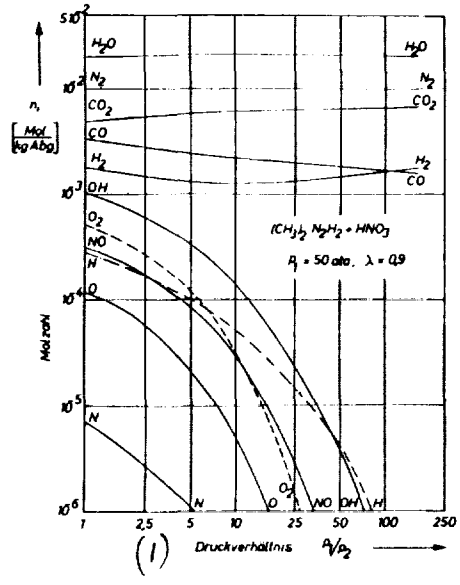

/21

Figure 7. Exhaust gas composition during expansion, chemical equilibrium.

1. Pressure ratio

Along with the state quantities, one also determines the exhaust gas composition during expansion in this manner, assuming chemical equilibrium. As Figure 7 shows for the example of the fuel mixture UDMH + HNO_3 at an oxygen carrier ratio of $\lambda = 0.9$ and a combustion chamber pressure of $p_1 = 50$ atm, the number of moles for the end products of complete combustion (e. g., H_2O, CO_2) increases with increasing expansion, while the atoms and radicals, which occur in relatively high concentration in the combustion chamber vanish relatively rapidly on expansion. This phenomenon is due to the strong temperature dependence of the equilibrium composition.

b. Determination of the specific heat and the sonic velocity for chemical equilibrium

Numerical calculation of the specific heat and the sonic velocity at chemical equilibrium is a necessary basis for application of an approximation method for the actual course of expansion. Various procedures are known for this [19, 24].

In particular, the specific heats can be determined, /22
including heats of reaction, by matrix multiplications, which can be done using fast digital computers even for multicomponent mixtures . Sänger-Bredt [23], for instance, used the differential quotients $(\delta \ln n_i/\delta \ln T)_p$ to calculate c_p values for chemical equilibrium. This quantity, though, could not be determined with the computer program available at the Institute [3]. For this reason, a different computer program was developed, which can be combined with the present program to determine equilibrium composition.

The absolute specific enthalpy of a reacting gas is represented by:

$$h' = \sum_{i=1}^{m} n_i H_i \qquad (40)$$

where m indicates the number of materials in the gas mixture.

One gets the specific heat from:

$$c_p' = \left(\frac{\partial h'}{\partial T}\right)_p = \sum_{i=1}^{m} n_i \left(\frac{\partial H_i}{\partial T}\right)_p + \sum_{i=1}^{m} H_i \left(\frac{\partial n_i}{\partial T}\right)_p \qquad (41)$$

The first summand in Equation (41) corresponds to the specific heat for the frozen reaction, while the second considers the change of gas composition. The latter can be split into two parts:

a) into the elementary chemically independent reactions (j) which determine the chemical equilibrium, the number of which is a = m - e (e = number of chemical elements).

b) into a frequency factor, or a reaction course number, E, which indicates how often the elementary chemical reaction (j) must occur during the change of the gas state in order for the chemical equilibrium of the entire system to be achieved.

The elementary, chemically independent reactions (j) are represented by

$$\sum_{i=1}^{m} \nu_i' Z_i = 0 \qquad \text{with } j = 1, 2, 3, \ldots a.$$

Here Z_i is the chemical symbol for the i-th component of the mixture and ν_i' is the stoichiometric number of moles /23

of this component in the j-th reaction. For the component i, which does not appear in the j-th reaction, $\nu_i^j = 0$.

Table 2 gives the stoichiometric number of moles for the 11 exhaust gas components and the 7 chemically independent reactions.

Table 2. Stoichiometric numbers of moles

ν_i^j (i \ j)	O	O_2	H	H_2	OH	H_2O	N	N_2	NO	CO	CO_2	$\Delta\nu^j$
O_2	-2	1	-	-	-	-	-	-	-	-	-	-1
H_2	-	-	-2	1	-	-	-	-	-	-	-	-1
OH	-1	-	-1	-	1	-	-	-	-	-	-	-1
H_2O	-1	-	-2	-	-	1	-	-	-	-	-	-2
N_2	-	-	-	-	-	-	-2	1	-	-	-	-1
NO	-1	-	-	-	-	-	-1	-	1	-	-	-1
CO_2	-1	-	-	-	-	-	-	-	-	-1	1	-1

Through consideration of these reactions, a change of exhaust gas composition can be expressed, depending on the stoichiometric mole number ν_i^j and the frequency factor E by the relation:

$$dn_i = \sum_{j=1}^{q} \nu_i^j \, dE^j$$

Thus one gets:

$$c_p^r = c_p + \sum_{i=1}^{m} H_i \cdot \sum_{j=1}^{q} \nu^{j\,\prime} \left(\frac{\partial E^j}{\partial T}\right)_p \qquad (42)$$

By exchanging the sequence of summation it follows from (42) that:

$$c_p^r = c_p + \sum_{j=1}^{g} \left[\sum_{i=1}^{m} \nu_i^j H_i \right] \left(\frac{\partial E^j}{\partial T} \right)_p \qquad (43)$$

The expression in the square brackets corresponds to the heat of reaction, ΔH^j, , i. e., ;the change of enthalpy on formation of the combustion products from the previously existing components with constant values for pressure and temperature. /24

The unknown partial derivative $(\delta E^j / \delta T)_p$ depends on the gas composition, the temperature, and the pressure of the system, and is determined from the equilibrium constants of the elementary reactions that occur:

$$\ln K_p^j = \sum_{i=1}^{m} \nu_i^j \ln P_i \qquad (44)$$

With

$$P_i = \frac{n_i}{\sum_{i=1}^{m} n_i} P$$

and

$$\sum_{i=1}^{m} \nu_i^j = \Delta \nu^j$$

one obtains

$$\ln K_p^j = \Delta \nu^j \ln n_i + \Delta \nu^j \ln P - \Delta \nu^j \ln \sum_{i=1}^{m} n_i \qquad (45)$$

The van't Hoff relation is assumed to be valid for the dependence of the rate constants on the temperature [71]:

$$\frac{d \ln K_p}{dT} = \frac{\Delta H^l}{\mathcal{R} \cdot T^2} \qquad (46)$$

By differentiating (45) with respect to temperature and inserting of (46) one obtains

$$\frac{\Delta H^l}{\mathcal{R} \cdot T^2} = \sum_{i=1}^{m} \left[\frac{\nu_i^l}{n_i} \left(\frac{\partial n_i}{\partial T} \right)_p \right] - \frac{\Delta \nu^l}{\sum_{i=1}^{m} n_i} \left(\frac{\partial \sum_{i=1}^{m} n_i}{\partial T} \right)_p$$

or

$$\frac{\Delta H^l}{\mathcal{R} \cdot T^2} = \sum_{i=1}^{m} \left(\frac{\nu_i^l}{n_i} - \frac{\Delta \nu^l}{n_{ges}} \right) \left(\frac{\partial n_i}{\partial T} \right)_p \qquad (47)$$

On introduction of the frequency factor into (47) one gets an equation, from which the unknown partial derivatives can be determined. /25

$$\frac{\Delta H^l}{\mathcal{R} \cdot T^2} = \sum_{i=1}^{m} \left(\frac{\nu_i^l}{n_i} - \frac{\Delta \nu^l}{n_{ges}} \right) \sum_{j=1}^{q} \nu_i^j \left(\frac{\partial \varepsilon^j}{\partial T} \right)_p \qquad (48)$$

In matrix notation, with $\mathcal{Y} = \sum_{i=1}^{m} \left(\frac{\nu_i^l}{n_i} - \frac{\Delta \nu^l}{n_{ges}} \right) \nu_i^j$

we get

$$\left\{ \left(\frac{\partial \varepsilon^j}{\partial T} \right)_p \right\} = \frac{1}{\mathcal{R} \cdot T^2} \left| \mathcal{Y} \right|^{-1} \cdot \left\{ \Delta H^l \right\} \qquad (49)$$

With this, (43) can be changed to:

$$c_p^f = c_p + \frac{1}{\bar{R} \cdot T^2} \left| \Delta H^j \right| \cdot \left| \mathcal{V} \right|^{-1} \cdot \left| \Delta H^j \right| \qquad (50)$$

The specific heat at constant pressure and chemical equilibrium is determined with (50) for the known exhaust gas composition and the heats for formation for the individual reactions. Multiplication of the inverse matrix $|\mathcal{V}|^{-1}$ with the column vector $|\Delta H^j|$ and the row vector $|\Delta H^j|$ is done using a program for the Siemens 2002 digital computer.

The specific heat at constant volume can be calculated similarly. In this case the starting equation is:

$$c_v^f = \left(\frac{\partial U}{\partial T}\right)_v = c_v + \sum_{j=1}^{n} \Delta U^j \left(\frac{\partial E^j}{\partial T}\right)_v \qquad (51)$$

With $H = U + \bar{R} \cdot T$ one obtains:

$$\Delta U^j = \Delta H^j - \Delta \nu^j \bar{R} T \qquad (52)$$

By introducing $p_i = n_i \cdot \bar{R} \cdot T / V$, (44) is changed to:

$$\ln K_p^j = \sum_{i=1}^{m} \nu_i^j \ln n_i + \Delta \nu^j \ln \frac{\bar{R} \cdot T}{V} \qquad (53)$$

Differentiation with respect to T and insertion of (46) /26 gives:

$$\frac{\Delta H^j}{\mathcal{R}\cdot T^2} = \sum_{i=1}^{m}\left[\frac{\nu_i^j}{n_i}\left(\frac{\partial n_i}{\partial T}\right)_v\right] + \frac{\Delta\nu^j}{T} \qquad (54)$$

or, after inserting the relation for the frequency factor:

$$\frac{1}{\mathcal{R}\cdot T^2}\left(\Delta H^j - \cdot T\cdot\Delta\nu^j\right) = \sum_{i=1}^{m}\left[\frac{\nu_i^j}{n}\sum_{j=1}^{q}\nu_i^j\left(\frac{\partial E^j}{\partial T}\right)_v\right] \qquad (55)$$

With the matrix $[\zeta] = \sum_{i=1}^{m}\frac{\nu_i^j}{n_i}\nu_i^j$, the a equations (55) change, in matrix notation, into:

$$\left[\left(\frac{\partial E^j}{\partial T}\right)_v\right] = \frac{1}{\mathcal{R}\cdot T^2}[\zeta]^{-1}\cdot\left[\Delta H^j - \mathcal{R}\cdot T\Delta\nu^j\right] \qquad (56)$$

Combining (51) with (52) and (56) gives the specific heat at constant volume as:

$$c_v' = c_v + \frac{1}{\mathcal{R}\cdot T^2}\left[\Delta H^j - \mathcal{R}\cdot T\Delta\nu^j\right]\cdot[\zeta]^{-1}\cdot\left[\Delta H^j - \mathcal{R}\cdot T\Delta\nu^j\right] \qquad (57)$$

The ratio of specific heats at chemical equilibrium follows from (50) and (57):

$$\varkappa' = \frac{c_p + \frac{1}{\mathcal{R}\cdot T^2}\left[\Delta H^j\right]\cdot[\zeta]^{-1}\left[\Delta H^j\right]}{c_v + \frac{1}{\mathcal{R}\cdot T^2}\left[\Delta H^j - \mathcal{R}\cdot T\Delta\nu^j\right]\left[\zeta\right]^{-1}\left[\Delta H^j - \mathcal{R}\cdot T\Delta\nu^j\right]} \qquad (58)$$

Calculation of the sonic velocity at chemical equilibrium is reduced to the relation

$$c^2 = \left(\frac{\partial p}{\partial \rho}\right)_s \qquad (59)$$

From the complete differentials of internal energy and enthalpy

$$du = c_v^r\, dT + \left(\frac{\partial u^r}{\partial v}\right)_T dv \qquad (60)$$ /27

$$dh = c_p^r\, dT + \left(\frac{\partial h^r}{\partial p}\right)_T dp \qquad (61)$$

and from the First Law at constant entropy

du = - pdv and dh = vdp it follows that:

$$\left[c_v^r \cdot dT + \left[\left(\frac{\partial u^r}{\partial v}\right)_T + p\right] dv\right]_s = 0 \qquad (62)$$

$$\left[c_p^r \cdot dT + \left[\left(\frac{\partial h^r}{\partial p}\right)_T - v\right] dp\right]_s = 0 \qquad (63)$$

With $\varkappa^r = c_p^r / c_v^r$ we have, from (62) and (63):

$$\varkappa^r = \frac{\left[\left(\frac{\partial h^r}{\partial p}\right)_T - \frac{1}{\rho}\right]}{\left[\left(\frac{\partial u^r}{\partial v}\right)_T + p\right]} \cdot (-\rho^2) \cdot \left(\frac{\partial p}{\partial \rho}\right)_s \qquad (64)$$

or

$$\left(\frac{\partial p}{\partial \rho}\right)_s = c^2 = \kappa^r \cdot \mathcal{R} \cdot T \cdot n_{gas} \cdot \frac{\left[1 + \frac{1}{p}\left(\frac{\partial u^r}{\partial v}\right)_T\right]}{\left[1 - \rho\left(\frac{\partial h^r}{\partial p}\right)_T\right]} \qquad (65)$$

Using the frequency factor, explained above in more detail, the partial derivatives in (65) are determined similarly as for the derivation of the specific heat c_p^r in matrix notation as

$$\frac{1}{p}\left(\frac{\partial u^r}{\partial v}\right)_T = \frac{1}{\mathcal{R} \cdot T}\left[\Delta H^l - \mathcal{R} \cdot T \Delta v^l\right] \cdot \left[\psi\right]^{-1} \cdot \left[\Delta v^l\right] \qquad (66)$$

and /28

$$\rho\left(\frac{\partial h^r}{\partial p}\right)_T = -\left[\frac{\Delta H^l}{\mathcal{R} \cdot T}\right] \cdot \left[\vartheta\right]^{-1} \cdot \left[\Delta v^l\right] \qquad (67)$$

With this, (65) can be converted into

$$c = \sqrt{\kappa^r \cdot \mathcal{R} \cdot T \cdot n_{gas} \frac{\mathcal{R} \cdot T + \left[\Delta H^l - \mathcal{R} \cdot T \Delta v^l\right] \cdot \left[\psi\right]^{-1} \cdot \left[\Delta v^l\right]}{\mathcal{R} \cdot T + \left[\Delta H^l\right] \cdot \left[\vartheta\right]^{-1} \cdot \left[\Delta v^l\right]}} \qquad (68)$$

or

$$c = \sqrt{\kappa^r \cdot \mathcal{R} \cdot T \cdot n_{gas} \cdot \mathcal{U}} \qquad (69)$$

where we have

$$\mathcal{U} = \frac{\mathcal{R} \cdot T + \left[\Delta H^l - \mathcal{R} \cdot T \Delta v^l\right] \cdot \left[\psi\right]^{-1} \cdot \left[\Delta v^l\right]}{\mathcal{R} \cdot T + \left[\Delta H^l\right] \cdot \left[\vartheta\right]^{-1} \cdot \left[\Delta v^l\right]}$$

c. Determination of mean isentropic exponents in nozzle flows

Usually enthalpy-entropy diagrams or enthalpy-temperature and entropy-temperature diagrams are used to determine velocities, specific impulses, and other values of exhaust gases in the nozzle flow. Such diagrams can be established only by use of electronic computers. It would be simpler, for instance, to use the expansion velocity formula (2) for the determination. If one assumes that T_1 and M_1, the conditions in the combustion chamber, are known, then only the coefficient $\bar{\kappa}$ is unknown. But $\bar{\kappa}$ is not a constant value. It depends on the course of the state during expansion, so that the exact relations cannot be determined by relations which contain the isentropic exponent. The usefulness of approximation equations to determine power characteristic data depends on the choice of useful values for the isentropic exponents. The strong temperature drop /29 during the expansion requires averaging.

With the assumption of frozen expansion flow the averages are generally based on the states in front of and behind the nozzle. From the definition of the specific heat $c_p \cdot dt = dH$ the following isentropic exponent can be obtained [19]:

$$\bar{\kappa}_1 = \frac{\frac{h_1 - h_2}{T_1 - T_2}}{\frac{h_1 - h_2}{T_1 - T_2} - \mathfrak{R} \cdot \sum n_1} \qquad (70)$$

On the other hand, the average derived from the isentropic equation is:

$$\bar{\kappa}_2 = \frac{\ln(P_1/P_2)}{\ln(P_1/P_2) - \ln(T_1/T_2)} \qquad (71)$$

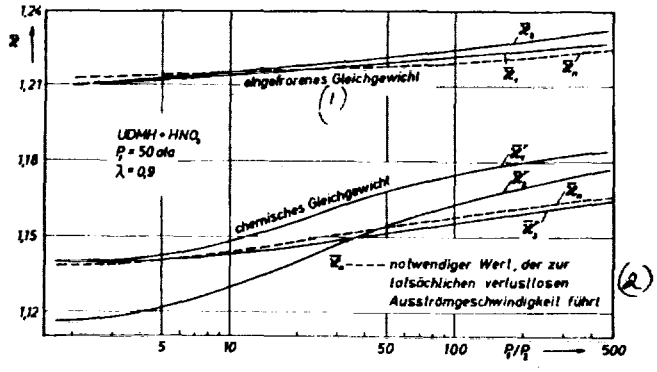

Figure 8. Comparison of different isentropic exponents in the nozzle flow.

1. frozen equilibrium
2. necessary value which leads to the actual loss-free exhaust velocity

The exponents calculated from (70) and (71) for the /30 expansion flow of a conventional fuel are shown in Figure 8. For comparison, the value of $\bar{\kappa}_s$ from Equation (2) is plotted also. It is required to determine the actual exhaust velocity for frozen equilibrium. (Here, w_s was determined using a digital computer.) According to this, Equation (70) is the best approximation.

On consideration of the chemical equilibrium the averaging becomes less reliable because of the sharp change of the $\varkappa$ value during the expansion.

If one introduces the mean change of the molar mass determined from the isentropic relation, then we get, for 2 state points considered:

$$\ln p_1 + \bar{\varkappa}' \ln \frac{T_1}{M_1 \cdot p_1} = \ln p_2 + \bar{\varkappa}' \ln \frac{T_2}{M_2 \cdot p_2} \qquad (72)$$

or

$$\bar{\varkappa}_1' = \frac{\ln(p_1/p_2)}{\ln(p_1/p_2) - \ln(T_1/T_2) + \ln(M_1/M_2)} \qquad (73)$$

As Figure 8 shows, $\bar{\varkappa}_1'$ is too large in comparison with the value provided at high pressure ratios.

Even the exponent $\bar{\varkappa}_2'$ determined without consideration of the change in number of moles ($M_1 = M_2$) gives no good agreement with $\bar{\varkappa}_s$ for chemical equilibrium. These results were found at various oxygen carrier ratios and combustion chamber pressures.

Because of the values of $\bar{\varkappa}_1'$ rising excessively with increasing pressure ratio, averaging was undertaken with the ratios at the nozzle throat and at the final cross section according to the relation

$$\bar{\varkappa}_3' = \frac{(\bar{\varkappa}_1')_{\text{critcal}} + (\bar{\varkappa}_1')_{\text{nozzle cross section}}}{2} \qquad (74)$$

The deviations of this mean from the required quantity are relatively minor. (See Figure 8.)

The best averages for a fuel combination consisting of the /31 atoms C - O - H - N are plotted for comparison in Figure 9 for various operating conditions.

While an increase in combustion chamber pressure leads to higher values of κ at chemical equilibrium, the situation is the reverse for frozen equilibrium. The effect of the pressure ratio, P_1/P_2 is nearly constant in the entire range for both expansion hypotheses.

The lower combustion temperature at lower oxygen carrier ratios, with its lower dissociation losses, leads, at chemical equilibrium, to an approximation of the κ value for the frozen flow.

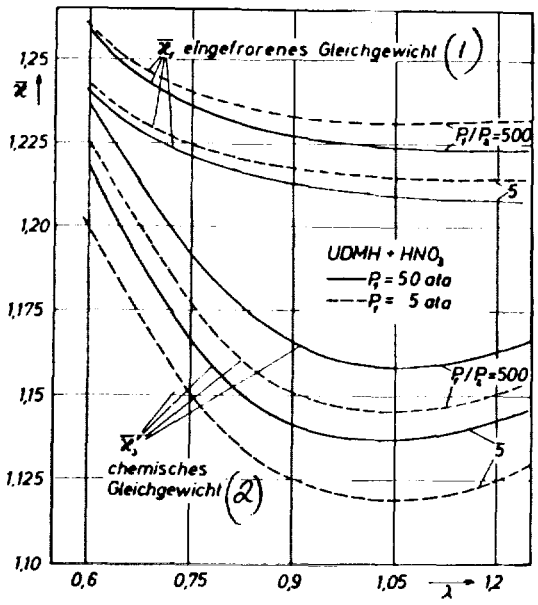

Figure 9. Effect of the operating conditions on the average isentropic exponents.

1. frozen equilibrium
2. chemical equilibrium

The large variations of the isentropic exponents ($1.12 < \bar{\varkappa}$ /32 or $\bar{\varkappa} < 1.26$) as they depend on the operating parameters (λ, P_1, P_1/P_2) and the type of expansion prevents general use of this value for calculation of nozzle flows of hot combustion gases without knowledge of the thermodynamic state values, even though the desired results are expected only to be of the nature of a crude approximation. For C - O - H - N systems, such a calculation at λ values of 0.8 can be based on $\bar{\varkappa}' = 1.15$ for chemical equilibrium and $\bar{\varkappa} = 1.22$ for frozen equilibrium [10, 25].

d. Calculation of the characteristic velocity

The characteristic velocity means that for a specified narrowest cross section and constant combustion chamber pressure, fuel combinations with a larger c* value require a smaller amount of fuel to produce the same combustion chamber pressure.

As the characteristic velocity is affected by the conditions in the narrowest cross section, one gets different values depending on the kind of expansion. Equation (8) can only produce correct results if accurate statements are possible about $\bar{\kappa}$ or $\bar{\kappa}'$ corresponding to the velocities occurring at the critical point. The relations (2) and (36) are used for the fuel pair investigated. By setting equal, these give:

$$\frac{h_1 - h_{krit}}{\sum n_i \cdot \bar{R} \cdot T_1} = \frac{\bar{\kappa}}{\bar{\kappa}-1}\left[1 - \left(\frac{p_{krit}}{p_1}\right)^{\frac{\bar{\kappa}-1}{\bar{\kappa}}}\right] \qquad (75)$$

index: "crit" = narrowest cross section.

As the values of $\bar{\kappa}$ obtained using (75) lead to the exact velocity, they can also be inserted into Equation (8). The calculation of c* is then reduced to determination of a suitable exponent $\overline{\bar{\kappa}}$. To ease the numerical calculation, a diagram corresponding to Figure 10 is set up according to (8). From the values of T_1 and M_1, which are well known from the specified combustion chamber state, the characteristic velocity can be determined. The results shown in Figure 11 show different values depending on the expansion hypothesis, with values being higher for chemical equilibrium by Δc^* = 30 to 40 m/s. The highest c* value is obtained at oxygen carrier ratios of λ = 0.7 to 0.8. As a result, this mixture ratio is used in practice.

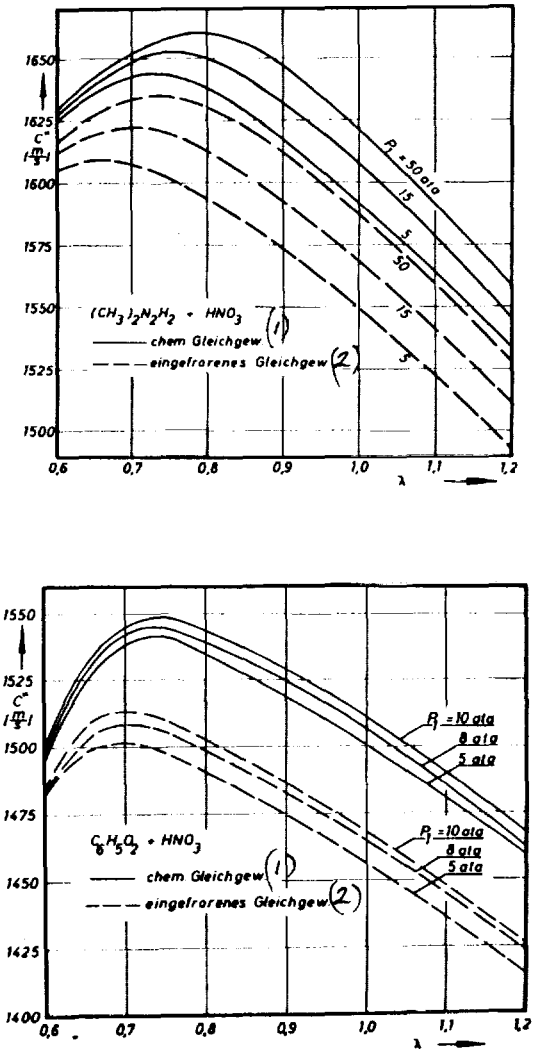

/33

Figure 11. Curve for the characteristic velocity

1. chemical equilibrium
2. frozen equilibrium

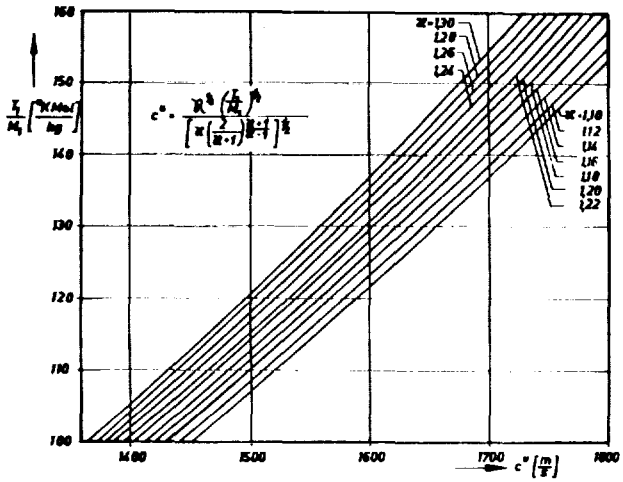

/34

Figure 10. Nomogram to determine the characteristic velocity.

The dependence of the characteristic velocity on the operating conditions, shown in Figure 11, is required in the framework of this work for comparison with the experimental investigations.

e. Effect of metal admixtures on the specific impulse

To attain higher specific engine powers, people have attempted to make the combustion temperature high and the molar mass of the exhaust gases low according to formula (2). Therefore, the elements of the first and second rows of the periodic system are used preferentially as fuels. Along with hydrogen, the hydrocarbons and the nitrogen-hydrogen compounds have attained special practical importance. But even the lighter metals and metal hydrides are of interest as fuels [1]. In particular, the high /35
heats of combustion of the metals causes additional heating of the reaction gases, so that the exhaust velocity and,

with it, the specific impulse are increased. But the metal oxides resulting in the reaction make only an insignificant contribution to the increase in thrust, as they cannot be discharged in the Laval nozzle because of their high melting temperatures.

In order to determine the extent of the increase in power, the theoretical specific impulse was determined and plotted in Figure 12 for two fuel combinations with added aluminum. At 15% added metal an increase of the optimum specific impulse by about 8 Kp·s/Kg or 2.7% can be attained. The necessary oxygen carrier ratio shifts to lower values with increasing metal concentration. In a theoretical study, Gordon et al. have determined that higher specific impulses can be attained by addition of metals than in the best two-material systems such as $H_2 + F_2$ [26].

The problems in application are mainly in the production of the metal suspensions. Our own attempts in this direction are discussed in Section C 5 a; but it should be mentioned here that because of difficulties in supplying the fuel, only metal concentrations up to 3% could be tested in the combustion chamber test stand.

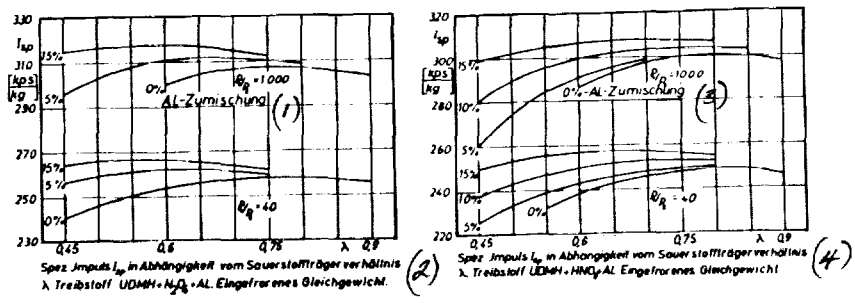

Figure 12. Calculated power increase by addition of aluminum.

1. Aluminum added
2. Specific impulse I_{sp} as a function of the oxygen carrier ratio, λ . Fuel UDMH + N_2O_4 + Al. Frozen equilibrium.
3. % Aluminum added
4. Specific impulse I_{sp} as a function of the oxygen carrier ratio, λ . Fuel UDMH + HNO_3 + Al. Frozen equilibrium

3. Actual course of reaction during expansion of hot combustion gases in Laval nozzles /36

a. Recombination processes and their significance for engine power

With energy conversion in the temperature region above 2500°K the reaction kinetic processes in the combustion gas have a great effect. For the theoretically calculated exhaust velocity from a nozzle, two different values can be obtained, depending on whether one does the calculation assuming that the gas composition present in the combustion chamber at the combustion temperature, which corresponds to

that for chemical equilibrium in the combustion chamber, is held the same during expansion in the nozzle (frozen equilibrium) or assuming that the particular equilibrium state is adjusted infinitely rapidly during expansion in the nozzle ("equilibrium flow") [13, 27].

For equilibrium flow, the energy present in the combustion chamber from the dissociation of molecules is liberated again during the expansion by recombination reactions, corresponding to the falling temperature. This process is called recombination. The gas exhaust velocity is, therefore, higher for equilibrium flow than for frozen flow. The difference between the two velocities becomes greater the higher the proportion of the dissociated molecules with the corresponding fuel combination; that is, the higher the combustion temperature is. The full chemical energy is only added to the flow if recombination of the dissociated elements without reaction occurs on decrease of temperature and pressure.

In a real expansion flow, chemical and gas-dynamic processes interact. The reactions proceed according to reaction kinetic laws with a time delay. The reaction rates affect the flow not only through the gas composition, but also influence the reaction itself by the path through the temperature.

Likewise, the changes in the state values caused by the nozle produce changes in the course of the reaction rates. Utilization of the energy liberated in the nozzle by recombination depends decisively on whether the recombination rate is so high that recombination can be complete during the very short residence time of the

combustion gases in the nozzle. The real expansion flow /37 will, therefore, always lie between the two limiting cases of "frozen equilibrium" and "chemical equilibrium" [28, 29].

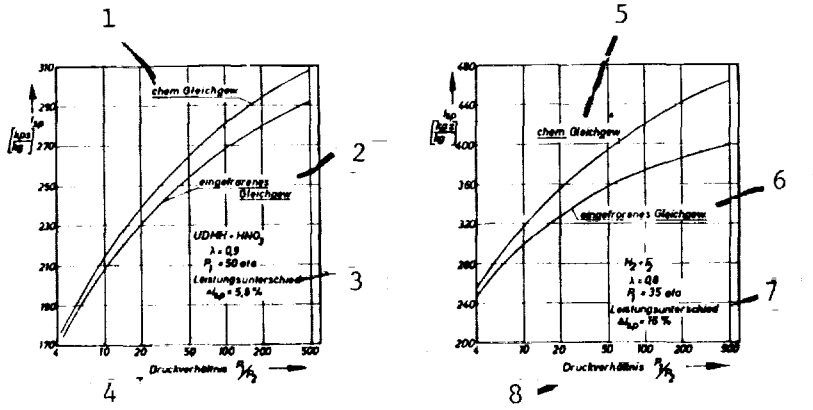

Figure 13. Power comparison assuming different expansion hypotheses.

a. conventional fuel b. high-energy fuel

1. chemical equilibrium
2. frozen equilibrium
3. power difference
4. pressure ratio
5. chemical equilibrium
6. frozen equilibrium
7. power difference
8. pressure ratio

Figure 13 shows that the calculated power difference from the assumption of different expansion hypotheses can be considerable for highly energetic fuel combinations, so that the calculation for the limiting case is not sufficient for an optimal engine design [2].

It can be seen from comparison of Figures 13 a and 13 b that for conventional fuels the difference remains within tolerable limits. Usually a design based on frozen

equilibrium has been considered adequate for these systems, especially because of their use as a base engine. In addition, this calculation is far simpler to carry out than the one with recombination processes included.

The problem of the nozzle flow with coupled chemical reactions is solved by means of fast digital computers, using the gas dynamic and reaction kinetic equations. The problems of accurate computer treatment lie, for one thing, in the mathematical complexity of the reaction kinetic processes resulting from a large number of mutually dependent and independent reactions. For another thing, the problems are due to the unreliability of many reaction kinetic data, especially of the rate constants of the /38 recombination reactions [7, 13].

b. Setting up and solving a system of equations for coupled chemical reactions

In a Laval nozzle, the thermal energy of a resting gas is converted into the kinetic energy of a supersonic flow. Assuming a unidimensional, isotropic, frictionless and non-ionized flow, the thermodynamic state values are calculated for a gas mixture consisting of many components by considering nonequilibrium effects. In order to be able to describe completely the course of such a chemical process, one must know not only the reaction rate but also the reaction path. Only in rare cases does this lead directly from the starting to the final materials according to the over-all conversion equation. Usually there are intermediate products.

Occasionally investigations have been done on chemically simple systems for which the kinetic data are adequately known [5, 29, 32].

In particular, H. Heitland has presented the relations for equilibrium expansion. Considering a finite reaction rate for a single reaction, and using an iodine-argon gas mixture as an example, he has shown the actual course of the flow as a function of the operating parameters and the nozzle geometry. He was able to indicate some important values influencing the recombination process [5].

The comparison done by H. Heitland, of approximation processes with the exact calculation of the flow, for the iodine recombination as an example, showed a strong dependence of the degree of dissociation at the end of the nozzle on the initial pressure and the nozzle geometry. Finally, transition from chemical equilibrium flow to frozen flow can be determined approximately using the freeze-in criterion.

For the technological fuels used in this work, the degree of dissociation can generally be used no more than as a characteristic value because several reactions with different reaction rates proceed simultaneously. The equations must, then, be formulated generally. The solution is determined using a high-powered digital computer.

By using the approximation procedure according to Section B 3 c, the freeze-in point is not assumed to be in the nozzle throat, in comparison with H. Heitland. Rather, one seeks the freeze-in point within the nozzle, under the assumptions of the approximation solution. Thus, the state values occurring at the end of the nozzle are established. The comparison between approximation and exact solution at a given expansion ratio makes possible evaluation of the usefulness of the approximation process. /39

In calculations for multicomponent systems, there are certain uncertainties with respect to selection of the correct reaction equations and rate constants [31, 33, 34]. On the other hand, problems arise because of the singularity of the kinetic equations on integration out of the chemical equilibrium.

Paths for solution of this problem have been shown, however, by the works of Zupnik et al. under contract with NASA.

The considerations within this work refer to a fuel system with the chemical elements C, O, H and N. The following reactions between the assumed eleven exhaust gas components are considered to be sufficient [7]:

1)	$H_2 + OH \rightleftharpoons H_2O + H$	$K_1^{(1)} = 6{,}3 \cdot 10^{13} \cdot e^{-\frac{2970}{T}}$ $\frac{cm^3}{mol \cdot s}$
2)	$H + O_2 \rightleftharpoons OH + O$	$K_1^{(2)} = 1{,}7 \cdot 10^{16} \cdot T^{-0{,}37} \cdot e^{-\frac{9110}{T}}$ $\frac{cm^3}{mol \cdot s}$
3)	$H_2 + O \rightleftharpoons OH + H$	$K_1^{(3)} = 2{,}5 \cdot 10^{12} \cdot e^{-\frac{3880}{T}}$ $\frac{cm^3}{mol \cdot s}$
4)	$H + H + M \rightleftharpoons H_2 + M$	$K_1^{(4)} = 7 \cdot 10^{16} \cdot T^{-0{,}5}$ $\frac{cm^6}{mol^2 \cdot s}$
5)	$CO + OH \rightleftharpoons CO_2 + H$	$K_1^{(5)} = 5 \cdot 10^{12} \cdot e^{-\frac{3520}{T}}$ $\frac{cm^3}{mol \cdot s}$
6)	$N_2 + O \rightleftharpoons NO + N$	$K_1^{(6)} = 5 \cdot 10^{13} \cdot e^{-\frac{38000}{T}}$ $\frac{cm^3}{mol \cdot s}$
7)	$O_2 + N \rightleftharpoons NO + O$	$K_1^{(7)} = 10^{11} \cdot T^{0{,}5} \cdot e^{-\frac{3120}{T}}$ $\frac{cm^3}{mol \cdot s}$
8)	$H + OH + M \rightleftharpoons H_2O + M$	$K_1^{(8)} = 3 \cdot 10^{19} \cdot T^{-1}$ $\frac{cm^6}{mol^2 \cdot s}$
9)	$O + O + M \rightleftharpoons O_2 + M$	$K_1^{(9)} = 2 \cdot 10^{19} \cdot T^{-1{,}5}$ $\frac{cm^6}{mol^2 \cdot s}$
10)	$NO + M \rightleftharpoons N + O + M$	$K_1^{(10)} = 7 \cdot 10^{15} \cdot e^{-\frac{75600}{T}}$ $\frac{cm^3}{mol \cdot s}$
11)	$O_2 + N_2 \rightleftharpoons 2\,NO$	$K_1^{(11)} = 2{,}7 \cdot 10^{13} \cdot e^{-\frac{53900}{T}}$ $\frac{cm^3}{mol \cdot s}$

The following fundamental equations are required for the computer treatment:

Continuity relation $$\rho \cdot w \cdot F = M_s \tag{76}$$

Motion equation $$w \cdot dw + \frac{1}{\rho} dP = 0 \tag{77}$$

Energy equation $$h_1 = h_2 + \frac{w^2}{2} \tag{78}$$

Gas equation $$P = \rho \cdot \mathcal{R} \cdot T \sum n_i \tag{79}$$

The change in concentration of material Z_i is represented by:

$$\left(\frac{\partial [Z_i]}{\partial t}\right)_p = \sum_{r=1}^{N} (\nu_i'' - \nu_i') \cdot \left\{ K_1^{(r)} \prod_{j=1} [Z_j]^{\nu_j'} - K_2^{(r)} \prod_{j=1} [Z_j]^{\nu_j''} \right\} \tag{80}$$

in which:

ν_i', ν_i'' are the stoichiometric coefficients for the component i in the reaction l

$K_1^{(r)}, K_2^{(r)}$ are the reaction rates for the forward and back reactions for reaction l

N is the total number of chemical reactions

m is the total number of exhaust gas components.

Equations (76) to (80) relate the quantities necessary for determining the gas flow with relaxation.

A basic program established by NASA [7] could be worked up and used for solution of this system of equations, because

the fast IBM 7094 digital computer at the German Computer Center in Darmstadt was available.

For given nozzle geometry, in carrying out the calculation an initial point is sought in the convergent part of the nozzle where the flow begins to deviate from chemical equilibrium. As the first computer results showed, correct choice of the initial point assumes some experience. That is, if the flow proceeds in chemical equilibrium at the beginning of the computation, the necessary computer time is very high because the program is not designed for expansion at chemical equilibrium. If the flow already deviates considerably from chemical equilibrium at the initial point of the computation, then the computer result becomes very inaccurate because the initial point is entered as an equilibrium state from the result of the Aachen computer. This equilibrium state, though, is no longer present.

The expansion courses were computed for the fuel combination UDMH + HNO_3 for combustion chamber pressures of P_1 = 50 atm and 5 atom, and for the mixture ratios $\bar{\lambda}$ = 0.6, 0.9 and 1.2, assuming a finite reaction rate. In this way the effect of the pressure and the oxygen carrier ratio on the actual course of the flow can be shown. The results of this computation are shown in Figures 16 to 23, 59, and 60. They are discussed, in comparison with the other expansion hypotheses, in Sections B 3 e and C 6 b.

c. Development of an approximation process to determine the expansion course for the fuel pair UDMH + HNO_3

In order to reduce the computing cost needed for exact determination of the real course of expansion during the flow of hot combustion gases through Laval nozzles, several approximation methods have been developed [27, 35, 36].

The usefulness and the limits of applicability have been discussed in various works [5, 7, 9]. In evaluation of all approximation methods one must take into consideration the fact that the accuracy of the exact computation also depends strongly on the reliability of the kinetic data. For instance, if the difference of the specific impulse between the chemical and frozen equilibrium is 8%, then an approximation with uncertainty limited to 2% is usable. The accurate computation generally has an uncertainty of about 1% even with a substantial increase in computing cost.

Usable results have been obtained so far with the Bray approximation method [35], which in most cases considers only one reaction [31, 33]. /42

Within this work, the method was extended to several reactions proceeding simultaneously, which can increase the accuracy.

Bray defined a freeze-in point within a transition region in the nozzle, in which the combustion gas changes from equilibrium flow to frozen-in flow. The problem of the nozzle flow with chemical ractions is, then, reduced to the more simply calculated limiting case with a known freeze-in point. The freeze-in point is characterized by a constant, K_s. Here the constant is

$$K_R = \frac{\text{rate of change of the equilibrium composition}}{\text{rate of the recombination reactions}} \qquad (81)$$

The numerator in (81) says how fast the gas composition must change in order to produce approximately equilibrium flow, while the denominator is a measure for the reaction rate limited by chemical kinetics. The flow occurs in quasi-chemical-equilibrium if the necessary rate of change of the equilibrium composition is low while the rate of the recombination reactions takes on large values. In the converse case there is quasi-frozen-in flow. The constant assumes different values. Its magnitude has been investigated by several researchers [29, 35, 36]. There is agreement in considering $K_R = 1$ as the best value, and this computation is based on that. The sensitivity of the results is also low with respect to selection of the value of K_R in the range $0.8 < K_R > 2.0$ [36]. *

* The symbol > in the original German text probably should be < .

The numerator in (81) is calculated with the assumption that the change of concentration $[Z_i]$ occurs only in the direction of the nozzle axis, and the flow is considered to be steady. If the density is considered to be approximately constant within the region considered, according to the deliberations of Bray [35], then there is a relation between the specific molar number n_i and the molar concentration $[Z_i]$ of the component Z_i:

$$[Z_i] = \rho \cdot n_i \qquad (82)$$

Then (82) yields the relation for the change of concentration at point x in the nozzle:

$$\left(\frac{\partial[Z_i]}{\partial t}\right)_p = \rho\frac{dn_i}{dt} = \rho\frac{dn_i}{dx}\cdot\frac{dx}{dt} = \rho\cdot w\cdot\frac{dn_i}{dx} \qquad (83)$$ /43

By introducing the dimensionless nozzle coordinate $\varepsilon = \frac{2x}{d}$, (83) is changed into:

$$\left(\frac{\partial[Z_i]}{\partial t}\right)_p = \frac{2\cdot\rho\cdot w}{d}\cdot\frac{dn_i}{d(\ln p)}\cdot\frac{d(\ln p)}{d(\ln F_i/F_{min})}\cdot\frac{d(\ln F_i/F_{min})}{d\varepsilon} \qquad (84)$$

The term $dn_i/d(\ln P)$ is obtained by graphic differentiation of the molar number curve for the component i under consideration.

From the continuity equation $d\rho/\rho + dF/F + dw/w = 0$ and the motion equation $w\cdot dw + 1/\rho\cdot dp = 0$ it follows that:

$$\frac{dF/F}{d\rho/\rho} = \frac{dp}{w^2 d\rho} - 1 \qquad (85)$$

With introduction of (59) and noting that Ma = w/c, (85) changes into:

$$\frac{dF/F}{d\rho/\rho} = \frac{1 - Ma^2}{Ma^2} \qquad (86)$$

The relation which is valid for chemical equilibrium of thermally complete gases follows from combination of (59) and (69):

$$\left(\frac{dp}{p}\right)_s = \left(\frac{d\rho}{\rho}\right)_s\cdot\frac{1}{\kappa'\cdot\psi} \qquad (87)$$

and with (87) there finally follows from (86):

$$\frac{d(\ln p)}{d(\ln F_i/F_{min})} = \frac{\kappa'\cdot\psi\cdot Ma^2}{1 - Ma^2} \qquad (88)$$

With Equation (88), (84) converts to: /44

$$\left(\frac{\partial[Z_i]}{\partial t}\right)_p = \frac{\psi\cdot 2\rho\cdot w\cdot\kappa' Ma^2}{d\cdot(1 - Ma^2)}\cdot\frac{dn_i}{d(\ln p)}\cdot\frac{F_{min}}{F_i}\cdot\frac{d(F_i/F_{min})}{d\varepsilon} \qquad (89)$$

The nozzle geometry must be specified for further calculation. Here we have selected a nozzle which is conical at each end, with a throat diameter of d = 0.03296 m.

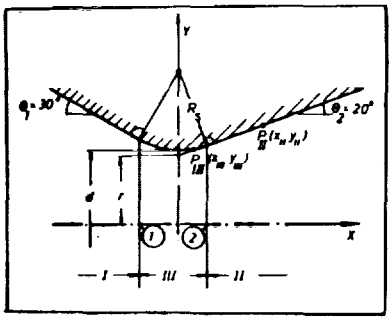

Figure 14: Nozzle geometry.

According to Figure 14, three regions, I to III, are distinguished within the nozzle. Their contours are established by the following relations:

I) $y_I = r' - x \cdot \operatorname{tg} \theta_1$

II) $y_{II} = r + x \cdot \operatorname{tg} \theta_2$

III) $y_{III} = d/2 + R_s - (R_s^2 - x^2)^{1/2}$

The area ratio for region II is represented by:

$$\frac{F_{II}}{F_{min}} = \frac{y_{II}^2}{(d/2)^2} = \frac{4}{d^2} \cdot (r + x \operatorname{tg} \theta_2)^2 \qquad (90)$$

After introduction of $\varepsilon = 2x/d$, differentiation of (90) gives

$$\frac{d(F_{II}/F_{min})}{d\varepsilon} = \frac{4r}{d} \cdot tg\,\theta_2 + 2\,tg^2\theta_2\,\varepsilon \qquad (91)$$

This relation is simplified by elimination of ε and by the use of (90) to:

$$\frac{d(F_{II}/F_{min})}{d\varepsilon} = 2 \cdot tg\,\theta_2 \sqrt{F_{II}/F_{min}} \qquad (92)$$

/45

Thus, (89) for region II becomes

$$\left(\frac{\partial(Z_i)}{\partial t}\right)_{II,\rho} = \frac{4 \cdot \rho w}{} \qquad (93)$$

(93) also applies for region I, if one replaces θ_2 with θ_1

The change of the area ratio can be obtained similarly for region III from the nozzle equation.

For this case, with an approximation based on a series expansion, we get

$$\frac{d(F_{III}\,F_{min})}{d\varepsilon} = \sqrt{\frac{2d}{R_s}\left[\left(\frac{F_{III}}{F_{min}}\right) - 1\right]} \qquad (94)$$

Then the change of concentration according to (89) is

$$\left(\frac{\partial(Z_i)}{\partial t}\right)_{III,\rho} = \frac{\dot{m}_i \cdot 2 \cdot \rho \cdot w \cdot \chi' \cdot Ma^2}{(1 - Ma^2)} \frac{dn_i}{d(\ln p)} \frac{F_{min}}{F_{III}} \sqrt{\frac{2}{R_s d}\left[\left(\frac{F_{III}}{F_{min}}\right) - 1\right]} \qquad (95)$$

For the narrowest cross section, (95) takes on an uncertain value because $(1 - Ma^2) = 0$. For this point, the solution can be found by using L'Hospital's rule [36].

$$\lim_{\substack{F/F_{min} \to 1 \\ Ma \to 1}} \frac{F/F_{min} - 1}{(1 - Ma^2)^2} = \frac{1}{2(1 - Ma^2)\,\frac{dMa^2}{d(F/F_{min})}} \qquad (96)$$

Then, using (88), one obtains:

$$\frac{dMa^2}{d(F/F_{min})} = \frac{dMa^2}{d(\ln P)} \frac{\varkappa \cdot Ma^2 \cdot \Re}{(1 - Ma^2)} \cdot \left(\frac{F_{min}}{F}\right) \tag{97}$$

Finally, by inserting (97) into (96), it follows that:

$$\lim_{\substack{F/F_{min} \to 1 \\ Ma \to 1}} \frac{F/F_{min} - 1}{(1 - Ma^2)^2} = \frac{1}{4 \cdot \varkappa \cdot p} \frac{dp}{dMa} \tag{98}$$

/46

Equation (95) then takes on the following form for the critical point:

$$\left(\frac{\partial [Z_i]}{\partial l}\right)_{krit.\bar{\rho}} = \frac{dn_i}{d(\ln P)} \sqrt{\frac{\Re^2 \cdot 2 \cdot (\varkappa^2 - 1) \cdot \rho}{R_s \cdot d} \left(\frac{dp}{dMa}\right)} \tag{99}$$

The generally applicable equation for the chemical conversion is [27, 37]:

$$\sum_{i=1}^{m} \nu_i' \cdot Z_i \underset{K_2^{(l)}}{\overset{K_1^{(l)}}{\rightleftharpoons}} \sum_{i=1}^{m} \nu_i'' \cdot Z_i \tag{100}$$

In (100), l = 1, 2, . . . N, where N = total number of reactions. For the change in molar number we have, for the steady case:

$$\rho \cdot w \cdot \frac{dn_i}{dx} = \sum_{l=1}^{N} (\nu_i'' - \nu_i') \left\{ K_1^{(l)} \prod_{j=1}^{m} \cdot (\rho \cdot n_j)^{\nu_j'} - K_2^{(l)} \prod_{j=1}^{m} \cdot (\rho \cdot n_j)^{\nu_j''} \right\} \tag{101}$$

On introduction of the reaction rates

$$K_1^{(l)} \prod_{j=1}^{m} \cdot (\rho \cdot n_j)^{\nu_j'} = R_1^{(l)} \tag{102}$$

and

$$K_2^{(l)} \prod_{j=1}^{m} \cdot (\rho \cdot n_j)^{\nu_j''} = R_2^{(l)} \tag{103}$$

(101) transforms into:

$$-\rho \cdot w \cdot \frac{dn_i}{dx} = \sum_{i=1}^{N} (\nu_i'' - \nu_i') \cdot R_i^{(l)} \left[1 - \frac{R_2^{(l)}}{R_1^{(l)}} \right] \qquad (104)$$

According to the definition the expression in the square brackets in Equation (104) is the Bray constant K_B [27]. /47

Then it follows, by combining (83) and (104) that:

$$K_B = \frac{\left(\frac{\partial [Z_i]}{\partial l}\right)_p}{\sum_{i=1}^{N} (\nu_i''' - \nu_i'') \cdot R_i^{(l)}} \qquad (105)$$

The freeze-in point within the nozzle can be found using this relation. Equation (105) applies not only for individual reactions, in which various materials can be considered, but also for several simultaneous reactions with consideration of the materials most important for the recombination process.

d) Application of the approximation method for various important reaction equations

The reaction kinetic processes in nozzle flow of a hot gas mixture are largely unknown, so that there is no certainty about the choice of the most important reaction equations. While 11 reactions in all were considered in determination of the kinetic equilibrium, (see p. 38), only the following reactions are considered for the approximate solution:

Reaction No. 2 $H + O_2 \rightleftharpoons OH + O$

Reaction No. 4 $H + H + M \rightleftharpoons H_2 + M$

Reaction No. 8 $H + OH + M \rightleftharpoons H_2O + M$

These reactions were chosen on the basis of the studies of Sarli et al. [17]. For the fuel system being considered, with the elements C - O - H - N, the water-forming reaction No. 8 appears to have decisive importance, because the results obtained using this reaction show good agreement with the exact solution. For this equation, therefore, the approximation method is applied to investigate the recombination of atomic hydrogen and the radical OH. The denominator in (105) takes on the form:

$$\sum_{i=1}^{N}(\nu_i'' - \nu_i')R_i^{(1)} = -K_1^{(8)}\rho^2 n_H n_{OH}\frac{1}{M} \qquad (106)$$

for this case.

In the simultaneous consideration of Equations 2, 4, and 8, /48 the recombination of hydrogen is considered the most important conversion. This yields the relation:

$$K_{B\,comp.}' = \frac{\left(\frac{\partial[Z_i]}{\partial t}\right)_p}{-\frac{\rho^2 n_H}{M}\left[K_1^{(2)}(n_{O_2})M + 2K_1^{(8)}\rho(n_H) + K_1^{(4)}\rho n_{OH}\right]} \qquad (107)$$

for the freeze-in condition.

For the numerical calculation, the fuel combination UDMH + HNO_3 was selected with the same combustion chamber conditions as for flow with relaxation. For given nozzle geometry the thermodynamic state values for chemical equilibrium were determined by the process described in Section B 2.

The parameters used along with the state values to characterize the equilibrium flow are plotted in Figure 15.

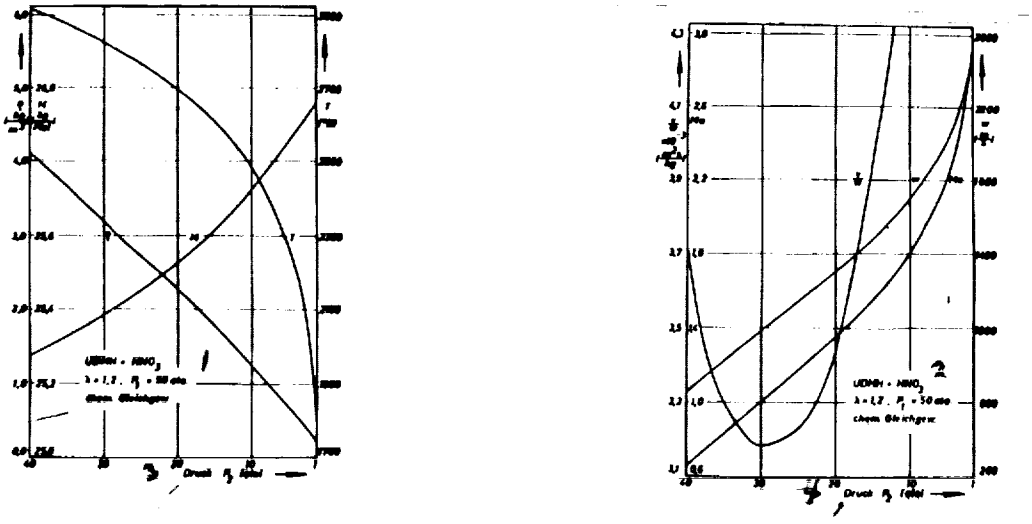

Figure 15. Thermodynamic and flow characteristic values in the equilibrium expansion.

1. chemical equilibrium
2. chemical equilibrium
3. pressure
4. pressure

Table 3. FREEZE-IN PRESSURE CONDITIONS FOR THE APPROXIMATE SOLUTION

/49

Component	Pressure ratio at the freeze-in point			
	H	OH	Composite H	Composite H
Reaction equation	8	8	2+4+8	4 + 8
$\lambda = 0,6$ $P_1 = 5$ ata				
$K_1^{\Delta U} = K_1 \cdot 10$	1,5	1,63	1,91	-
K_1	1,08	1,16	1,37	1,11
$K_1^{\Delta U} = K_1 \cdot 10^{-1}$	1,0	1,0	-	-
$\lambda = 0,6$ $P_1 = 50$ ata				
$K_1^{\Delta U} = K_1 \cdot 10$	2,96	4,85	3,18	-
K_1	1,86	2,25	1,94	1,93
$K_1^{\Delta U} = K_1 \cdot 10^{-1}$	1,23	1,33	1,32	-
$\lambda = 0,9$ $P_1 = 5$ ata				
$K_1^{\Delta U} = K_1 \cdot 10$	5,05	4,39	-	-
K_1	1,96	1,47	11,9	1,78
$K_1^{\Delta U} = K_1 \cdot 10^{-1}$	1,37	1,0	6,33	-
$\lambda = 0,9$ $P_1 = 50$ ata				
$K_1^{\Delta U} = K_1 \cdot 10$	31,9	10,0	15,6	10,2
K_1	7,94	5,1	12,8	6,5
$K_1^{\Delta U} = K_1 \cdot 10^{-1}$	3,31	1,92	9,8	3,36
$\lambda = 1,2$ $P_1 = 5$ ata				
$K_1^{\Delta U} = K_1 \cdot 10$	4,1	1,61	-	3,9
K_1	1,76	1,35	-	1,62
$K_1^{\Delta U} = K_1 \cdot 10^{-1}$	1,2	1,0	-	-
$\lambda = 1,2$ $P_1 = 50$ ata				
$K_1^{\Delta U} = K_1 \cdot 10$	18,5	6,18	-	17,8
K_1	8,48	2,87	-	6,33
$K_1^{\Delta U} = K_1 \cdot 10^{-1}$	2,52	-	-	2,26

The freeze-in point is determined by first calculating the /50
K_β value for various state points within the nozzle. The transition point can be found by graphic interpolation using the relation $K_\beta = 1$. Table 3 lists the freeze-in pressure ratios determined. These were based on various components, various reaction equations, and rate constants which deviate from the standard values.

At $\lambda = 0.6$ the component H freezes in first. With the other oxygen carrier ratios, OH shows a lower freeze-in pressure ratio. The approximation method, with simultaneous consideration of Reactions 4 and 8 leads to freeze-in pressure ratios between those for H and OH. Added consideration of Reaction 2 yields a steep shift of the freeze-in point with rising λ value in the direction of chemical equilibrium. With oxygen excess, finally, a solution for this case could no longer be found.

With determination of the freeze-in pressure all the values are known for description of the approximate course of expansion.

e) Comparison of the powers and the exhaust gas compositions for assumption of various expansion hypotheses

The specific impulse has been calculated for six differeent combustion chamber states, using the process treated in the preceding sections for determining the course of expansion of gas mixtures at high temperatures. The results are shown as functions of the expansion pressure ratio in Figures 16 to 18.

The power difference between the chemical and the frozen equilibrium is greatest at $\lambda = 0.9$. With a large excess of fuel ($\lambda = 0.6$) the difference drops, mainly because

of the lower combustion chamber temperature, to $\Delta I_{sp} = 5 \left(\frac{kps}{kg}\right)$ for $P_1/P_2 = 500$.

The difference between limiting values is reduced by increasing the combustion chamber at constant oxygen carrier ratio because the dissociation is reduced because of the higher pressure [58].

As the pressure rises, flow with relaxation approaches chemical equilibrium. Apparently the three-body collision reactions are decisive for the amount of energy recoverable /51
by recombination, because these reactions are very pressure-sensitive because of the third power of the concentration on the left side of the reaction equations. From the results of the kinetic calculation, the expansion flow is not near frozen-in equilibrium for the fuel combination studied, even with the assumed small nozzle dimensions except for $P_1 = 5$ atm, $\lambda = 0.6$. Therefore, the frequently used assumption of frozen equilibrium can lead to underestimation of the potential engine thrust.

At larger nozzle dimensions, the power level can shift even more strongly in the direction of chemical equilibrium because of the longer residence time of the gases in the nozzle, so that a prediction of the power actually expected is possible only in combination with the nozzle geometry.

The power comparison using the approximation method shows that the agreement with the kinetic solution is good with excess fuel, while greater deviations appear at $\bar{\lambda} = 1.2$. Apparently the recombination reaction selected, $H + OH + M = H_2O + M$ is no longer decisive for the total course of all the reactions because of the oxygen excess.

At this oxygen carrier ratio there appears a considerable difference between the freeze-in point for the components H and OH. It is particularly important at high combustion chamber pressure. Even use of the composite approximation provides no improvement here. But because a real engine is always operated with a large fuel excess, the approximation used allows more accurate determination of power in comparison with the limiting cases if the large computer cost for determining the kinetic nozzle flow is to be avoided.

In [7], considerations are established with respect to the reaction course of complex gas mixtures at high temperatures. They can serve to explain the good agreement of the approximation under consideration with the kinetic solution. As long as the radical OH, along with atomic hydrogen, is present at high concentration in the exhaust gas, the OH recombination proceeds through the bimolecular reactions 1 and 5. Simultaneously, more atomic hydrogen is formed. Conversion of the hydrogen occurs through the three-body collision reactions 4 and 8. Because the pure hydrogen recombination reaction 4 freezes in very rapidly, the total energy liberated from all the hydrogen reactions is finally dependent on the freeze-in point of reaction 8.

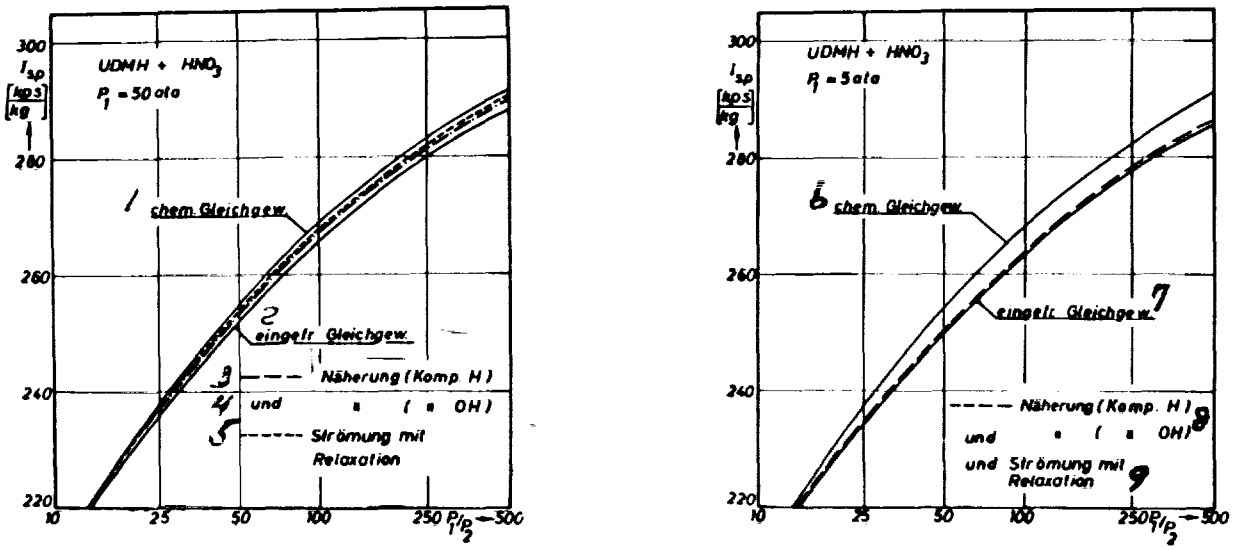

/52

Figure 16. Comparison of the specific impulse assuming different expansion hypotheses. Oxygen carrier ratio $\lambda = 0.6$.

1. chemical equilibrium
2. frozen equilibrium
3. - - - - approximation (comp. H)
4. and " " (" OH)
5. Flow with relaxation
6. chemical equililbrium
7. frozen equilibrium
8. - - - - approximation (comp. H)
   and " " (" OH)
9. and flow with relaxation

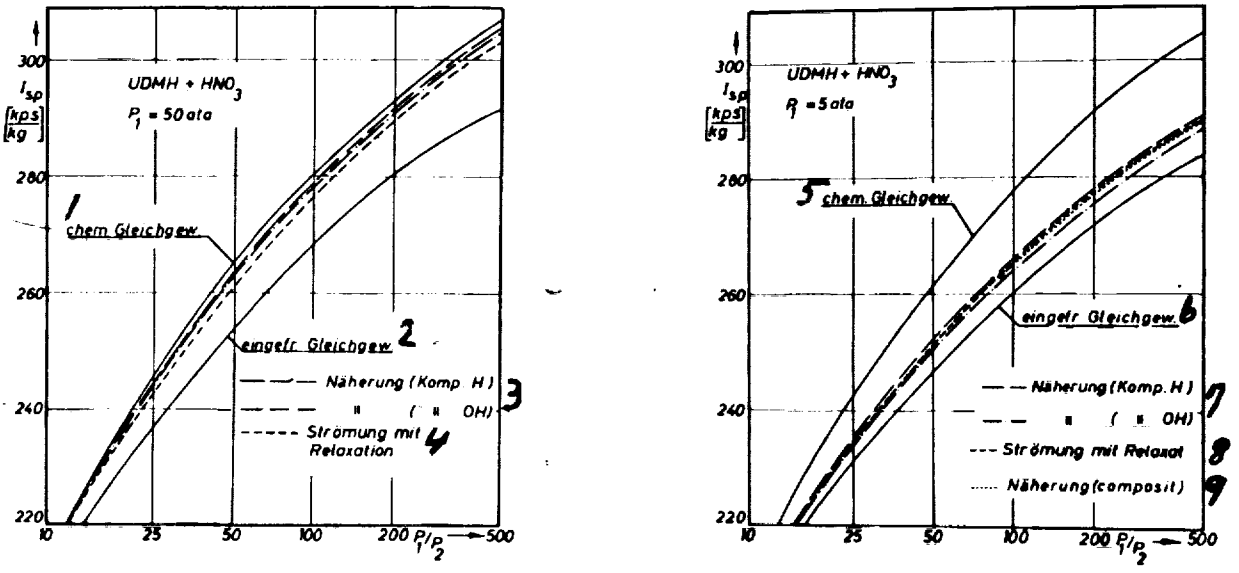

/53

Figure 17. Comparison of the specific impulse assuming different expansion hypotheses. Oxygen carrier ratio $\lambda = 0.9$.

1. chemical equilibrium
2. frozen equilibrium
3. - - - approximation (comp. H)
   - - - " (" OH)
4. flow with relaxation
5. chemical equilibrium
6. frozen equilibrium
7. - - - aproximation (comp. H)
   - - - " (" OH)
8. flow with relaxation
9. approximation (composite)

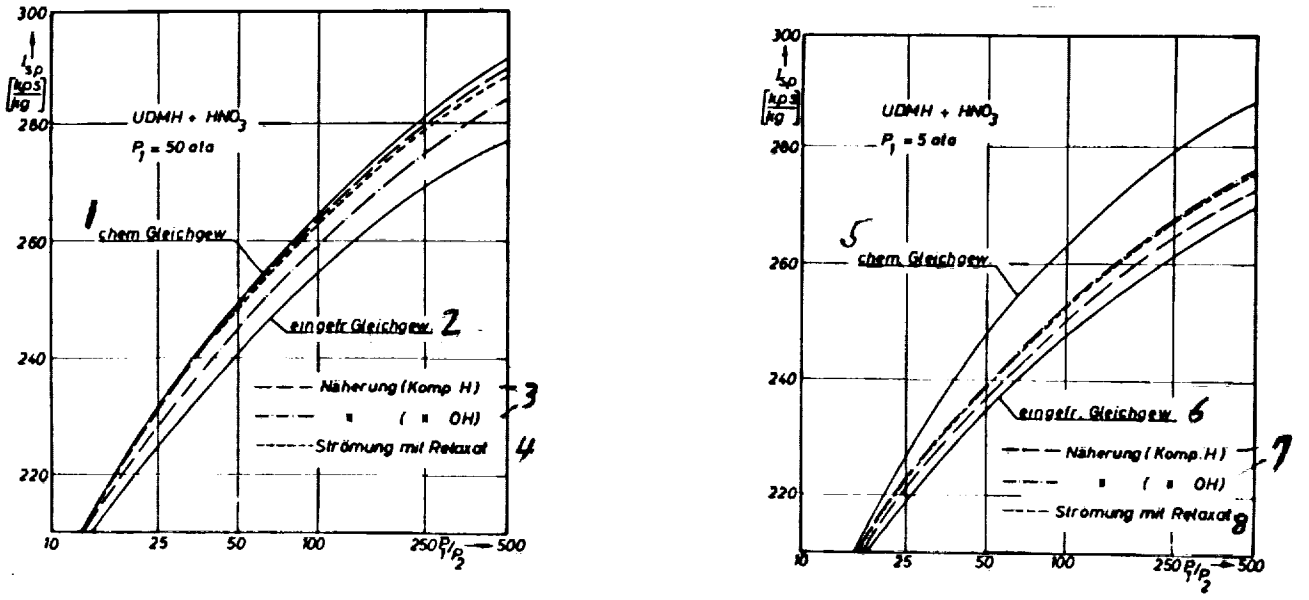

Figure 18. Comparison of the specific impulse assuming different expansion hypotheses. Oxygen carrier ratio λ = 1.2.

1. chemical equilibrium
2. frozen equilibrium
3. approximation (comp. H)
   " (comp. OH)
4. flow with relaxation
5. chemical equilibrium
6. frozen equilibrium
7. approximation (comp. H)
   " (comp. OH)
8. flow with relaxation

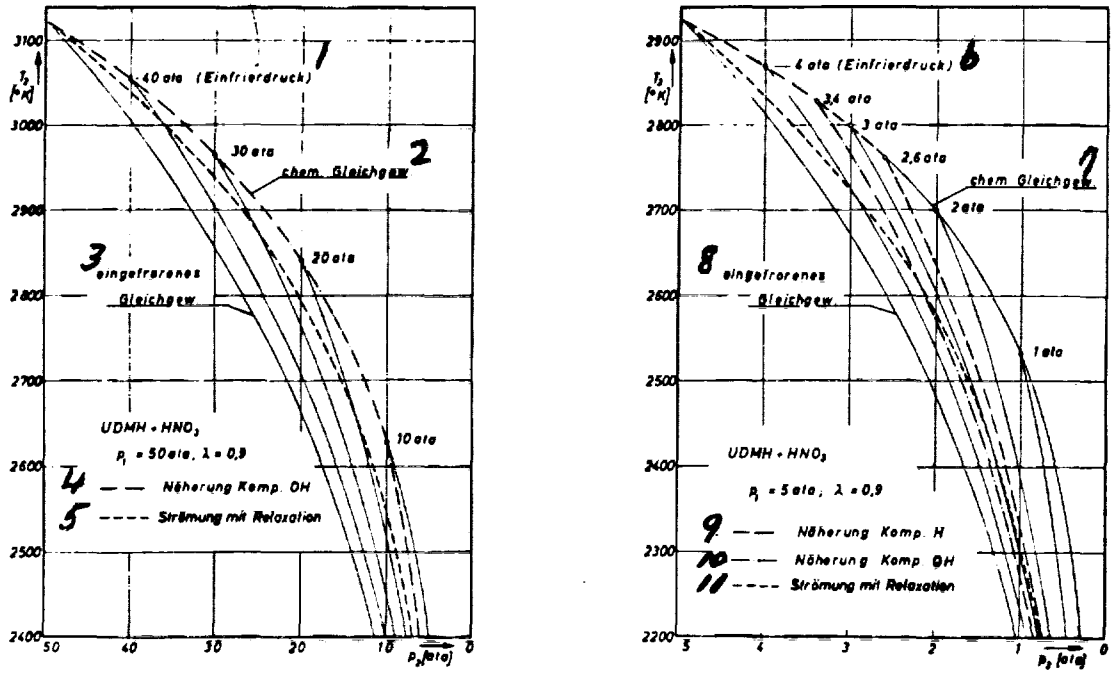

/55

Figure 19. Temperature curve in the initial part of the nozzle assuming different expansion hypotheses.

1. (freeze-in pressure)
2. chemical equilibrium
3. frozen equilibrium
4. approximation comp. H
5. flow with relaxation
6. (freeze-in pressure)
7. chemical equilibrium
8. frozen equilibrium
9. approximation comp. H
10. approximation comp. OH
11. flow with relaxation

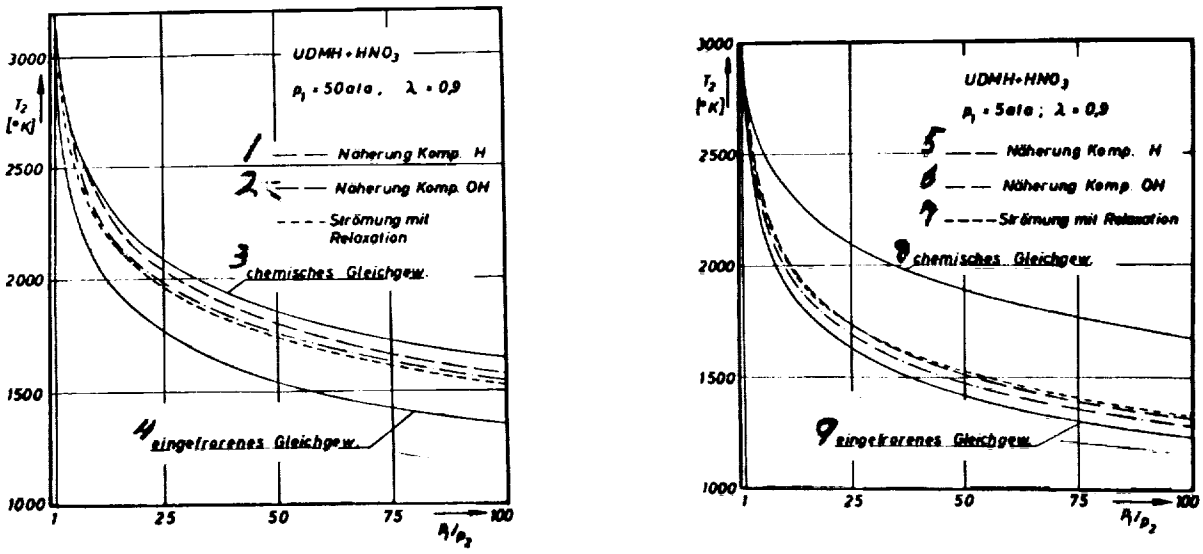

Figure 20. Temperature curve during discharge assuming different expansion hypotheses.

1. approximation comp. H
2. approximation comp. OH
3. flow with relaxation
4. frozen equilibrium
5. approximation comp. H
6. approximation comp. OH
7. flow with relaxation
8. chemical equilibrium
9. frozen equilibrium

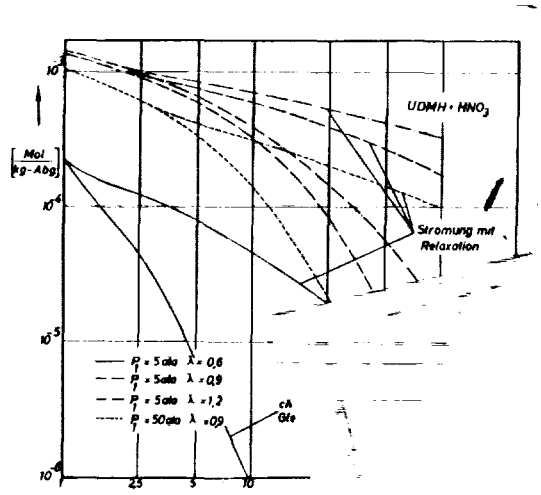

Figure 21. Molar number of the exhaust gas component OH during expansion with chemical equilibrium and for flow with relaxation.

1. flow with relaxation
2. chemical equilibrium

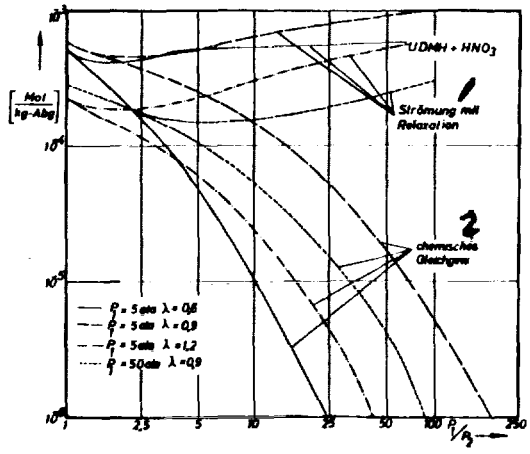

Figure 22. Molar number of the exhaust gas component H during expansion with chemical equilibrium and for flow with relaxation.

1. flow with relaxation
2. chemical equilibrium

The comparative consideration of the temperature curve in the first part of the nozzle expansion shows the difference between the kinetic solution and the approximate solutions. The final expansion temperature for the approximation differs more and more strongly from the exact kinetic computation at low pressure ratios. Then at the freeze-in point the temperature curve bends downward and again approaches the kinetic solution on further expansion. This relation also very clearly clarifies the principle of the approximation method. /58

For large pressure ratios, the calculated expansion temperatures show a curve corresponding to that of the specific impulse. This can be seen from comparison of Figures 17 and 20. Because of the good agreement of temperature and specific impulse, temperature measurement can be considered as an experimental method which is well suited to investigate recombination phenomena.

The equations which have been set up so far refer to the total system. For detailed investigations, though, changes in the molar numbers are of interest, among other things. Here a considerable difference appears between the different hypotheses. Out of the eleven exhaust gas components, the molar numbers for H and OH are plotted as examples in Figures 21 and 22 for chemical equilibrium and for flow with relaxation at various combustion chamber states. The higher the combustion temperature and the combustion chamber pressure are, the later the deviation appears between the two expansion hypotheses. With the further expansion, for flow with relaxation, the measure of the approximation to the horizontal curve is a criterion for attainment of the frozen-in state.

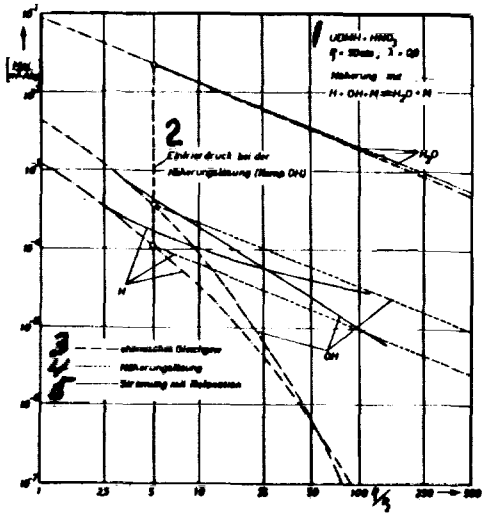

Figure 23. Comparison of the concentrations of the exhaust gas components during discharge assuming different expansion hypotheses.

1. approximation with
2. freeze-in pressure for the approximation equation (comp. OH)
3. chemical equilibrium
4. approximation
5. flow with relaxation

The curves for the concentrations of important materials, /59
according to Figure 23, show great deviations for the components present at low concentrations, while the difference for H_2O can be considered slight.

f. Calculation of the impulse figure and effect of the reaction rates on the engine power

Barrere used a parameter ξ to characterize the real course of expansion. The parameter indicates the deviation of the specific impulse from the limiting cases of chemical and frozen equilibrium [10].

This characteristic value, which is designated in the following as the impulse figure i, is well suited for analysis of Bray's approximation method because the position of the freeze-in point strongly affects the magnitude of the impulse figure

$$i = \frac{I_{sp\ approx.} - I_{sp\ fr.}}{I_{sp\ chem.} - I_{sp\ fr.}} \qquad (108)$$

Here the impulse $I_{sp\ approx.}$ corresponds to the total power with the assumptions of the approximation procedure, and is determined as follows from the limiting cases on selection of a certain freeze-in point: The exhaust velocity w is made up of two parts, which correspond to the enthalpy differences in chemical and frozen equilibrium.

$$w = \sqrt{2[(h_1 - h_x)_{chem.} + (h_x - h_2)_{frozen}]} \qquad (109)$$

h_x = enthalpy at the freeze-in point

$h_{x\ chem.} = h_{x\ frozen.}$

With knowledge of the freeze-in point the specific impulse can be determined from (109). At the Aachen Computer Center the beginning of frozen-in flow within the nozzle was varied for the nozzle expansions investigated, so that the enthalpy, $h_{beim.}$ is available for many freeze-in points. /60

The results of such a calculation for two expansion cases is plotted in Figure 24. With decreasing freeze-in pressure the impulse figure rises almost linearly. If the i value is plotted as a function of the area ratio as in Figure 25, one can sse that in the region of the narrowest cross section there is a steep rise in the curves for various combustion chamber pressures and mixture ratios. As the temperature dependence of the reaction rate is large and the temperatures drop considerably near the nozzle throat, the impulse figure changes sharply in the vicinity of the narrowest cross section. The effect of the combustion chamber pressure is slight while the mixture ratio produces a large shift in the impulse figure. That is due to the very different combustion temperatures for different values of λ .

If one considers the approximation methods according to Bray, from the viewpoint of Figure 25, the flow must frequently freeze in in the vicinity of the critical cross section. If the freeze-in point varies from the high subsonic region to the low supersonic region, this can cause a shift of the power from the nearly frozen-in flow to near chemical equilibrium flow. Because of this high sensitivity of the impulse figure in the vicinity of the nozzle throat, the predictive force of the approximate solution must be limited if the freeze-in point is in the vicinity of F_{min}.

In order to estimate the effects of the rate constants on the freeze-in point, the standard value of K, was varied over an order of magnitude upward and downward for all six combustion chamber states under consideration. The result in Table 3 shows that for large reaction rates the transition point is shifted in the direction of the nozzle

end, while reduction of the rate constants has the opposite effect. The extent of this shift is affected by the combustion chamber pressure and the oxygen carrier ratio. The effect is greatest for the energetic mixture (P_1 = 50 atm, λ = 0.9). If the approximation is to be used for highly energetic fuel combinations such as $H_2 + F_2$ (Figure 13b), the effect of the rate constants on the result is apparently very great, so that more accurate /62 investigations must be established about applicability in this case, because the kinetic data are still relatively inaccurate.

/61

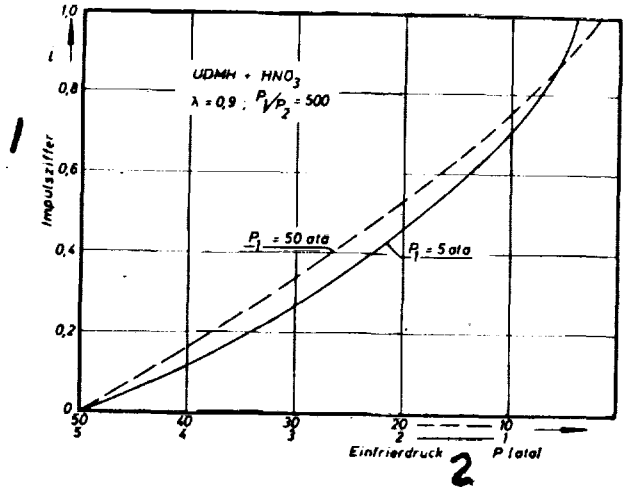

Figure 24. Impulse figure i for change of the freeze-in pressure

1. impulse figure
2. freeze-in pressure

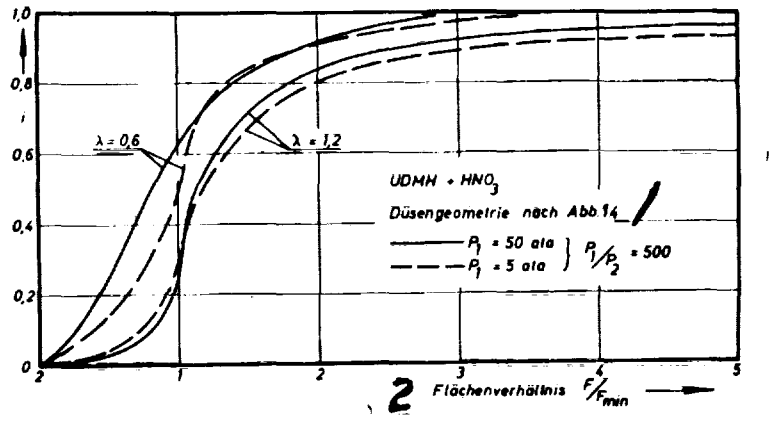

Figure 25. Impulse figure i as a function of the cross section ratio of the expansion nozzle

1. nozzle geometry according to Figure 14
2. area ratio

In order to determine the sensitivity of the impulse figure to changes in the rate constants for the system UDMH + HNO_3 the composite approximation is used. A partial shift of the reaction rates of the reactions considered is undertaken.

Figure 26 shows, for instance, the dashed curves under the condition that the reaction rate for the reaction H + OH = H_2O is changed by the factor C shown on the abscissa, while the reaction rate for the other reaction involved, H + H + M = H_2 + M, retains its standard value.

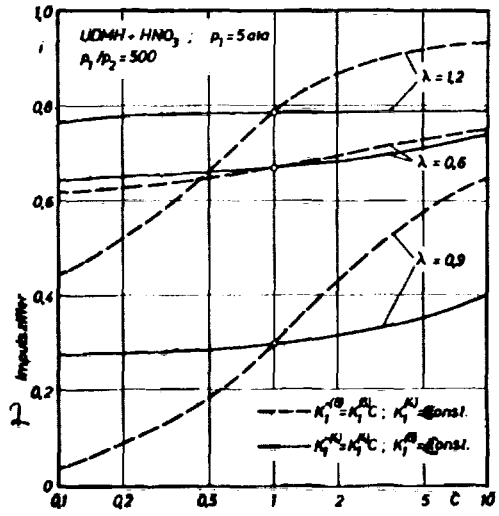

(1)

Figure 26. Influence of changes in the reaction rates on the power. Approximation method considering the reactions:

$$H + H + M \xrightarrow{K_1^{(A)}} H_2 + M$$

$$H + OH + M \xrightarrow{K_1^{(B)}} H_2O + M$$

1. Factor of change in reaction rates
2. impulse factor

The result shown in Figure 26 shows that the 3-body hydrogen formation reaction dominates at all mixture ratios. That is, the system UDMH + HNO_3 is most sensitive for this reaction. /63

The effect of the hydrogen recombination reaction decreases, though, with increasing excess of hydrogen in the total mixture.

For instance, while at $\lambda = 1.2$ the hydrogen recombination causes practically no change in power, its effect is noticeable at $\lambda = 0.9$, and at $\lambda = 0.6$ its effect is almost as great as that of the water formation reaction.

4. Calculation of the vibration frequency with unstable combustion

Occurrence of unstable combustion processes often delays the development of high-temperature engines. Several causes, often acting simultaneously, are responsible for initiating this phenomenon. Instabilities produce pressure vibrations superimposed on the combustion chamber pressure. Depending on the amplitude of the superimposed vibration they may present a danger to satisfactory operation of the rocket.

These phenomena are influenced by design and operating values such as the supply system, valves, dynamic effect of the fuel flow through the injection head, injection pressure drops, combustion chamber and nozzle shape, position of the injection orifice, fuel, ignition delay, combustion chamber pressure and oxygen carrier ratio [10, 38, 59].

The instabilities can essentially be divided into two basic types:

a. the intense low tones corresponding to the low-frequency instability with a frequency range of about 10 to 200 Hz.
b. the higher whistling tones, assigned to the so-called high-frequency instability, with a frequency of about 1,000 to 10,000 Hz.

Instability effects were also observed occasionally in our own test stand investigations. Thus, it seems appropriate within this theme to analyze these phenomena separately, comparing the results found experimentally with theoretical principles.

Most calculations of low-frequency instabilities are based on the assumption of hydraulic coupling between the combustion chamber pressure and the fuel supply system [38, 39]. /64

For our experimental combustion chamber, the fuel flow rates in the lines are low because of the low mass throughput, so acceleration effects are not considered [39].

The pressure fluctuation, which appear in the form of damped vibrations, can be represented by the following relation:

$$f(t) = e^{nt} \sin \omega t \qquad (110)$$

The amplitude factor n may take only low values because of the danger of immediate destruction of the engine, so that (110) gives the approximation:

$$f(t) = \sin \omega t + nt \cdot \sin \omega t \qquad (111)$$

The mass of fuel M_v burned at time t corresponds to the mass portion M_e injected at a previous time $(t - \theta)$.

$$M_v(t) = M_e(t - \theta) \qquad (112)$$

The mass flow through the combustion chamber, M_s, is made up of a constant amount M_o and a non-steady portion dependent on the time.

$$M_s = M_o + f(t) \tag{113}$$

For the combustion gas present in the combustion chamber, M_K and the portion M_D flowing out through the nozzle, the gas equation applies, corresponding to the state after combustion.

$$M_K = k_1 \cdot P_1 = \frac{V_K \cdot P_1 \cdot M_1}{R \cdot T_1} \tag{114}$$

$$M_D = k_2 \cdot P_1 \tag{115}$$

It follows that the mass balance in the combustion chamber is:

$$\frac{dM_K}{dt} = M_V - M_D \quad \text{or} \quad M_V = k_2 \cdot P_1 + k_1 \frac{dP_1}{dt} \tag{116}$$

The processes in the combustion chamber are influenced by the pressure drop from the supply tank up to the chamber. This pressure drop is made up of the pressure difference in the injection head, $\Delta P\text{-head} = M_s^2/K_3^2$, the frictional losses in the line, $\Delta P_L = K_4 \cdot w^2 = K_4 \cdot M_s^2/(\rho \cdot F)^2$ and the constant pressure loss in a spring-loaded check valve, ΔP_R. /65

$$P_{Tank} - P_1 = \left(\frac{M_s}{k_3}\right)^2 + k_4 w^2 + \Delta P_R \tag{117}$$

It follows from Equation (113) that:

$$(M_s)^2 = (M_o)^2 + 2 M_o f(t) + [f(t)]^2 \tag{118}$$

The quadratic term $[f(t)]^2$ can be neglected as an approximation because the amplitude variations of the

combustion chamber pressure and of the mass flow are small in comparison with the absolute average values.

On introduction of (118) into (117), and noting that $M_s = \rho \cdot F \cdot w_s$, it follows that

$$P_t - P_1 = \frac{(M_s)^2}{k_3^2} + 2 \cdot \frac{M_s \cdot f(t)}{k_3^2} + \frac{k_4}{(\rho \cdot F)^2}(M_s)^2 + \frac{k_4}{(\rho \cdot F)^2} 2 M_s \cdot f(t) + \Delta P_R \qquad (119)$$

If one introduces P_t from this equation, or the differential quotient dP_t/dt in (116), and notes that $M_v = M_o + f(t - \theta)$, then:

$$\left[\frac{k_1 \cdot 2 \cdot M_o}{k_3} + \frac{k_1 \cdot k_4}{(\rho \cdot F)^2} \cdot 2 \cdot M_o\right] \frac{df(t)}{dt} + \left[\frac{k_2 \cdot 2 \cdot M_o}{k_3^2} + \frac{k_2 \cdot k_4}{(\rho \cdot F)^2} \cdot 2 \cdot M_o\right] f(t) +$$

$$+ f(t - \theta) = k_2 \cdot P_1 - \frac{k_2 \cdot (M_s)^2}{k_3^2} - \frac{k_2 \cdot k_4}{(\rho \cdot F)^2} \cdot (M_s)^2 - k_2 \Delta P_R - M_o \qquad (120)$$

In the steady state case, $M_v = M_o = M_s$, so that with (115) and (117) the right side of (120) becomes equal to zero.

If one also introduces the designations A and B for those in the square brackets in [120], then (120) can be transformed into:

$$A \cdot \frac{df(t)}{dt} + B \cdot f(t) + f(t - \theta) = 0 \qquad (121)$$

/66

The quantities A and B can be obtained from thermodynamic rules, especially from the relations according to Section B 1 c.

$$A = \frac{4{,}76 \cdot E^* \cdot Z \cdot (P_{ank} - P_1 - \Delta P_R)}{C^* \cdot P_1} \qquad (122)$$

$$B = \frac{2}{P_1} (P_{ank} - P_1 - \Delta P_R) \qquad (123)$$

By combining (121) and (111) and ordering according to the same coefficients of t there follows, among others, this expression as a condition for the vibration frequency ω:

$$\frac{4{,}76 \cdot L^2 Z \cdot (R_{max} - R - \Delta R_k)}{C^4 \cdot R} \omega - \sin\omega\theta = 0 \qquad (124)$$

C. EXPERIMENTAL INVESTIGATIONS ON IGNITION, COMBUSTION AND THE SUBSEQUENT EXPANSION /67

1. Apparatus for determining the ignition delays of hypergolic fuels

a) Structure of the test stand

The use of self-igniting fuel combinations is of special interestfor engine development because the cost of building a special ignitor can be saved, and because failure of ignition must be avoided in all cases due to the danger of destroying the engine. There was, therefore, very early concern with the ignition characteristics of chemical fuel pairs [40, 41]. There are essentially two different types of device that are used for this purpose: the drop test and the two-stream method [42, 43]. In the former, one allows a certain amount of oxidizer to drop into a vessel with the fuel, and measures the ignition delay. In the two-stream devices, on the other hand, both components are freely sprayed together through two capillary tubes. Their design more nearly approaches the actual relations in a combustion chamber and also provides a faster sequence of tests with lower fuel consumption. Furthermore, certain operating parameters such as temperature, pressure, effect of the free jet length and capillary diameter can also be investigated with the two-stream apparatus [44].

In order to be able to measure ignition delay times of fuels tested on the combustion chamber test stand, including the effects of admixtures of aluminum, with a system of similar dimensions, the test stand shown schematically in Figure 27 was developed.

The main part of the apparatus is the combustion chamber (1) of acid-resistant steel, with the two injection valves for fuel (2) and oxidizer (3) standing at a relative angle of 90°. Both components are in the aluminum supply containers (5, 6). They can flow out of bottom of the containers after opening of both valves (7 and 8) and into the volume meters (9, 10). Commercial volume flowmeters were used for the volume measurement. The floating balls were removed from the meters, and their scales were specially calibrated for this application.

The pressure required for injection of both components is taken from a nitrogen bottle (15), and separately adjustable through pressure reduction valves (16, 17) and needle valves (20, 21). To ease the filling process, the pressures in the supply containers are controlled by needle valves (18, 19), and the pressures are indicated by the sensitive manometers (22 to 25).

Special attention was devoted to development of the injection valve (Figure 28). The housing is of nonmagnetizable steel (material No. 4541). Inside the housing, the magnetic iron core (No. 4501) moves along the guide paths with longitudinal slots. When the magnet is switched on, the core moves upward against the force of the return spring and opens the flow to the injection capillary. The valve seat and needle are designed as flat cones of different slope. The needle tip is of Teflon. The easily changeable injection capillary is dealed by O-rings.

/68

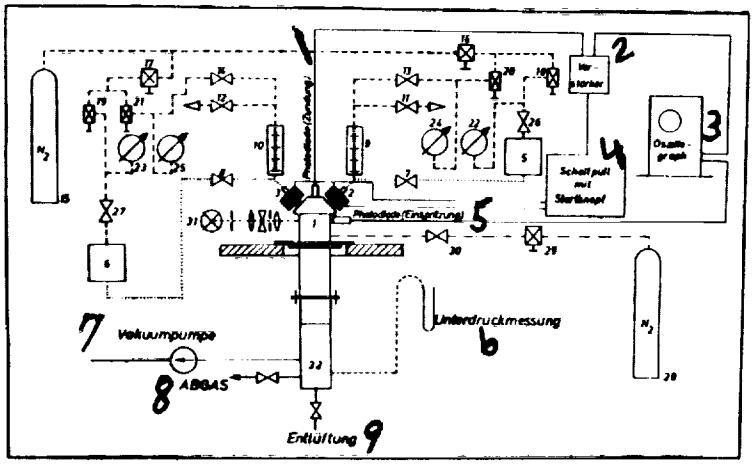

Figure 27. Schematic design of the ignition delay test stand

1. photodiode (ignition)
2. amplifier
3. oscilloscope
4. switchboard with starting button
5. photodiode (injection)
6. reduced pressure measurement
7. vacuum pump
8. exhaust gas
9. ventilation

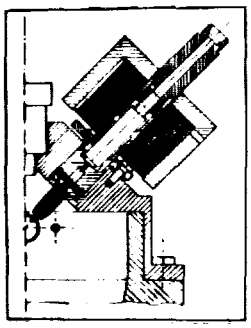

Figure 28. Injection valve

In order to prevent carbon deposition on the parts projecting into the combustion space, a nitrogen flush is provided by an annulus between the nozzle jacket and the capillary tip. /69

b. Measurement and control systems

The ignition delay is defined at the time between the first contact of the two fuel components and the appearance of a visible flame.

As the times are measured in milliseconds, all mechanical measuring devices are ruled out. Optical-electronic components were used with this test stand to determine injection and ignition times with the highest possible accuracy. By means of an optical bench with a system of lenses and diaphragms, a sharply focused beam of parallel light is produced at the point of contact of the two fuel streams within the combustion chamber. Behind the chamber, the beam strikes a photodiode. The voltage generated there

is amplified and plotted on the oscilloscope screen. In the injection process the light beam is covered by the fuel stream which runs across it, so that the intensity of the light leaving the system is attenuated.

Due to the partially different blocking of the light by one component, compared to the other, on injection, the processes within the combustion chamber can be maintained exactly, so that measurement errors due to different injection times are eliminated (Figure 30). This arrangement also automatically provides the possibility of measuring the lead of one component over the other and its effect on the ignition delay.

The time of ignition is determined by a second photodiode arranged to view the entire combustion volume in the head of the chamber.

This photodiode simultaneously actuates a relay through a transistor amplifier. The relay cuts off the magnetic valve and interrupts the fuel supply (Figure 29) [45].

This prevents accumulation of a large amount of exhaust gas in the combustion chamber, and makes it easier to do tests at reduced pressure.

The outputs of both photodiodes are displayed on a two-channel oscilloscope and recorded photographically. The calibrated time base of the device allows simple evaluation of the test results (see Figure 30).

A delay circuit is installed to allow selectable change of the injection time [43]. A continuously adjustable potentiometer can delay one component by up to 200 ms after the other.

/70

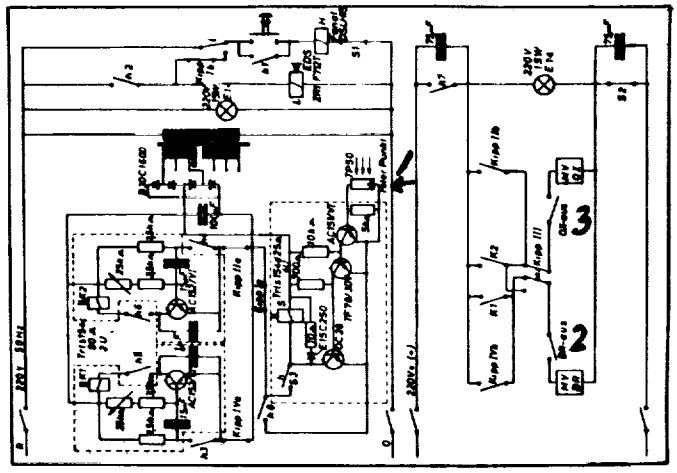

Figure 29. Circuit diagram of the electrical system of the ignition delay test stand

Kipp: = switch

1. red spot
2. fuel out
3. oxidizer out

a) Fuel leads b) Oxidizer leads

Figure 30. Ignition delay measurement (d = lead)

In order to assure early fuel cutoff in case of ignition

failure, there is also a time relay with adjustable switching delay of 0.1 to 1.0 seconds.

In normal operation the combustion chamber is open. For /71 investigations in the low-pressure range the chamber and another container connected to increase the volume are evacuated by a vacuum pump (Leybold D 2). The flange connection between the chamber (1) and the supplemental container (32) is designed as an overpressure safety. In vacuum operation reduced pressure can also be applied to the fuel so that the injection pressure drop can be varied over a wide range.

2. Investigation of the time delays of hypergolic fuels

a. Fundamental considerations on the self-ignition process with different fuels

F. A. F. Schmidt at the Institute for Motor Working Methods of the GRS [German Rocket Society] has already been intensively concerned with the theoretical and experimental investigation of auto-ignition processes, and has reported fundamental relations [46]. These works have been successfully extended at the Aachen Technical College and have recently been extended to higher temperature ranges [1, 6, 47]. In particular, F. A. F. Schmidt developed the semiempirical relation

$$\tau = \alpha \cdot \beta \cdot p^{n} \cdot e^{\frac{b}{T}} \cdot \sqrt{T} \qquad (125)$$

which describes the ignition behavior of technological fuels on oxidation with air.

The constants b, n, and a in Formula (125) do not represent concepts which can be accurately defined physically.

Rather, they should be considered as means of empirical values [46].

The factor ß considers the shortening of the ignition delay period due to the increase in reaction rate due to the temperature rise in this period. This theoretical consideration of the laws of the autoignition process has proved very useful for combustion in engines, e. g., for explanation of the knock process in Otto engines.

For testing the ignition behavior of hypergolic fuels, we do /72 not deal with a homogeneous gas mixture. Rather, the nature of the preparation and mixing are involved with the magnitude of the delay time. That is, as in the determination of the autoignition temperature, the experimental conditions exert a great effect on the results. The fuel combination itself determines the reaction enthalpy, reaction rate, heats of fusion and vaporization, specific heats of the solid, liquid and gaseous components and reaction products, as well as the surface tension and viscosity. The variable operating conditions include the oxygen carrier ratio, degree of mixing, initial temperature of the components, and the pressure and temperature in the experimental chamber [43]. Equipment which can most nearly approach real conditions is considered advantageous for measurements.

Hypergolic fuels have a high chemical reactivity in the liquid phase. The activity of the reaction partners is a function of the temperature and of the amounts of the components in the injection stream. As soon as both components have made contact, the exothermic reaction begins at the ambient temperature. Because of the exponential dependence of the reaction rate on the temperature, according to the Arrhenius law, the

temperature in the primary reaction zone rises rapidly until the concentrations of the reaction partners decreases according to the limiting diffusion rate. Morrell [48] has represented the change of the concentration by:

$$-\frac{d[Z]}{dt} = k_5 \cdot Z^n e^{-b/T} \qquad (126)$$

k_5 = constant

Assuming continuous injection of the components, the concentration is inversely proportional to the container volume, so that this equation follows for a second-order reaction from (126):

$$\tau = k_6 V_k e^{b/T} \qquad (127)$$

k_6 = constant

By means of this relation, a satisfactory agreement with some experimental results can be found for a limited temperature range [48]; but the relation by F. A. F. Schmidt also appears more suited for application to hypergolic liquid fuels because the pressure dependence of the ignition delay is explicitly expressed in the formula.

b. Experimental results and discussion of the ignition delay measurements /73

I. Variation of the operating conditions

The generally observed rise in the ignition delay time of reactive mixtures with diminishing external pressure, which is also presented in Equation (125), has also been found in the ignition behavior of the hypergolic liquid fuels used.

The amount of change in the hypergolicity is dependent on the injection system and the reaction volumes. At greater underpressure the components begin to vaporize immediately after injection. The reduction in the concentration of the reaction partners which this causes leads to a decrease in the reaction rate [46]. If the chamber volume is large in comparison to the amount of fuel injected, the ignition is delayed until the combustion space contains so much vapor that the fuel can only partially evaporate and a reaction in the liquid phase at high concentration can occur.
Apparently Morrell [48] took this phenomenon into consideration by introducing the reaction volume into the numerator of the ignition delay equation. /74

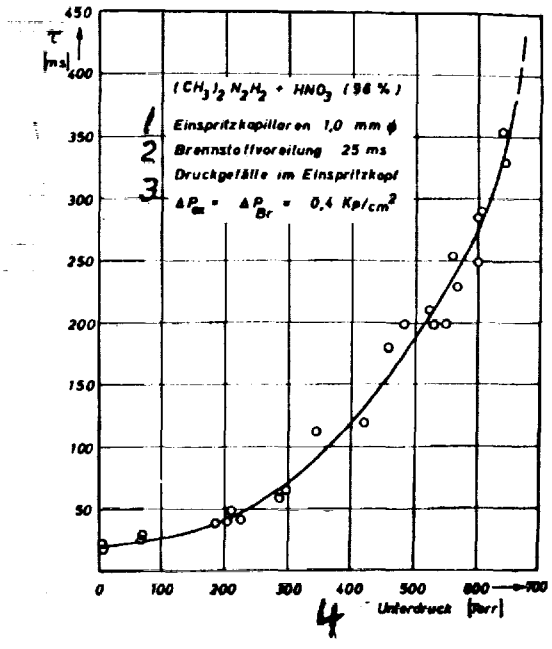

Figure 31. Ignition behavior of a liquid fuel combination at reduced external pressure

1. injection capillaries 1.0 mm diam.
2. fuel lead 25 ms
3. pressue drops in the injection head
4. reduced pressure (Torr)

C-2

At an underpressure of 700 Torr no ignition can any longer be achieved in the experimental apparatus used (see Figure 31). It should be noted, though, that the fuel supply was automatically interrupted after an injection time of 0.5 sec in order to prevent the possible eventual ignition of an excessive amount of fuel.

The investigation of the effects of the lead of one component compared with the other, which is possible with the measuring method used, showed that the ignition delay times become smaller, with this experimental system and with the fuel combinations tested, if the oxidizer is injected 30 to 100 msec earlier than the fuel (see Figure 32). This result is explained by the different preparation times of the two fuel components. This shows the necessity, for application, of considering this parameter to achieve good ignition properties.

II. Change of the acid concentration

As the production costs of the fuel combinations rise steeply with higher degrees of purity, the effect of the acid concentration on the ignition delay was tested.

Beginning with a 99% acid, the concentration was reduced by 3% steps down to a limiting value of 90% by adding distilled water. The investigation of a higher water content appeared unnecessary because water as a ballast reduces the combustion temperature and, therefore, reduces the power. No difference in ignition behavior was observed between the 99% and the 96% acids. At 93% a slight increase in the τ value was observed. The results of the lowest concentration are shown in Figure 33 in comparison with the 96% acid The 6% lower concentration increased the delay time by an average of about 10 msec. The experiments have

shown that at a concentration of more than 90% HNO_3 (remainder H_2O) for the acid used, there are no narrow limits established with respect to the ignition behavior. When the oxidizer leads by 50 ms the ignition delay values are still below 30 msec for the 90% acid.

/75

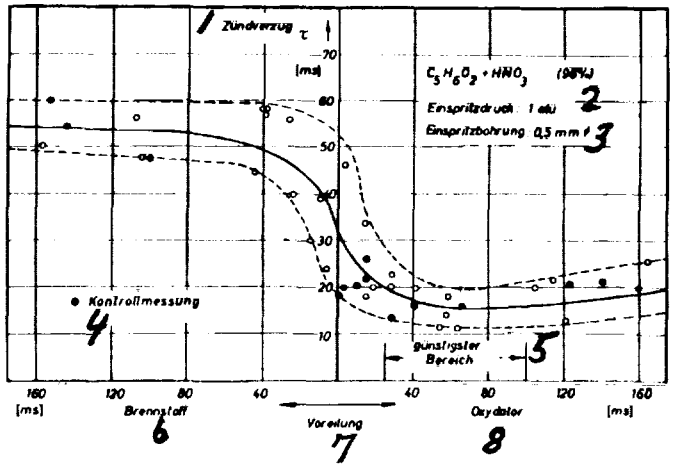

Figure 32. Dependence of the ignition delay time on the lead of one fuel component. (The range between the dashed curves corresponds to the range of variation of the measurement.)

1. ignition delay
2. injection pressure: 1 atm gauge
3. injection bore: 0.5 mm diam.
4. control measurement
5. favorable range
6. fuel
7. lead
8. oxidizer

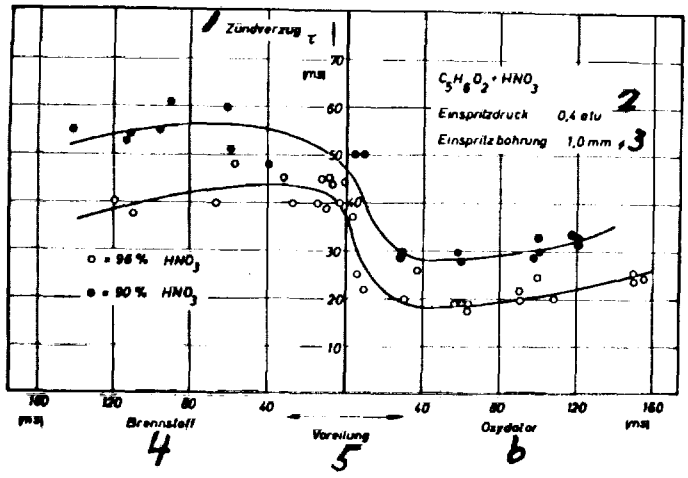

Figure 33. Effect of acid concentration and lead on the ignition delay time.

1. ignition delay
2. injection pressure 0.4 atm gauge
3. injection bore 1.0 mm diam.
4. fuel
5. lead
6. oxidizer

According to [43] it does make a difference which component /76
contains the water. Because of the heat of hydration, the hypergolicity can quickly be lost under some circumstances.

III. Admixture of aluminum

The measured change in ignitability due to addition of aluminum to the fuel is shown in Figure 34. Hardly any increase in ignition delay time could be detected up to 10% added metal. At higher metal concentrations, though, the delay time rose steeply, and the ignition limit was reached at 20%. In these experiments also, the ignition delay times were 10 to 15 ms higher when the fuel was leading.

Apparently the reactivity was severely limited by extensive accumulation of the aluminum particles on the fuel droplets.

The dependence of the ignition delay time on the particle size of the metal was not investigated; but L. E. Dean has found that no effect on the τ value was present for aluminum particle sizes between 5 and 44 μ [49]. The aluminum powder used had a mean particle size of less than 40 μ for the primary particles.

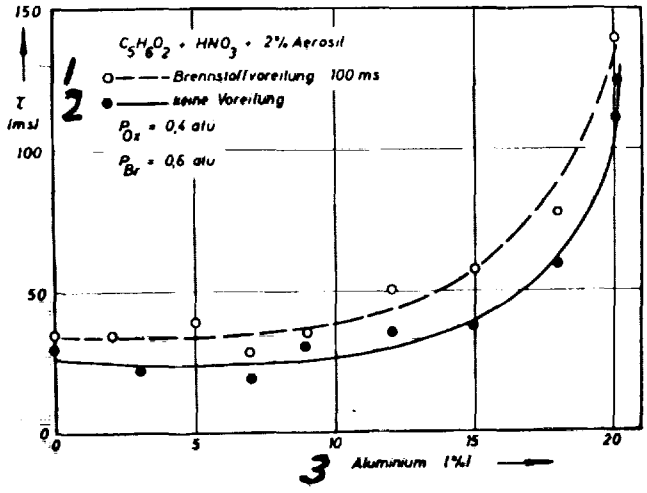

Figure 34. Change of the ignition delay time due to addition of aluminum

1. fuel lead 100 ms
2. no lead
3. aluminum

Along with the influences considered, the diameter of the /77 injection capillary, the injection angle, the injection pressure drops, the temperature and the mixture ratio are important for the magnitude of the delay time [44, 48] so that discovery of a generally applicable rule for calculation of delay times of hypergolic liquid fuels is extremely difficult.

From the experiments done, though, the ignition behavior of the fuel combinations used could be analyzed to the extent that the production of favorable ignition conditions at the combustion chamber test stand was assured. In particular, the possibility of shortening the delay time by leading with the oxidizer and the beginning of the injection process was utilized.

Further, due to the measured effect of acid concentration in the combustion chamber experiments, only 96% nitric acid was used as the oxidizer.

3. Combustion chamber test stand with thrust nozzle

a. Test stand design

A test stand according to Figure 35 was developed and built for the desired investigations. As the investigations were done with liquid fuel combinations, supply of the fuels by means of compressed gas appeared most suitable. Nitrogen is taken from a supply bottle through a pressure reducing valve and manometer to the separate supply containers for fuel and oxidizer. In this way the desired injection pressure and, as a result, the mixing ratio, can be adjusted simply. From the supply containers the two components pass through mass flowmeters to the combustion chamber injection head. In order to be able to switch to a different fuel during operation, a second fuel container was installed. It can be turned on or off by a three-way valve. In order to keep the injection head clean of combustion residues, a nitrogen flush had to be installed in the injection head. It works at a over-pressure of 2.5 atm. The fuel and flush lines are provided with check valves to prevent back-flow of the

components. The combustion chamber table can be displaced horizontally by an electric motor in order to be able to perform measurements at various points in the combustion chamber or behind the thrust nozzle. The entire system is controlled automatically not only to rule out erroneous conditions but also to reduce the /78
necessary preparation time for a test, because the test itself often runs only for a few seconds. The system was designed so that both fuel combinations can be injected with different relative delays. Two long-time-delay and two short-time-delay relays were installed for starting and cutoff magnetic valve control. They were coupled through a programmed switch so that there can be four different starting and cut-off programs: 1. start with flush gas and relative delay of fuel components

2. start without flush gas with relative delay of fuel components
3. start without flush gas, fuel components simultaneous
4. start with flush gas, fuel components simultaneous.

The various processes go in reverse order on cut-off. The long-time-delay relays control the pre-run or post-run of nitrogen. The short-time-delay relays control the response interval for the fuel valves on startup and cut-off. After preparing the system, the delay times of the components of the entire system were measured with an electronic counter. It appeared that they were nearly independent of the pressure that was set, and that the effective delay times of about 0.03 seconds were shorter than the times set.

Figure 36 shows a general view of the test stand. The supply lines were laid under the floor. Between the operating and measuring test stand on one side and the combustion chamber table on the other size, a movable armored wall was installed. It provides adequate protection in case of starting failure, etc. As highly concentrated

nitric acid and unsymmetrical dimethylhydrazine were used among the fuels, all the parts coming in contact with these materials had to be made of 4401 or 4541 stainless steel or, in some cases, of aluminum. The combustion gases were removed through a cooled exhaust gas channel by means of a suction train.

The automatic switching of the course of the test simplified the operation of the apparatus and required only a little concentration. Another advantage of the relay circuit is the speed and accuracy of the switching process, which is not attainable manually. For special purposes, the automatic system can be manually over-ridden.

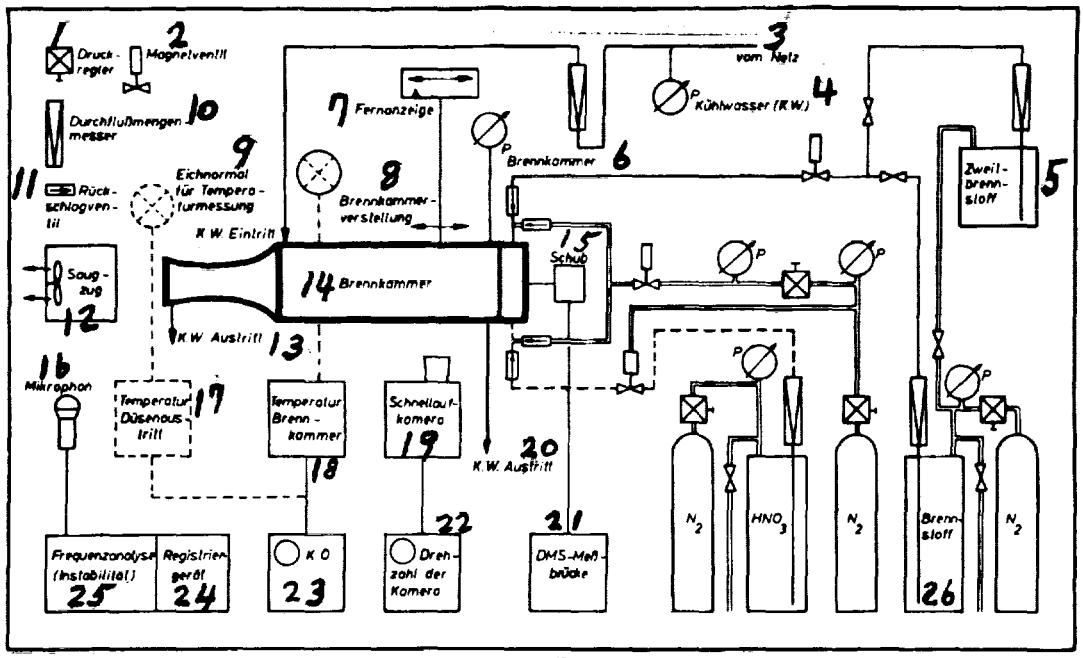

/79

Figure 35. Schematic structure of the combustion chamber test stand.

1. pressure regulator
2. solenoid valve
3. from power line
4. cooling water (CW)
5. second fuel
6. combustion chamber
7. distance indicator
8. combustion chamber adjustment
9. calibration standard for temperature measurement
10. mass flowmeter
11. check valve
12. suction pump
13. cooling water outlet
14. combustion chamber
15. thrust
16. microphone
17. nozzle exhaust temperature
18. combustion chamber temperature
19. high-speed camera
20. cooling water outlet
21. strain gauge bridge
22. camera speed
23. oscilloscope
24. recorder
25. frequency analyzer (instability)
26. fuel

/80

Figure 36. General view of the combustion chamber test stand

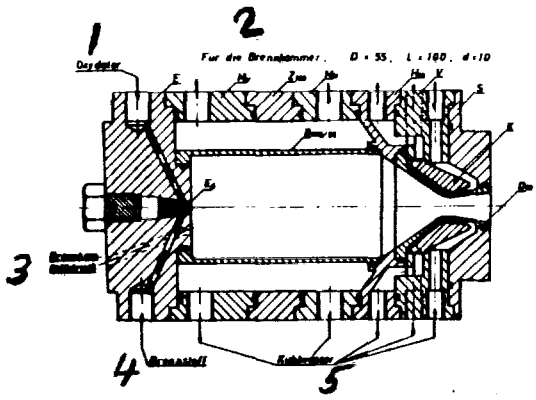

Figure 37. Cross section of the combustion chamber

1. oxidizer
2. for the combustion chamber
3. combustion chamber pressure
4. fuel
5. cooling water

b. Combustion chamber design

It was required of the combustion chamber design that setup and breakdown should be possible in the shortest time, and that the combustion chamber parts and the injection head be easily exchangeable for changing the geometric dimension.

As shown in Figure 37, the combustion chamber in the standard design consists of the outer jacket and the cylindrical inner part. The jacket consists of individual /81 segments, with one end formed by the injection head while the other end serves as the nozzle mount. The inner chamber is supported at both ends, and can be moved slightly in the axial direction because of the strong expansion. The combustion chamber and nozzle are independently water-cooled. On cooling, segment K provides for the nozzle cooling. The cooling channel in the vicinity of the narrowest cross section is only 1 mm thick. This makes possible sufficient coolant flow rate for the necessary high heat removal at this point. All the parts are sealed by O-rings.

After assembly of the individual parts, the combustion chamber is clamped hydraulically to the combustion chamber table. After connection of the supply lines the chamber is ready to operate. Because of the hydraulic clamping, no bolting is needed, so that mounting is greatly simplified.

By changing the nozzle holder H, combustion chambers with different diameters (D = 45 - 70 mm) can be investigated. By changing the intermediate section Z, combustion chambers with different lengths (L = 75 to 150 mm)can be investigated. Nozzle changes and changes at the injection head can be made without problem. Use of the building block principle provides a large number of characteristic combustion chamber lengths, L*.

The mixture preparation is very difficult for small combustion chambers because two liquid components must be mixed together homogeneously in the minimum time and minimum space. It is well known [50] that for small combustion chambers only injection heads that provide mixing by impact of the two injection streams are usable. That is, mixing occurs even in the liquid phase. Therefore, only these types were considered for these investigations. In order to be able to study combustion processes, various combustion chambers with windows or transparent walls were used [51, 52]. The windows must meet the combustion chamber wall exactly on the inside to prevent perturbations of the boundary layer. Use of combustion chambers with rectangular cross section cannot be considered optimal. Heidman et al. also performed experiments with Plexiglass combustion chambers [50] but the material partly burned, and this portion had to be considered in the evaluation.

Our initial experiments with lateral slots of fused quartz on a cooled combustion chamber were not successful because an opaque deposit formed quickly on the insides of the windows because of /82
the cold window. Therefore, uncooled combustion chambers of Jena ["Pyrex"] glass were used. These combustion chambers were used in the usual manner as inner chambers, and the outer chamber was provided with a wide slot at both sides, and served only as the supporting jacket for the hydraulic clamping. To be sure, these chambers allow only about 10 seconds of operation until they are destroyed, but this is not a problem in performing the tests because they are easily changed. No deposit forms on the walls, so that optical investigations can be carried out with good accuracy and reproducibilty.

4. Effect of design and operating characteristics on the power behavior of the experimental combustion chamber.

It was not possible to design the model combustion chamber with sufficient accuracy from theoretical considerations. Therefore, various injection heads were investigated with respect to their behavior on initiation of combustion, because the nature of the mixture preparation is important for the engine power. The characteristic velocity and the development of the gas velocity in the combustion chamber were also studied comparatively in order to determine the optimal conditions at various operating conditions for the planned combustion chamber. This appeared particularly necessary because use of the test stand could provide temperature measurements which could be compared with corresponding theoretical values at satisfactory accuracy only if the course of the combustion can be controlled satisfactorily in all the phases.

Out of a large number of injection heads investigated, four characteristic fundamental types are shown in Figure 38. As a particular characteristic, all four types exhibit mixing of oxidizer and fuel in the liquid phase. The intensity of the mixing differs in the individual types due to variation in the number of holes, the hole diameters, the injection angle and the free path. For injection head E 6 the liquid is distributed in a full cone. With the turbulent injection head E 7 both injection openings open tangentially into a short mixing channel, so as to give both components rotation in the same direction along the wall of the mixing chamber. The mixing chamber length was designed so that the residence time of the fuel in the chamber is in every case below the ignition delay time, because ignition within the

mixing chamber is to be avoided. In the water test the injection picture shows a conical jacket with an angle of 58°.

The atomization with injection head E 8/1 is good, although the elliptic cone only partially fills the combustion chamber on the narrow side. /83

By changing the position and number of the fuel holes, the type E 8/4 was developed from the head E 8/1. In this way a larger part of the combustion chamber could be filled by the injection stream (see Figure 38). With the injection head types E 8/1 and E 8/4 the injection openings are very near each other so that the meeting point of the two streams is almost in the plane of the injection head. The injection head E 8/2 investigated in Section C 5 c has larger hole diameters in comparison with the type E 8/1, so that the injection pressure drop is smaller.

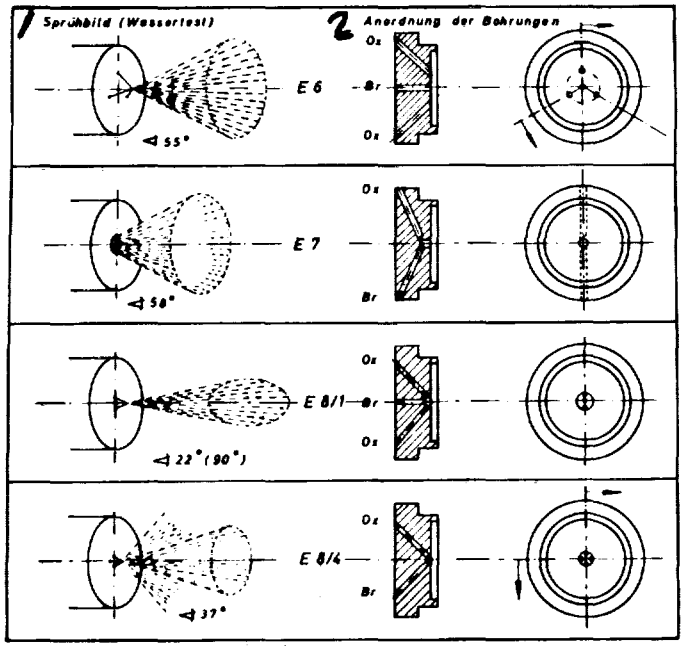

Figure 38. Comparison of the injection heads investigated
1. Spray picture (water test)
2. Arrangement of the holes

High-speed photography was used to expand knowledge of the ignition and combustion process. An AEG time-expander camera was available for the measurements. /84

Using that camera, individual pictures were made of the injection process in rapid sequence (1200 to 3000 pictures per second), using transparent combustion chambers without nozzles, with a lighted background. A high-intensity high-pressure mercury lamp was used for illumination.

Figure 39 shows, as an example, the injection processes of heads E 6, E 7 and E 8/1 up to ignition.

With head E 6 the reactions in the liquid phase produce a gas cloud at the contact point of the jets. The gaseous reaction products gradually fill the combustion chamber. Ignition occurs relatively late with an ignition delay time of 35 ms, in the gas cloud about in the center of the combustion chamber. No distinct ignition center could be observed.

In contrast, in the test with injection head E 7 it could be determined that ignition occurred near the injection head plane. The delay time could be reduced to 15 ms, apparently due to intensive mixing and turbulence during the liquid phase in the mixing chamber. The mixture distribution is not quite satisfactory with this injection head, though, because large collections of droplets were observed in the combustion zone.

This disadvantage was avoided with injection head E 8/1. Here the flame front fills the entire combustion chamber immediately after ignition. As there are no unburned fuel

residues near the injection head in the initial phase of combustion, we can conclude that the mixture preparation was good and that the ignition delay time is very small.

Along with the qualitative observation of the injection and mixing processes up to ignition, measurements were made of the gas velocities with different injection head types, using transparent combustion chambers with thrust nozzles. Here the film runs at speeds of up to 20 m/s past a narrow slit in the center of the camera which is parallel with the combustion chamber axis. The light traces from the radiating particles form a certain angle with the film direction, from which the particle speed can be determined if the geometry is known and the film speed is measured [10, 17]. Figure 44 shows a film section of this measurement.

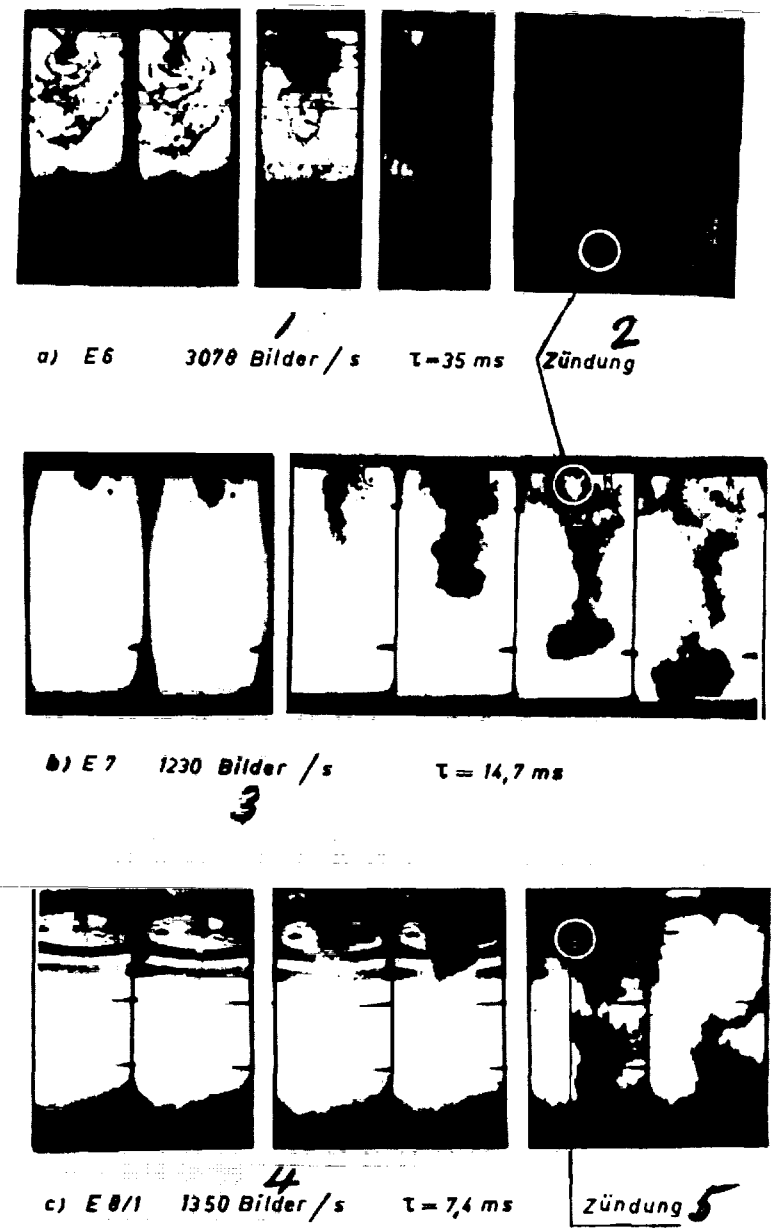

Figure 39. Injection process with different injection heads. Film direction: -->

1. 3078 frames/second
2. ignition
3. 1230 frames/second
4. 1350 frames/second
5. ignition

The experimentally determined gas velocities for the injection head types investigated are plotted in Figure 40. In general, there is a continuous rise in velocity with increasing distance from the injection head. /86

Because of the faster mixing, the gas velocities with types E 8/1 and E 8/4 take on high values even near the injection head. With injection head E 6, for which the contact point of the jets is farther from the injection head plane, the velocities are at first comparatively low. Injection head E 8/2 has poor combustion characteristics. The turbulent injection head E 7 shows moderate quality. With this head, no measurement could be performed because of severe turbulence in the front half of the combustion chamber.

According to the discussions in B 1 a, the characteristic velocity is measured according to Equation (7) by determining the fuel throughput and the combustion chamber pressure.

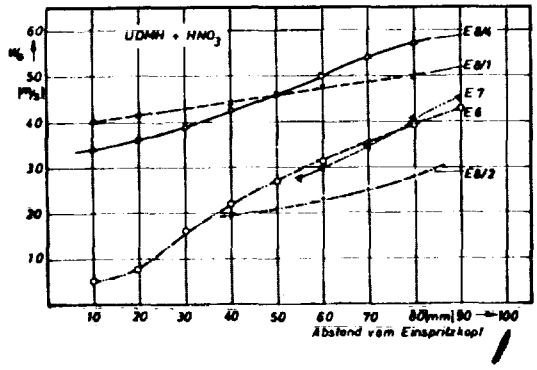

Figure 40. Comparison of the gas velocities with different injection head types.
P_1 ≈ 3 atm.
1. distance from the injection head

A quality factor can be determined by comparing the measurements with the theoretical values. This allows evaluation of the quality of combustion. Figure 41 shows the characteristic velocities for two experimental series. The highest values were attained at λ = 0.7 to 0.8, in agreement with the theory (Figure 11). The quality factor for the smallest motor lies between 0.8 and 0.9, and reaches the value φ_c^* = 0.95 only at pressures of 10 atm and λ = 0.8 (Figure 42a). The quality factor φ_c^* depends strongly on the combustion chamber geometry, along with the operating parameters, as is shown in Figure 42.

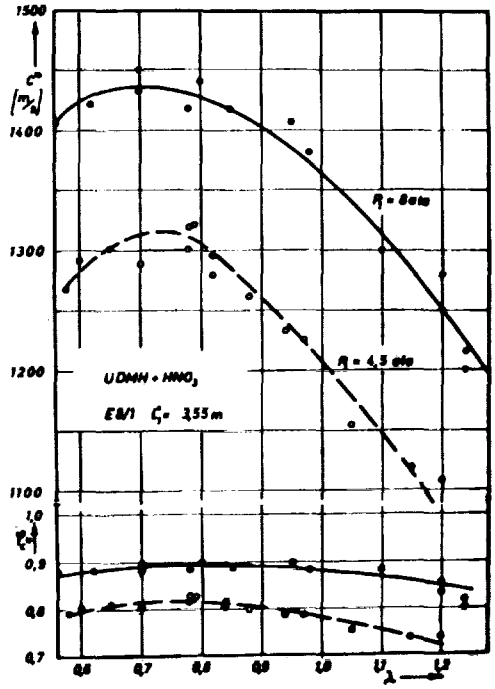

Figure 41. Curves for the characteristic velocity and the quality factor as functions of the oxygen carrier ratio.

Figure 42. Change of the quality factor.

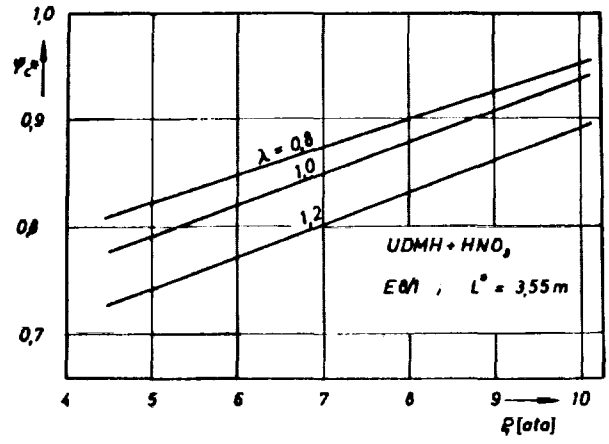

a) as a function of the operating conditions

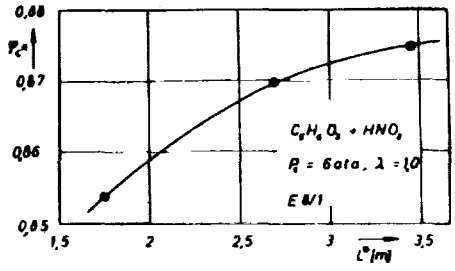

b) as a function of the combustion chamber geometry

At the same operating conditions the quality of combustion approaches a maximum with increasing L* value. No differences in characteristic velocities could be determined for the injection heads E 8/1 and E 8/4. Head E 8/2 had a

lower value. In seeking reasons for this drop in power, /88
instability phenomena were found. They were specially considered because of their importance for the combustion.

5. Determination of combustion instabilities with and without metal admixture /89

a. Preparation of metal suspensions

While it is relatively easy to imbed fine metal particles in the fuel of solid-fuel motors, there are great difficulties with liquid fuels, especially in production of a storable suspension. E. SÄnger has already reported suggestions for stabilizing fuel suspensions; but comparatively high metal concentrations were desired.

Experiments with solid fuel motors have shown that metal-enriched fuels can contribute to reducing instability phenomena [8]. As part of the present study, the effect of aluminum admixtures on the stability of combustion in liquid combustion chambers was investigated.

Because of the different density of the fuel (furfuryl alcohol $\delta_{20} = 1.129$ g/cm³) and aluminum ($\delta_{20} =$ 2.7 g/cm³) a suspending agent must be found which will keep aluminum particles with a maximum grain size of < 40 µ suspended for a long time after successful mixing.

According to investigations of M. L. Pinns [54, 55], polyoxyethylene sorbitan monooleate, aluminum octoate and glycerol sorbitan laurate appear to be the most practical.

Because of problems in obtaining those materials, our own experiments were performed with the following six suspending agents:

Sodium lignosulfonate (Zellstoff-Waldhof AG)
Genopol C-050, O-020, and X-050 (Farbwerke Hoechst AG)
Filler R 972 and Aerosil 2491/380 (Degussa AG)

For the measurements, the concentrations of the suspending agent and the metal were changed, as was the stirring time. As a measure of the quality of the suspension, the height h of the metal column as compared to the total height of the fuel in a measuring cylinder was evaluated as a function of the time. A suspension was considered usable for this application if the relative height h was at least 95% after a standing time of 10 hours. Furthermore, all mixtures were tested for their hypergolicity. Retention of their auto-ignition properties must be considered a basic prerequisite.

From this viewpoint, sodium lignosulfonate is unsuitable, /91 because it is not satisfactorily soluble in furfuryl alcohol. The Genopol substances C-050, O-020 and X-050 are quite soluble, to be sure, but cannot suspend metal particles. Also, the ignition delay times are too long for all three types of Genopol. Filler R 972 shows moderate solubility and falls to the bottom after a short time. Aerosil 2491/380, on the other hand, meets all the specified conditions.

This material consists of more than 99.8% SiO_2 with a particle size of 3 - 15 µ for the primary particles. The physical properties of the pure silicon dioxide powder can be reproduced strictly, due to the manufacturing process. The strength of the suspension, which depends on the stirring time, is shown in Figue 43a for the fuel

composition used in the instability experiments. At a stirring time of at least 3 hours by means of an electric propellor stirrer, a quality of 96.5% could be achieved for a standing time of 20 hours.

The concentration of the metal and of the suspending agent have a great effect on the quality of the mixture. The experimental results in Figure 43b show that the stability of the suspension rises with increasing aluminum and Aerosil concentration. /90

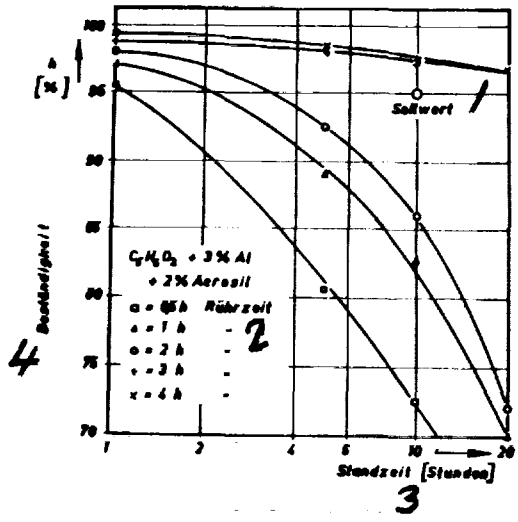

a) Effect of the stirring time

1. target value
2. stirring time
3. standing time (hours)
4. stability

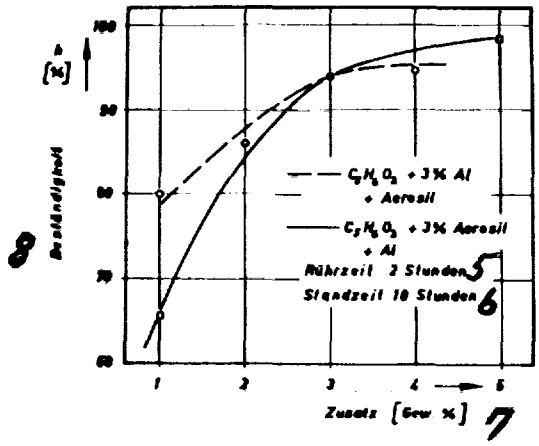

b) Effect of additions of metal and suspending agent

5. stirring time 2 hours
6. standing time 10 hours
7. addition [% by weight]
8. stability

Figure 43. Quality of hydrocarbon-aluminum suspensions

b. Measuring methods to determine instability influences, high-frequency vibrations

Combustion instabilities were determined experimentally both with a piezoelectric pressure transducer suitable for high-temperature combustion chambers (Kistler) and with a sound level meter (Rohde & Schwarz Type EZGN) combined with an octave band pass (Type PBO). Using the filter gives the possibility of separating the harmonics from the fundamentals, or even fading out a certain region from a large frequency spectrum. The frequency curves of the sound level meter were displayed on an oscilloscope and photographed for evaluation. With the quartz transducer the instantaneous pressure was plotted in the usual manner through an electrometer stage and an oscilloscope with a calibrated time base. In agreement with Tischler, the measurements showed that sound measurements are suited only for study of high-frequency vibrations [56]. The display of all the perturbing noise is considered a disadvantage of this method. Figure 45 shows the simultaneous recording of the frequency with both measuring methods.

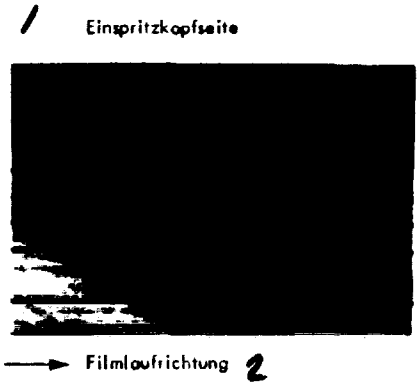

Figure 44. Development of the gas velocity in the combustion chamber
1. injection head side
2. film direction

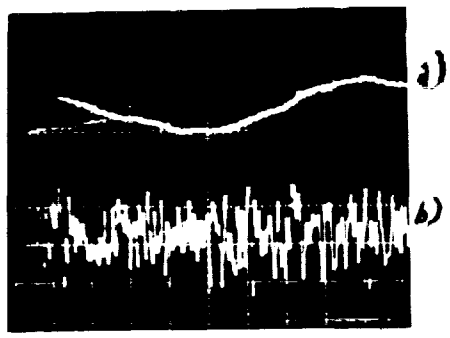

Figure 45 Display of the frequency course.
a. Quartz pressure transducer
b. Sound level meter

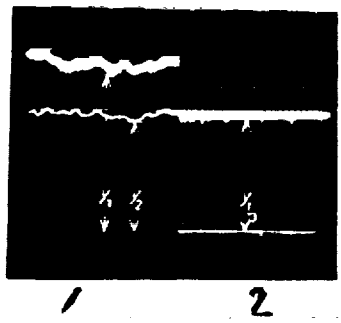

Figure 46. Temperature measurement
1. Measurement. 2. Calibration

High-frequency instabilities often originate due to /93
longitudinal sound vibrations in the combustion chamber [57]. For computer determination, the combustion chamber up to the narrowest cross section is considered as a tube of length L_{total} closed at both ends. Then the frequency is found to be:

$$f = \frac{c \cdot n}{2 \cdot L_{ges}} = \frac{0{,}36 \cdot c^{*} \cdot n}{L_{ges}} \qquad (128)$$

c = velocity of sound
n = harmonic factor to characterize the number of standing waves in the chamber

The frequency determined by the sound level meter diverges by 7% from the high-frequency instability calculated from Relation (128). As the quality of combustion is not reduced by the strong turbulence with high-frequency instability, essentially only the low-frequency instability was investigated, because it can have an unfavorable effect on the course of combustion.

c. Results of the stability investigation

In considering instabilities, one must free oneself from the concept that the results can be represented in the form of well-defined lines. Rather, there are regions defined by the vibrations themselves, as combustion itself is not a strictly reproducible process [59]. The instability investigations were performed with the fuel combination $C_5H_6O_2$ + HNO_3. It appeared that the form of the injection head has a substantial effect on combustion stability. Figure 47 shows the mean pressure fluctuations for two different injection heads. Injection head E 8/4 has two oxidizer openings and two fuel openings, while injection head E 8/2 has only one injection opening for each component. The injection pressure drops are higher for head E 8/4. The amplitude fluctuations for this injection head are in the range of 0.02 - 0.04 atm, with a very narrow range of variation. For the other injection head, E 8/2, the severe scattering of the experimental points indicates considerable instability, so that this injection head must be evaluated unfavorably. From a comparative study of the power of the two injection heads, according to Figure 48, it can be seen that the characteristic velocity for the unstable head in the optimal operating range is some 6% below the corresponding value for head E 8/4. Because of this finding, the type E 8/2 was not used in the other studies, and especially for temperature measurements.

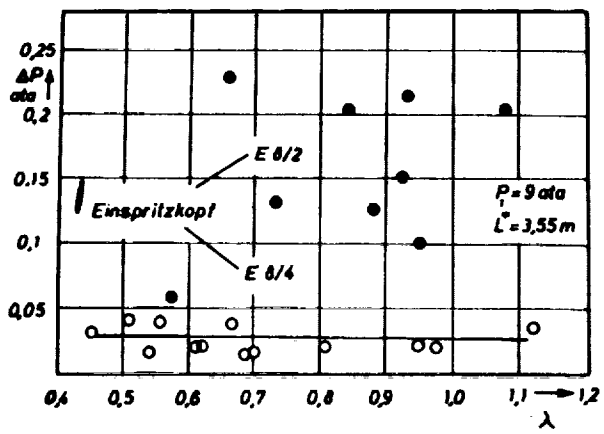

Figure 47. Amplitudes of the pressure fluctuation in the combustion chamber with stable and unstable combustion

1. injection head

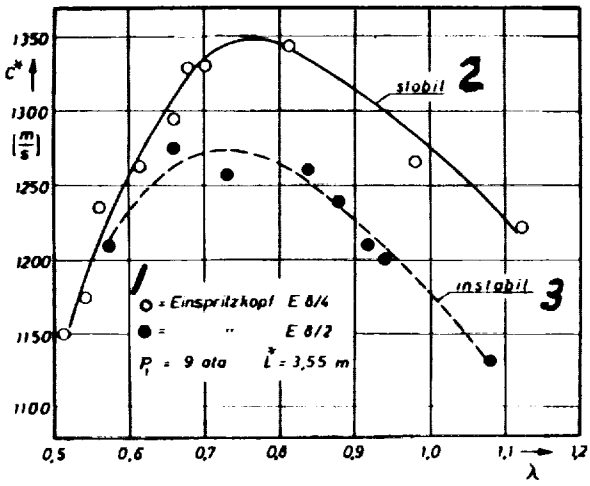

Figure 48. Effect of the instability on the characteristic velocity

1. injection head.
2. stable
3. unstable

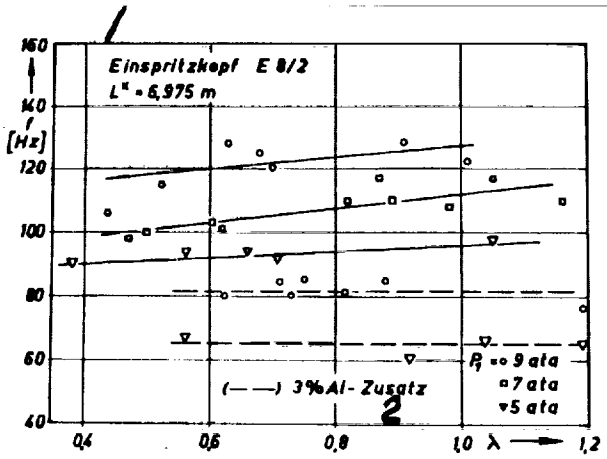

ORIGINAL PAGE IS
OF POOR QUALITY

a. Considering the oxygen carrier ratio

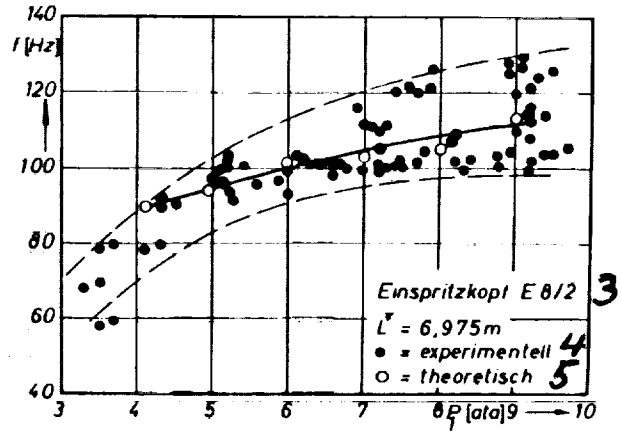

b. Without considering the oxygen carrier ratio

Figure 49. Dependence of the instability frequency on the combustion chamber pressure.

1. injection head E 8/2
2. 3% Al addition
3. injection head E 8/2
4. experimental
5. theoretical

The operating conditions and design values have a substantial effect on the frequency of vibration. Accurate knowledge of this frequency is important in order to be able to avoid resonant vibrations within the engine. The measured frequencies at different combustion chamber pressures are plotted in Figure 49. While a notable increase in frequency was observed with increasing combustion chamber pressure, no dependency of the vibrational frequency on the oxygen carrier ratio can be detected at low pressures. At higher pressures a slight increase can be seen with increasing λ . The frequency can be reduced by adding 3% aluminum; for instance, from 120 Hz to 80 Hz at a combustion chamber pressure of P_1 = 9 atm.

In order to establish the effect of combustion chamber geometry on the vibration frequency, several series of experiments were performed with different characteristic lengths L^*. The vibration frequency decreases with increasing length, and the decrease is less for higher than for lower pressures. In the comparison of the experimental results with those determined according to Formula (124) in Figures 49b and 50, the geometric dimensions and operating data for the individual experiments were used.

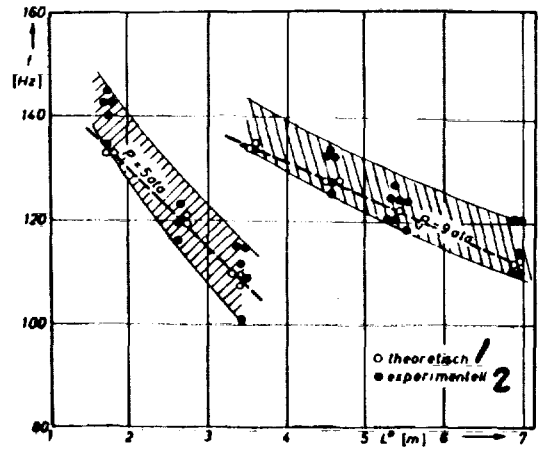

Figure 50. Effect of the characteristic length on the instability frequency
1. theoretical. 2. experimental

The pressure loss in the check valve is $\overline{\Delta P_R}$ = 1 atm. A linear dependence on the characteristic length is assumed for the combustion chamber characteristic number z according to the considerations in B 1 c (z = 0.85 at L* = 1.5 m; z = 0.97 at L* = 6.975 m). The delay, θ, is assumed constant at 0.02 sec. With different injection pressures for the two components, we consider that $P_T = 1/2 \cdot (P_{Ox} + P_{Fuel})$. /97

The theoretically calculated values lie within the range of variation of the experimental results. Formula (124) can, then, be considered a useful criterion for determining the vibration frequency in case of unstable combustion vibrations.

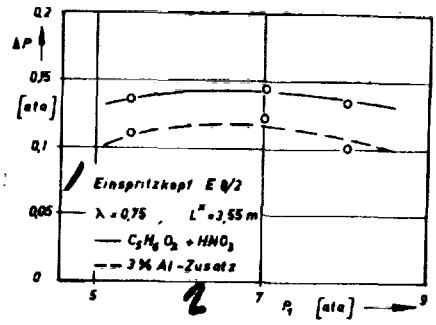

Figure 51. Effect of adding aluminum on the instability amplitude

1. injection head E 8/2
2. 3% Al added

Adding aluminum has no great effect on the amplitude of the instability, so that from these investigations we cannot say there is any notable damping of combustion instabilities. This result agrees with that of [60], but contradicts that of Horton and Mc. Gie [8], although those studies referred solely to solid fuel engines. Furthermore, slight deposits of Al_2O_3 were detected in the nozzle when aluminum was added. No effect of metal addition on power could be found.

In order to establish the stability limits for specified combustion chamber geometry, measurements were carried out with different oxygen carrier ratios in the pressure range of 4 to 10 atm.

An amplitude of 1% is used as the criterion to distinguish between stable and unstable combustion. That is, if the /38 amplitude of the pressure vibration exceeds 1% of the

combustion chamber pressue, the combustion is considered unstable. With this definition, it was possible to find a limit curve establishing the stable operating range (see Figure 52). With increasing distance of the operating point from the limiting curve,the instability amplitudes increase, or vanish completely.

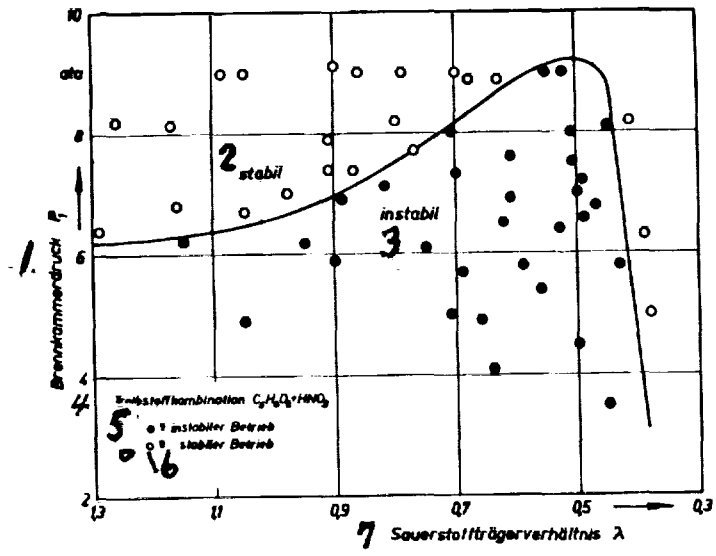

Figure 52. Instability region of the combustion chamber (E 8/2).

1. combustion chamber pressure
2. stable
3. unstable
4. fuel combination $C_5H_6O_2$ + HNO_3
5. unstable range
6. stable range
7. oxygen carrier ratio

Suitable engine parameters could be found for the model combustion chamber, based on the instability measurements. This provided better prerequisites for the further experimental investigations, and especially for the temperature measurements. Reproducibility of the measurements is assured only with adequate stability of the

operating point. It must be concluded from the studies that the injection head has the greatest effect on the stability of small engines. The injection heads E 8/1 and E 8/4 (see Figure 38) proved usable, so that further investigations were done essentially with those types.

6. Temperature measurements using the spectral line inversion method /99

a. Combustion chamber temperatures

Because of the high gas temperatures prevailing in the combustion chambers of high-temperature engines, devices requiring direct contact with the medium measured (e. g., thermocouples) are generally ruled out. The spectral line inversion method with sodium [2, 28, 61] proved to be a usable method for measurement. The measurement principle consists of comparison of the radiation intensity of the flame with the intensity of a calibrated radiation source (tungsten ribbon lamp). The calibration was done using a micro-pyrometer tested by the Federal Physical Technical Institute.

Figure 53 shows the principle of the measurement. Accurate descriptions of the procedure, including the various modifications, have been published many times, so that no explanation is needed here [3, 10]. The true flame

temperature is determined, according to [10], by use of the relation

$$T_F = \frac{T_s}{1 - T_s \frac{\lambda}{c_2} \cdot \ln \frac{y_1}{y_1 - y_2 + y_3}} \qquad (129)$$

where y_1 = energy of the incandescent wire (tungsten ribbon lamp)

y_2 = energy of the flame + energy of the incandescent wire after passing through the flame

y_3 = energy of the flame

T_s = black-body radiation tempertature of the lamp

λ = wavelength

c_2 = radiation constant

As mentioned previously in Section c 3 b, transparent glass combustion chambers were used to determine the combustion temperature. The corresponding calibration curves for the individual measuring elements including the absorption and scattering of the glass wall are given in Figure 54. The intensities were shown on the oscilloscope and photographed for evaluation (see Figure 46).

Sodium nitrate, $NaNO_3$, was added to the oxidizer at 1% to color the flame.

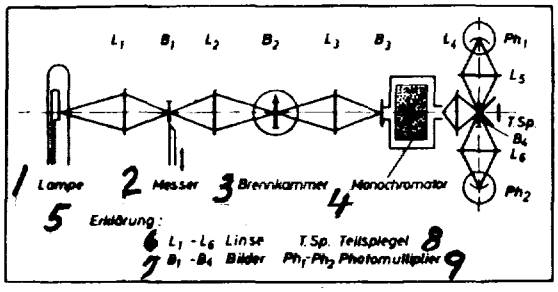

Figure 53. Principle of temperature measurement using the spectral line inversion method

1. lamp
2. meter
3. combustion chamber
4. monochromator
5. explanation
6. lenses
7. images
8. partial mirror
9. photomultipliers

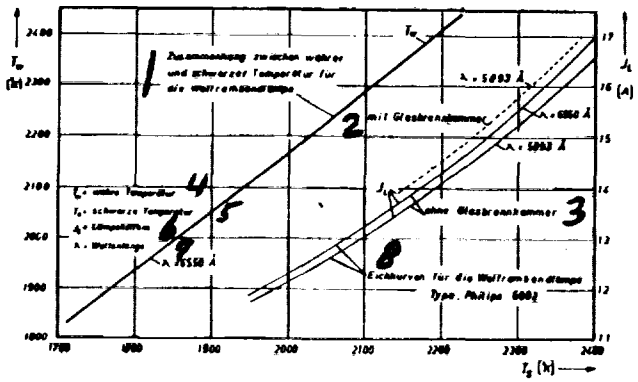

Figure 54. Calibration curves for temperature measurement by the spectral line inversion method

1. relation between true and black-body temperature for the tungsten ribbon lamp
2. with glass combustion chamber
3. without glass combustion chamber
4. true temperature
5. black-body temperature
6. lamp current
7. wavelength
8. calibration curves for for tungsten tape lamp

Effects on the flame from the boundary layer and from /100 inhomogeneities in the flame are not considered here; but investigations have shown that the error is small [28, 63]. The total inaccuracy is reported to be ± 1.5% in the temperature range 2000 to 2600 °K [63].

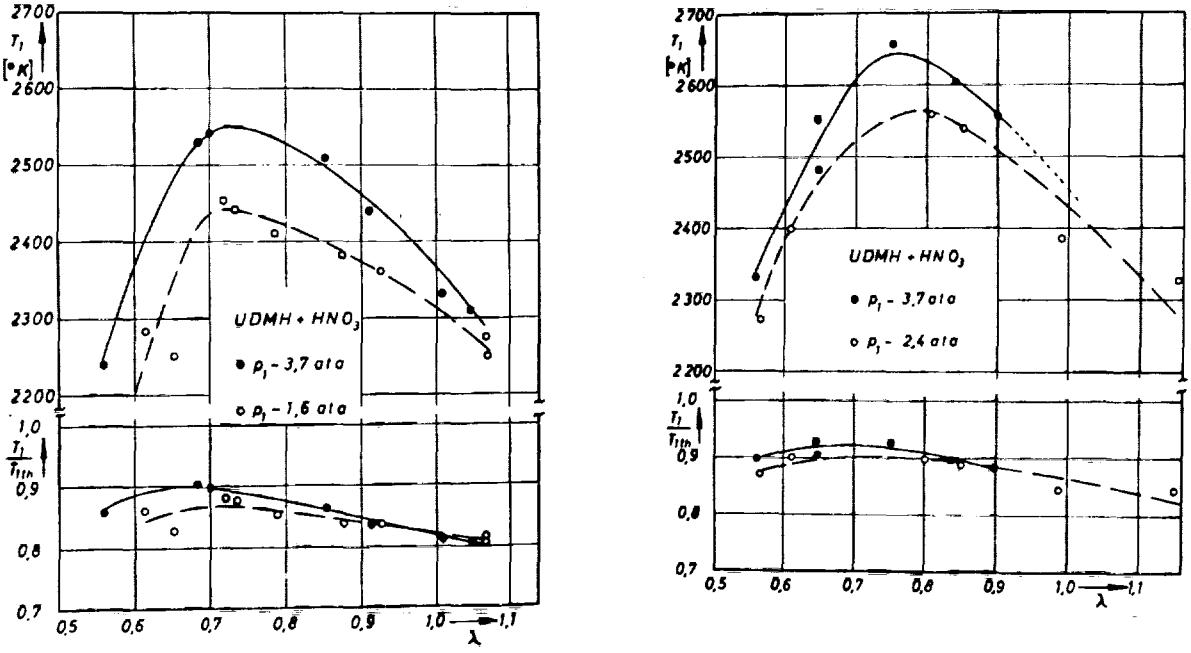

Figure 55. Measured combustion chamber temperature and comparison with the theoretical values
a. Combustion chamber length L = 50 mm
b. Combustion chamber length L = 127 mm

For the temperature measurements in the chamber, only pressures below 4 atm could be realized because of the

danger of immediate destruction of the combustion chamber. As the completeness of combustion depends strongly on the /102 path available, combustion chambers 50 and 127 mm long were used. Figure 55 shows the results of the temperature measurement.

The highest temperatures were measured at oxygen carrier ratios of λ = 0.7 to 0.8, while the theoretical maxima occur at λ = 0.85 to 0.9 (Figure 6). Only about 85 to 90% of the theoretical combustion temperature was attained. The reason is considered to be heating up of the combustion chamber and still-incomplete combustion. With larger combustion chambers with many injection openings the mixture distribution is generally better, so that comparatively higher temperatures can be expected.

The best combustion was attained with large fuel excess (λ = 0.65 to 0.7). Apparently the best mixture preparation occurs here, with the injection head E 8/1 which was used, independent of the pressure and of the combustion chamber length. With increasing combustion chamber pressure and increasing chamber length, the difference between the theoretical and experimental values decreases, and the pressure effect diminishes with increasing values of λ .

The three-dimensional representation of the temperature as a function of the oxygen carrier ratio and the characteristic length, in Figure 56, shows clearly the effect of these characteristic values on the measured temperatures. With the existing combustion chamber arrangement, higher characteristic lengths also correspond to greater effective combustion chamber lengths. The combustion temperature rises steeply with L* values below 2 m and approaches a limit with increasing length.

As the combustion chamber would have to be be cooled at longer operating times, there would be a decrease in temperature with increasing length due to the strong heat removal, so that optimization of the combustion chamber length is possible from the temperature curve. For the fuel combination used, a characteristic length of $L^* \geq 2$ m can be considered the minimum size for small engines. The temperature maximum shifts from $\bar{\lambda} = 0.7$ at a low characteristic length to $\bar{\lambda} = 0.76$ for larger values of L^*.

To summarize, it can be stated that temperature measurements in the combustion chamber are suitable for investigation of the combustion and the mixture preparation.

/103

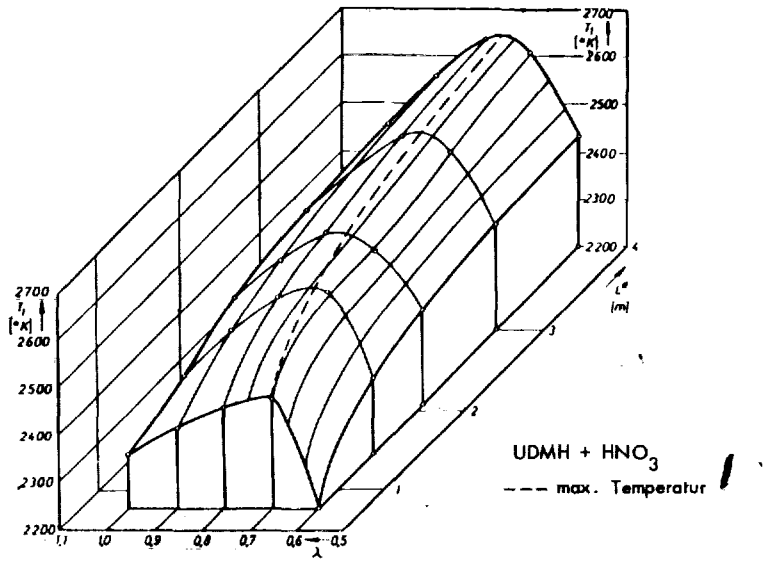

Figure 56. Temperature profile measured with changes of the combustion chamber geometry
1. maximum temperature

b. Final expansion temperatures and consideration of recombination processes on the basis of temperature measurements

In order to determine the temperature of the exhaust gas jet behind the nozzle, the combustion chamber table was set so that the measurement plane was 4 mm behind the end of the nozzle. The temperature measurements were performed for combustion chamber pressures of 3, 5, 6, 8 and 10 atm with variation of the mixture ratio. Different nozzles were used to compensate for ambient pressure and nozzle pressure. In the region of under- or over-expansion temperature, comparisons between experimental and theoretical values and the power considerations derived from them are not possible under the specified conditions because temperature and power determinations are not reliable when the nozzles are not matched.

Heat transfer in the combustion chamber and in the nozzle gives too low an exit temperature for the gas in the measurement, in comparison to the values calculated theoretically without consideration of the heat transfer.

On the other hand, the temperature in the core of the jet is not as greatly affected by heat transfer as that in the zones near the wals. The method of spectral line inversion, however, measures a temperature value near the maximum temperature of the gas jet along the measuring path perpendicular to the jet axis [62]. /104

From this it can be concluded that considering the total heat transfer in the combustion chamber and in the nozzle yields excessively high experimental temperature values. To

estimate the actual situation, therefore, only heat transfer in the cooled nozzle was considered as a correction for the experimental measurements.

A method from Bartz [64] is used to determine the temperature difference due to heat transfer.

The heat transfer coefficient on the gas side is

$$\alpha_G = \left[\frac{0.026}{d_{min}^{0.2}} \cdot \left(\frac{\mu^{0.2} c_p}{Pr^{0.6}}\right)_t \cdot \left(\frac{p_t g}{c^*}\right)^{0.8} \cdot \left(\frac{d_{min}}{R_s}\right)^{0.1} \right] \left(\frac{F_{min}}{F}\right)^{0.9} \cdot \sigma \qquad (130)$$

with

$$\sigma = \left[\frac{T_{wG}}{2 \cdot T_G}\left(1 + \frac{\kappa - 1}{2} Ma^2\right) + \frac{1}{2}\right]^{-0.68} \cdot \left[1 + \frac{\kappa - 1}{2} Ma^2\right]^{-0.12} \qquad (131)$$

The factor σ considers the changes of the material values in the boundary layer.

The material values used for the calculation are:

$$Pr = \frac{4\kappa}{9\kappa - 5},$$

$$\mu = 0.8 \cdot 10^{-3} \text{ g/cm·s}.$$

Further, frozen equilibrium is assumed for the heat transfer calculation.

For an aluminum nozzle, the wall temperature on the gas side is between 400 and 700°K, with the highest value at the nozzle throat.

The calculations were performed for two of the nozzles used with throat diameters of 7.15 and 10.2 mm. From the heat transfer number, the nozzle geometry and the temperature difference between the gas temperature, T_s and the wall

temperature on the gas side, T_{WG}, the heat removed by the nozzle is given by the relation:

$$Q = \int_{x=0}^{l} \alpha_G(x) \cdot F(x) \cdot (T_G - T_{WG})(x) \qquad (132)$$

(132) is solved by dividing the nozzle into 10 segments. /105

$$Q = \sum_{i=1}^{10} \alpha(i) \cdot F(i) \cdot (\Delta T)(i) \qquad (133)$$

From the mass throughput specified by the experiment, and the mean specific heat of the gas, the temperature difference is approximated as

$$\Delta T = \frac{Q}{c_p \cdot M_G} \; [°K] \qquad (134)$$

A temperature of $0.9 \cdot T_{theor}$ was used for the gas temperature, T_G.

Temperature differences of 80° - 140° were found from the calculation above, depending on the mixture ratio, combustion chamber pressure and nozzle geometry. These values agree with those of Boynton [9]. The measured temperature values are corrected with these computed data.

Only the nozzle was cooled in the experiments. The radiative heat transfer was not considered because it does not decisively affect the result [10].

As a rule, the temperature measurements at the individual experimental points are evaluated so that the highest and lowest values were omitted. The variation of the experimental points becomes less with increasing combustion chamber pressure. At P_1 = 3 atm the measured points spread over a range of at most 100°K, while a spread of less than 50°K was found at P_1 = 10 atm.

The results from the temperature measurements are shown in Figures 57 to 60. Both the measurements corrected for heat transfer and the means without considering heat transfer are plotted.

In general, the temperature found for the fuel combination used, unsymmetrical dimethylhydrazine + nitric acid, is between the boundaries for chemical and frozen equilibrium, which are also shown.

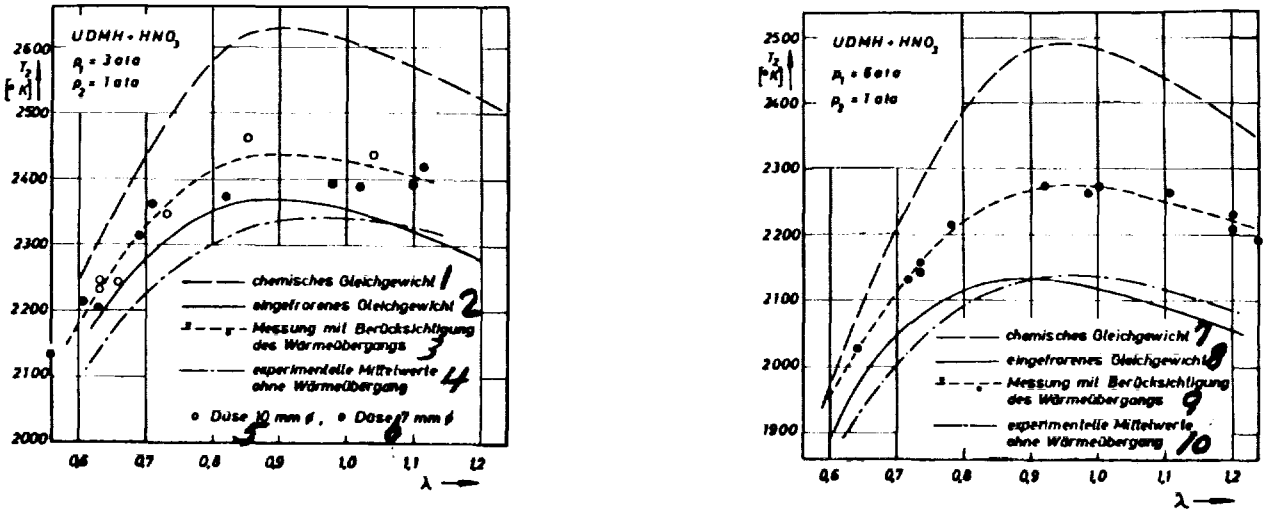

Figure 57. Measured final expansion temperatures compared with the theoretical values

1. chemical equilibrium
2. frozen equilibrium
3. measurement considering heat transfer
4. experimental measurement without heat transfer
5. nozzle
6. nozzle
7. chemical equilibrium
8. frozen equilibrium
9. measurement considering heat transfer
10. experimental measurement without heat transfer

ORIGINAL PAGE IS
OF POOR QUALITY

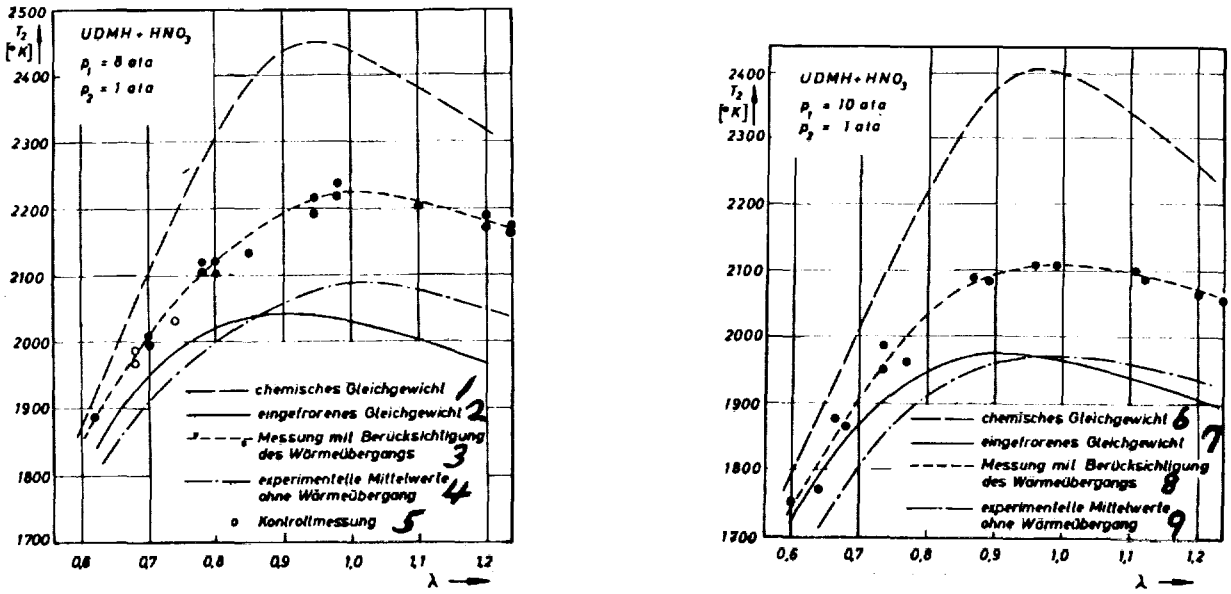

Figure 58. Measured final expansion temperatures compared with the theoretical values

1. chemical equilibrium
2. frozen equilibrium
3. measurement considering heat transfer
4. experimental measurement without heat transfer
5. control measurement
6. chemical equilibrium
7. frozen equilibrium
8. measurement considering heat transfer
9. experimental measurement without heat transfer

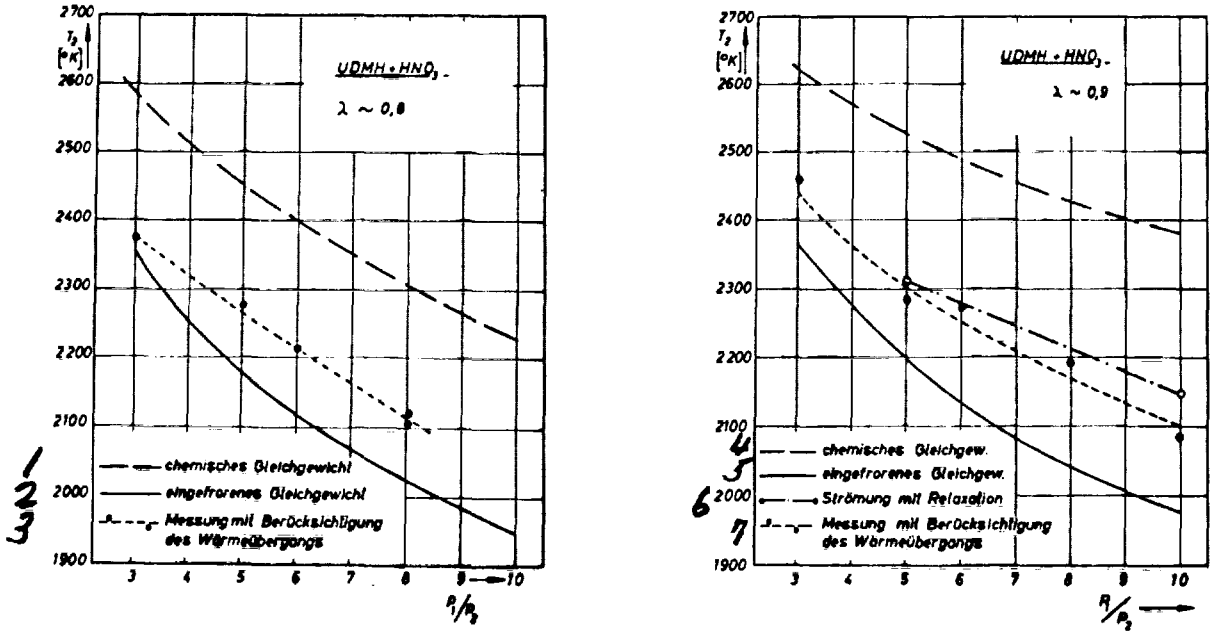

Figure 59. Comparison of the theoretical final expansion temperature with the experimental values as a function of the pressure ratio; P_e = 1 atm.

1. chemical equilibrium
2. frozen equilibrium
3. measurement considering heat transfer
4. chemical equilibrium
5. frozen equilibrium
6. flow with relaxation
7. measurement considering heat transfer

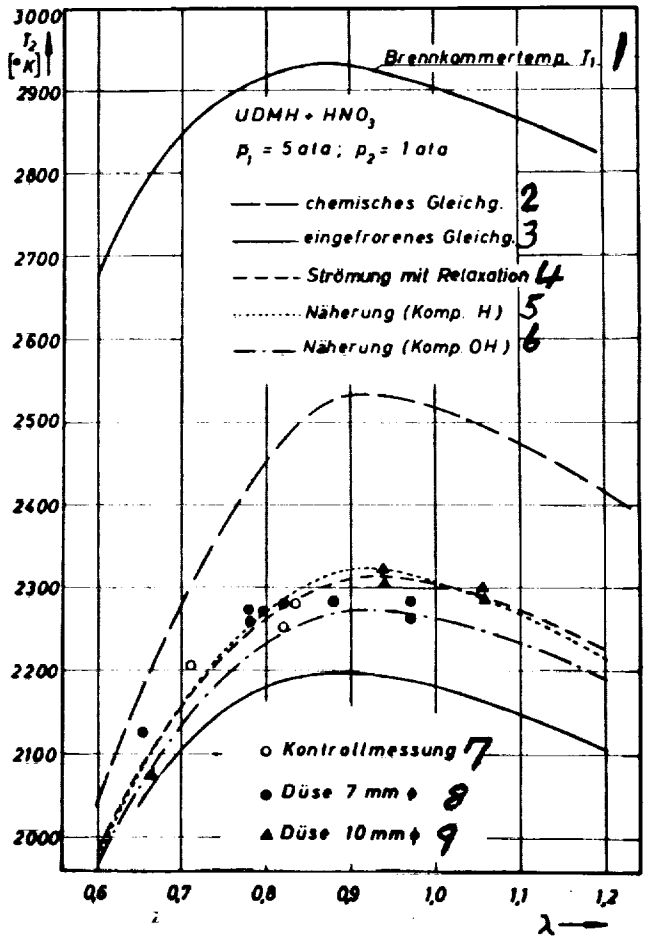

Figure 60. Experimental final expansion temperature with consideration of heat transfer in the nozzle, compared with the theoretical values assuming different expansion hypotheses

1. combustion chamber temperature
2. chemical equilibrium
3. frozen equilibrium
4. flow with relaxation
5. approximation (comp. H)
6. approximation (comp. OH)
7. control measurement
8. nozzle 7 mm diameter
9. nozzle 10 mm diameter

Determination of the temperature is valuable for consideration of recombination effects because the differences between the limiting cases are relatively large. /109

Here determinations of the concentrations of individual components of the reaction are suitable for detailed studies, along with temperature measurements; but they are extremely difficult to do with the necessary accuracy.

Pressure measurements generally do not give a satisfactory result because of the small pressure differences between the hypothetical limiting cases, even though one can realize large pressure ratios experimentally.

It can be seen from the temperature measurement that the flow runs near the frozen equilibrium at low pressure ratios, while at increasing combustion chamber pressures recombination effects raise the temperature. This phenomenon also appears in consideration of the measurements as they are affected by the pressure ratio, according to Figure 59. The temperature curve compared with the limiting values on combustion of other hydrocarbon-oxygen mixtures has been investigated occasionally recently, and similar results were obtained [9, 31, 65, 66].

As only very small nozzle dimensions could be realized in these experiments, substantial recombination gains could not be expected because of the short residence times of the combustion gases in the nozzle and the finite reaction rates of recombination.

There are also uncertainties in evaluation of the measurements because of the small dimensions, the boundary

layer effect, and heat transfer. The temperatures corrected for heat transfer can be considered to be the upper limits, while the uncorrected temperatures are the lower limits. The actually prevailing temperatures will lie between these limits.

It is of particular interest to answer the question of the extent of agreement of the measurements with the theoretically computed kinetic solution. Because of the relatively long computing time, the comparison computation could be performed only for some points. Nevertheless, one can conclude from the presentation in Section C 3 that similar results are also to be expected for other operating conditions.

Figure 60 compares the final expansion temperatures calculated theoretically for a combustion chamber pressure of 5 atm, considering the finite recombination rates, with the corrected experimental measurements. It appears that /111
the experimental measurements are near the theoretical values. From this one can conclude, as an approximation, that consideration of heat transfer in the manner stated approaches the real conditions. In order to increase the reliability of the experimental values, Nozzles with different narrowest cross section were used at this combustion chamber pressure. Also, control measurements were performed some time later to study the reproducibility. The corresponding measurements are emphasized in Figure 60.

In order to check the approximation method of Bray, the final expansion temperatures considering the components H and OH are plotted in Figure 60. Here it can be seen that slightly too high values appear with hydrogen, while the component OH lies at the lower limit of the measurement range.

In all, though, one can see that the method of Bray yields values that agree with the experimental results for the fuel combination used, and using the decisive reaction equation for the entire process.

D. SUMMARY /112

This work is theoretically and experimentally concerned with the dependences of various important influential values in ignition, combustion and expansion of hypergolic liquid fuels in small thermal high-temperature engines.

The usual characteristic values for rocket engines are summarily presented. In particular, a relation was developed for approximation of the combustion chamber volume required for combustion. This depends on the thermodynamic gas properties, the reaction rate and a design parameter.

The question of the extent to which the change of the thermal quantities can be represented by averaging in nozzle expansion was intensively investigated, with various mean $\bar{\pi}$- values being used for power calculation. It appeared that for high-temperature systems no satisfactory results can be obtained with a single average applicable to the entire expansion.

By use of fast digital computers, it was possible to study the course of expansion, including reaction kinetic processes. This provided an extensive approximation to the actual expansion process, which was of great interest particularly with respect to the use of high-energy fuel combinations.

As expected, the computer results showed that the flow process with relaxation runs between the hypothetical limiting cases. At high combustion chamber pressure and

high combustion chamber temperature, the flow approaches chemical equilibrium, while at low combustion chamber pressure the flow is nearly frozen.

If one considers, for instance, the power difference between the limiting values for chemical and frozen equilibrium, then the kinetic solution for P_1 = 50 atm and $\bar{\lambda}$ = 0.9 is 68% above that for frozen equilibrium. On reduction of the combustion chamber pressure to P_1 = 5 atm, the energy recovered due to recombination diminishes to 30%.

It was shown, therefore, that the effect of the combustion chamber pressure on the energy recoverable through recombination is very significant. /113

The Bray approximation method for the fuel mixture studied was derived to supplement the kinetic solution. On consideration of various components and reaction equations the approximation to a large extent gave good agreement of the power and temperature with the kinetic solution. In particular, the deviations were less than 1% for the practically important operation with fuel excess. By studies with changing of the reaction rates and application of the approximation and introduction of an impulse figure it could be shown that the total power is decisively influenced by the course of the three-body water forming reaction $H + OH + M = H_2O + M$. Here an increase of the reaction rate by a factor of ten increased the recombination energy from 30% to 65% at $\bar{\lambda}$ = 0.9.

In the comparison of the concentrations of various exhaust gas components on expansion, no satisfactory agreement was found between the approximation and the exact kinetic calculation. Therefore, although one can, to be sure, make predictions about the approximate total course of the flow

on the basis of the approximation, it is not suited for detailed studies of the actual reaction mechanism.

Ignition delay measurements with the fuel system UDMH + HNO_3 give an increase in the delay time with decreasing pressure. At reduced pressures below 700 Torr no ignition could be obtained. For aluminum additions of more than 10% the τ-value became greater, and the ignition limit was reached at about 20%. Oxidizer lead by 30 to 100 msec produced the minimum ignition delays. Apparently the different preparation times for the two components are important here.

As combustion of liquid fuels in small engines presents special problems for mixture preparation, systematic studies were performed on the injection process, the gas velocity in the combustion chamber and the characteristic velocity; and instability phenomena were considered with admixture of aluminum to the fuel. As a result, decisive parameters for the process of combustion were shown and their interactions in combustion were analyzed.

For instance, testing of various types of injection heads showed that among the designs tested, the design with two /114
holes for oxidizer and two holes for fuel gave the highest powers with stable combustion. The significant characteristic of this head is intensive mixing of the components in the liquid phase with small free spray paths.

Investigation of combustion instabilities gave a power drop of 6% for unstable combustion, and allowed marking off a stable operating region, which depends on both the mixing ratio and the combustion chamber pressure. The theoretical relation for the instability frequency, established in

connection with the instability investigations, gave values within the range of variation of the experimental measurements.

As temperature measurements of high-temperature systems offer good possibilities for comparison with theoretical results, the temperatures in the combustion chamber and behind the thrust nozzle were determined by the spectral line inversion method. The measured combustion chamber temperatures rise with increasing combustion chamber length, but because of incomplete combustion and heat loss at the wall they reach only about 90% of the theoretical values.

At a combustion chamber pressure of 3 atm the measured expansion temperatures run in the vicinity of frozen equilibrium. At pressures of 6 to 10 atm and $\overline{\lambda} = > 0.8$ the temperature values are 100 to 200°K higher than the lower theoretically determined limit. As the nozzle dimensions were very small, however, we cannot expect a substantial recombination recovery in comparison with larger engines.

Comparison of the temperatures corrected due to heat transfer to the cooled nozzle with the exact kinetic solution and the approximation method showed good agreement, so that from these studies the usefulness of temperature measurements for the approximate analysis of expansion processes in the temperature range considered can be confirmed.

A formula abbreviation

a number of chemically independent reactions

a function value

B formula abbreviation

[B] matrix

b apparent mean activation energy

C constant

c velocity of sound

C_F thrust coefficient

C_F^* characteristic thrust coefficient

c_p specific heat at constant pressure and frozen equilibrium

c_{v_f} specific heat at constant volume and frozen equilibrium

c_p specific heat of reacting gases at constant pressure

c_v^f specific heat of reacting gaes at constant volume

c^* characteristic velocity

D combustion chamber diameter

d diameter of the narrowest cross section

E frequency factor (reaction variable)

e reaction order

F cross section

f frequency

[S] matrix

g acceleration of gravity

H absolute molar enthalpy

h absolute specific enthalpy per unit mass of the gas mixture

ΔH heat of reaction at constant pressure

I_{sp} specific impulse

I impulse figure

$K_1^{(i)}$ reaction rate constant for the i-th forward reaction

$K_2^{(i)}$ reaction rate constant for the i-th reverse reaction

K_p rate constant

k constant (with index designation)

L length /116

L^* characteristic length

M molar mass

M_s mass throughput per second

Ma Mach number

M_s' relative mass proportion of the unburned fuel

m number of gas components

m_s' relative mass proportion of the burned fuel

N number of chemical reactions

n specific mole number per unit mass of the gas mixture

P pressure

Pr Prandtl number

Q quantity of heat

R universal gas constant

R_s radius of the nozzle contour at the narrowest cross section

r space proportion

S thrust

s entropy

T temperature

t time

t_v residence time

ΔU heat of reaction at constant volume

u specific internal energy per unit mass of the gas mixture

V_K
V_K^* combustion chamber volume

v specific volume

w gas velocity

x distance from the injection head

y nozzle coordinate

Z symbol for an exhaust gas component

(Z) molar concentration

z' combustion chamber characteristic number (quality factor)

α heat transfer coefficient

β number of atoms or molecules of a chemical material

$\varepsilon = 2x/d$ dimensionless nozzle coordinate

$\varepsilon' = D^2/d^2$ cross section ratio

$\varkappa$ isentropic exponent /117

$\varkappa'$ ratio of the specific heats at chemical equilibrium

$\bar{\varkappa}$ ratio of the isentropic exponents at frozen equilibrium

$\varkappa^{\Gamma}$ ratio of the isentropic exponents at chemical equilibrium

ρ density

λ oxygen carrier ratio

χ wavelength

ω cyclic frequency

τ ignition delay time

μ viscosity

ν stoichiometric number of moles

ν_i', ν_i'' stoichiometric coefficient of component i in reaction I

$\Delta\nu$ change in the stoichiometric number of moles in a chemical reaction

φ_c^* quality factor

Index designations

1	combustion chamber
2	nozzle end
a	outside state
i	i-th exhaust gas component
j	j-th reaction
f_j	j-th component of the fuel
min, Kr	narrowest cross section
m	number of materials in a gas mixture
r	reaction rate

F. BIBLIOGRAPHY

1. F. A. F. Schmidt — Combustion engines
4th Expanded Edition
Springer Verlag, Berlin 1967

2. F. A. F. Schmidt — Energy conversion in the high-temperature region of high-power engines and rockets. Working Association for Research, No. 151, 1965.

3. O. Stumpf — Theoretical and experimental foundations of high-temperature combustion and the reaction processes in thrust nozzles. Dissertation, Aachen Technical College, 1962

4. H. May — Theoretical and experimental investigations on liquid cooling of gas turbine blades at gas temperatures up to 1200°. Engineering Research, 5, 6, 1962.

5. H. Heitland — Dissociation and recombination processes with state values varying strongly with time. Habilitation paper, Aachen Technical College, 1963.

6. H. Prehn — Investigation of the reaction processes and the autoignition behavior of hydrocarbon-air and oxygen gas mixtures in temperature regions above 1000°K; theoretical and experimental bases preferably using the shock tube method and digital computer technology. Dissertation, Aachen Technical College, 1966.

7. T. F. Zupnik, E. N. Nilson, V. J. Sarli, W. G. Burwell — Investigation of nonequilibrium flow effects in high expansion ratio nozzles. NASA-CR-54042, 1964; NASA-CR-54221, 1964; NASA-CR-52921, 1963.

8. M. D. Horton, M. R. McGie — Particulate damping of oscillatory combustion. AIAA Journal 6/1964

9. P. P. Boynton — Chemical kinetic analysis of rocket exhaust temperature measurements. AIAA Journal 3/1964.

10. M. Barrere — Rocket Engines Elsevier Publishing Company 1961

11. S. S. Penner, I. Dacarme — The Chemistry of Propellants Pergamon Press 1960.

12. R. L. Wilkins — Theoretical Evaluation of Chemical Propellants. Prentice-Hall, Inc., 1963.

13. S. S. Penner — Chemistry Problems in Jet Propulsion /119 Pergamon Press, New York, 1957

14. F. A. Williams — Combustion Theory Addison-Wesley Publishing Co., Reading, USA, 1965.

15. V. N. Huff, S. Gordon, V. E. Morell — General method and thermodynamic Tables for computation of equilibrium composition and temperature of chemical reactions. NACA Report 1037.

16. I. Surugue — Experimental Methods in Combustion Research. Pergamon Press, 1961.

17. M. Barrere — Essais de modeles de foyers pour fusees a propergols liquides Experimental methods in combustion research. AGARD, 1961.

18. C. E. Feiler, L. Baker — A study of fuel-nitric acid reactivity NACA-RM E 56 A 19, 1956

19. R. Edse — Propagation of sound waves in chemically reacting gas mixtures. Proceedings of the Propellant Thermodynamic and Handling Conference, Special Report No. 12, 1960. Also: WADC Report TR 57-485.

20. J. Himpon — The calculation of the volume of rocket combustion chambers. Aircraft Eng. 7/1950.

21. C. H. Trent — Investigation of combustion in rocket thrust chambers. Industrial and Engineering Chemistry 4/1956.

22. C. C. Miesse — On the combustion of a liquid fuel spray. 6th Symposium on Combustion, 1956.

23. I. Sänger-Bredt — Thermodynamic mixture properties of octane fire gases under equilibrium conditions at temperatures up to 4000°K. Verlag Flugtechnik, 1959.

24. M. Rosner, R. Kung, L. S. Dzung — Calculation of the thermodynamic state quantities and the thermodynamic differential quotients of chemically reacting gas mixtgures. Forschung Ingenieurwesen 3/1963.

25. G. P. Sutton — Rocket Propulsion Elements Chapman & Hall, Ltd., 1949

26. L. J. Gordon, J. B. Lee — Metals as fuels in multicomponent propellants. ARS Journal 4/1962.

27. S. S. Penner — Chemistry Reactions in Flow Systems, Butterworth's Scientific Publications, London, 1955.

28. R. Hoglund, D. Carlson, S. Bryon — Experiments on recombination effects in rocket nozzles. AIAA Journal 2/1963. /120

29. P. P. Wegner — Experiments on the departure from chemical equilibrium in a supersonic flow. ARS Journal Vol. 30, 1960.

30. A. Dadieu — Possibilities for increasing rocket power with chemical rocket engines 3rd Lecture Series for Space Technology, Aachen, 1964.

31. E. A. Franciscus, L. C. Lezberg — Effects of exhaust nozzle recombinations on hypersonic ramjet performance. AIAA Journal 9/1963.

32. F. J. Krieger — Chemical kinetics and rocket nozzle design. ARS JOurnal 11/1951.

33. K. N. C. Bray — Chemical reactions in supersonic nozzle flows. 9th Symposium on Combustion, 1963.

34. A. Q. Eschenroeder, D. W. Boyer, J. G. Hall — Nonequilibrium expansions of air with coupled chemical reactions. The Physics of Fluids, 5/1962.

35. K. N. C. Bray — Atomic recombination of hypersonic wind tunnel nozzle. Journal Fluid Mechanics 1/1959.

36. R. Kushida — Nonequilibrium chemical recombination effects in exhaust nozzle flow. Progress in Astronautics and Rocketry Vol. 2, 1960.

37. K. N. C. Bray, J. P. Appleton — Atomic recombination in nozzles. ARC Paper No. 636, 1963.

38. L. Crocco — Aspects of combustion stability in liquid propellant rocket motors. Part I, Journal Am. Rocket Soc. V. 21/1951. Part II, Journal Am. Rocket Soc. V. 22/1952.

39. A. O. Tischler, D. R. Bellman — Combustion instability in an acid-heptane rocket with a pressurized-gas propellant pumping system. NACA-NT 2936.

40. O. Lutz — Report of the meeting on R-drives (records of the German Academy for Research on Air Travel, Berlin, 1943).

41. R. Fuchs — Hypergolic rocket fuels with nitric acid as the oxygen carrier and their measurement with special consideration of organic amines. Zeitschr. Explosivstoffe 5/1958.

42. S. V. Gunn — The effects of several variables upon the ignition lag of hypergolic fuels oxidized by nitric acid. ARS Journal 1 and 2/1952.

43. G. Spengler, A. Lepie — On rocket fuels with hypergolic properties. Zeitschrift für Flugwissenschaften 5/1963. /121

44. G. Spengler, J. Bauer — On hypergolic rocket fuels. Zeitschrift Brennstoffchemie 4/1966

45. M. P. Neumann — Photoelectronics. Frank'sche Verlagsbuchhandlung, Stuttgart

46. F. A. F. Schmidt — Theoretical investigations and experiments on ignition and knock. VDI Research No. 312, 1938.

47. A. Beckers — Investigation of the autoignition behavior of fuels in a compression apparatus, MTZ, Vol. 14, 1953.

48. G. Morrell — Summary of NACA research on ignition lag of self-igniting fuel - nitric acid propellants. NACA-RM E 57 G 19

49.	L. E. Dean R. C. Keith T. L. Summer	Ignition and combustion of aluminum in small-scale liquid rocket engines. Journal Spacecraft, Vol. 2, No. 5, 9/1965.
50.	M. F. Heidmann C. M. Auble	Injection principles from combustion studies in a 200 pound-thrust rocket engine using liquid oxygen and heptane. NACA-RM E 55 C 22 1955.
51.	K. Berman S. E. Logan	Combustion studies with a rocket motor having a full-length observation window. ARS JOurnal 3/4/1952.
52.	D. R. Bellman J. C. Humphrey T. Male	Photographic investigation of combustion in a two-dimensional transparent rocket engine. NACA Report 1134.
53.	E. Sänger	On a rocket engine for long-distance bombers. Verlag Flugtechnik, Stuttgart, 1944.
54.	M. L. Pinns W. T. Olson H. C. Barnett R. Breitwieser	NACA research on slurry fuels. NACA Report 1388, 1958
55.	M. L. Pinns	Effect of surface active additives on physical properties of slurries of vapor-process magnesium. NACA-RM E 55 H 26, 1955.
56.	A. O. Tischler R. V. Massa R. U. Mantler	An investigation of high-frequency combustion oscillations in liquid-propellant rocket engines. NACA-RM E 53 B 27.
57.	H. H. Koelle	Handbook of Astronautical Engineering. McGraw-Hill Book Co., Inc., New York, 1961.
58.	H. Kühl	Dissociation of combustion gases. VDI Forschungsheft, 373, 1935.

59. W. Zangl — The effect of different design values on the characteristics of rocket chambers and injection systems. Raketentechnik und Raumfahrtforschung 3/1958. /122

60. I. A. Watermeier, W. P. Aungst, S. P. Pfaff — An experimental study of the aluminum additive role in unstable combustion of solid rocket propellants. 9th Symposium on Combustion, 1963.

61. A. Moutet — Measurement of temperature in the phenomenon of combustion. Experimental methods in combustion research, AGARD, 1961.

62. M. F. Heidmann, R. J. Priem — A modified sodium-line reversal technique for the measurement of combustion temperatures in rocket engines. ARS Journal 8/1953.

63. Th. Just, H. Pippert — Measurements of relaxation effects in nozzle flows of hot combustion gases by means of a shock tube system. DVL Research Report 66-01, / 1966.

64. D. R. Bartz — A simple equation for rapid estimation of rocket nozle convective heat transfer coefficients. Jet Propulsion 1/1957.

65. C. C. Ferriso — High-temperature spectral absorption of the 4.3 micron CO_2 band. The Journal of Chemical Physics 11/1962.

66. C. C. Ferriso — The emission of hot CO_2 and H_2O in small rocket exit exhaust gases. 8th Symposium on Combustion, 1962.

67. S. S. Penner, P. P. Datner — Combustion problems in liquid fuel rocket engines. 5th Symposium on Combustion, 1954.

68. L. E. Bollinger, M. Goldsmith, A. W. Lemmon. Liquid Rockets and Propellants. Academic Press, New York, 1960.

69. J. G. Hall. Dissociation nonequilibrium in hypersonic nozle flow. American Institute of Chemical Engineers, 7th Symposium, 1959.

70. W. T. Olson. Recombination and condensation process in high area ratio nozzles. ARS Journal 5/1962.

71. H. Ulich, W. Jost. Short Textbook of Physical Chemistry. Steinkopf Verlag, Darmstadt, 1960.

Biography

I was born on [redacted] in [redacted] as the son of the merchant Amandus Schulz and his wife, Paula, nee Berns.

From 1939 to 1953 I attended the primary school and the city high school at Gelsenkirchen-Buer, ending with the matriculation examination.

After working as a probationer in the mechanical industry for half a year, I began the study of mechanical engineering in the Fall of 1953 at the Rhein-Westphalia Technical College, Aachen. I took the principal test for the diploma in December 1958.

From December 1955 to January 1959 I was employed as a scientific aid and, since February, 1959, a scientific coworker and assistant at the Institute for Heat Technology and Combustion Engines of the Technical College, Aachen, under the direction of Prof. Dr.-Ing. Fritz. A. F. Schmidt.